博士論文

Effects of fuel injection angle on combustion efficiency in a model hydrogen ram combustor
（モデル水素ラム燃焼器における燃料噴射角度が燃焼効率に及ぼす効果）

趙　徹

Abstract

Effects of fuel injection angle on the combustion efficiency in a model hydrogen ram combustor, which is based on a pre-cooled turbojet engine afterburner developed by Japan Aerospace Exploration Agency, were investigated both experimentally and numerically in this study.

Various combinations of fuel injection angles with two types of injection hole arrangement have been tested experimentally, the results indicated the correlations between the combustion efficiency and the injection angle at different injection hole arrangement. The combustion efficiency increased with an increase in the upstream injection angle at a serial injector arrangement. It showed an approximately 10%~15% improvement over the serial case at a zigzag arrangement case, When the upstream injection angle changed, a difference in combustion efficiency was observed.

Numerical simulation was considered necessary to understand the results revealed by the experiments. Therefore, a numerical solver for non-premixed turbulent combustion based on large eddy simulation (LES) using Flamelet Progress Variable (FPV) method was applied with OpenFOAM and validated using experimental results of Sandia Flame D. Numerical simulation of the combustion field inside the model ramjet combustor with eighteen combinations of injection angle of two arrangements with FPV model were performed. The trend of simulation results showed a good agreement with the experiments, and the zigzag arrangement injector with 30° upstream and 60° downstream injection angle achieved the best combustion efficiency. The difference between the best case of two different arrangements was close to 7%. Besides, the numerical results also revealed the working status of two kinds of injectors and explained why different arrangements and injection angles affect combustion efficiency. For both kinds of arrangement, the upstream injection angle played the most crucial role in combustion efficiency, but the trend was converse. The downstream injection angle for both two arrangements mainly affected the recirculation zone. However, for two kinds of arrangement injectors, the way of achieving high combustion efficiency was different. The serial arrangement injector increased the combustion efficiency by increasing the penetration height. The zigzag achieving the high combustion efficiency mainly depended on the recirculation zone in the wake of the injector.

Contents

Figure List

Table List

1 Introduction

1.1 Research background

Japan Aerospace Exploration Agency (JAXA) has been developing a cryogenic hydrogen-fueled pre-cooled turbojet engine (PCTJ): a combined cycle engine of the gas turbine and the ramjet engine (afterburner) for hypersonic transports [1], as shown in Figure 1. The system diagram is shown in Figure 2. Since hypersonic propulsion for Mach 5 flight systems cannot be realized with a conventional jet engine, the total temperature of incoming air reaches approximately 1300K, leading to the failure of the engine cycle. The PCTJ engine is equipped with a pre-cooler to cool incoming air by heat exchange with liquid hydrogen at upstream of a core engine. Also, it has an afterburner to create sufficient thrust for hypersonic flight. The afterburner is equipped with strut injectors to provide after-burning and is fitted with a single-ramp rectangular variable exhaust nozzle, as shown in Figure 3. At the afterburner, fuel is hydrogen which is reused from the pre-cooler, and the condition is considered hydrogen-rich combustion since pre-cooling needs a large amount of hydrogen. By combining such a pre-cooler and an afterburner, PCTJ can operate up to Mach 6. Although conventional jet engines fueled by jet fuel operate under lean conditions, the PCTJ engine is designed to operate with an equivalence ratio of 2.2 in the afterburner at the cruising condition of Mach number 5. It is possible to maximize the payload under the fuel-rich condition because the mean molecular weight of the hydrogen-rich combustion gas is smaller than the combustion gas molecular weight of jet fuel, resulting in the higher exhaust speed at the nozzle exit [1]. In order to achieve a high thrust under these given conditions, the afterburner needs maintain the combustion temperature as high as possible. Thus, the importance of combustion efficiency is highlighted. In order to achieve efficient combustion, in past decades, a number of studies have been conducted. These results indicate that combustion efficiency is highly affected by the mixing process of reactants, ignition process, and flame holding structure in a highly turbulent and enthalpy flow field [2].

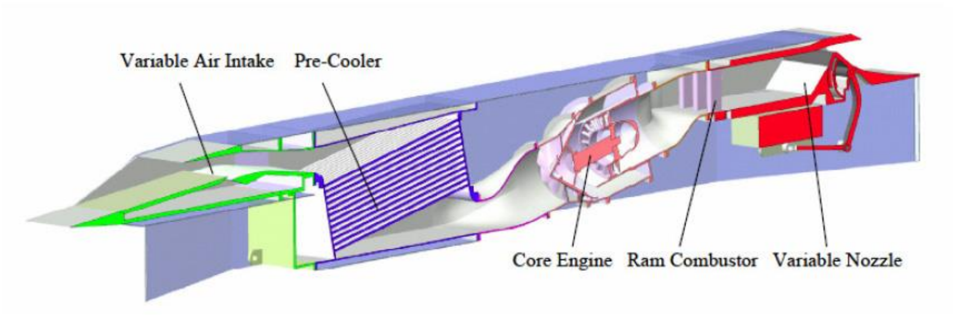

Figure 1 Pre-Cooled Turbo Jet Engine [3]

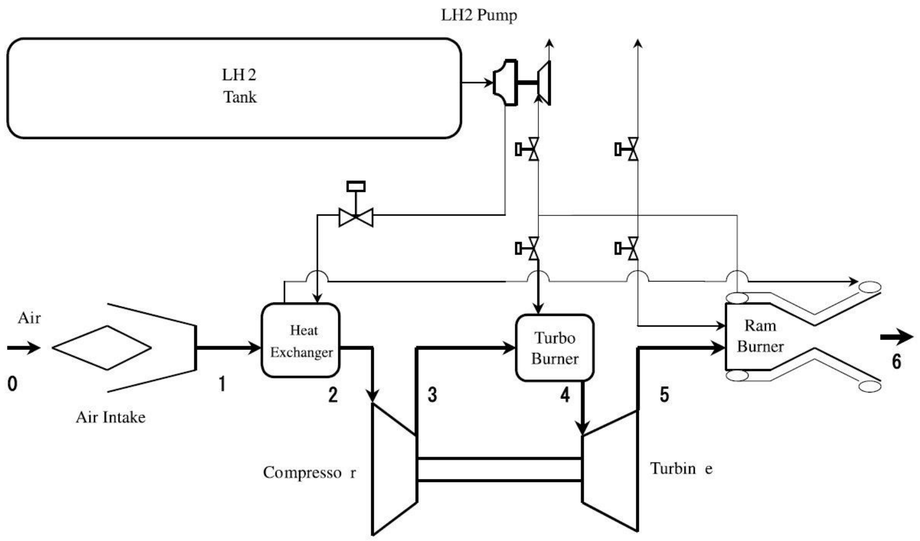

Figure 2 PCTJ system diagram [4]

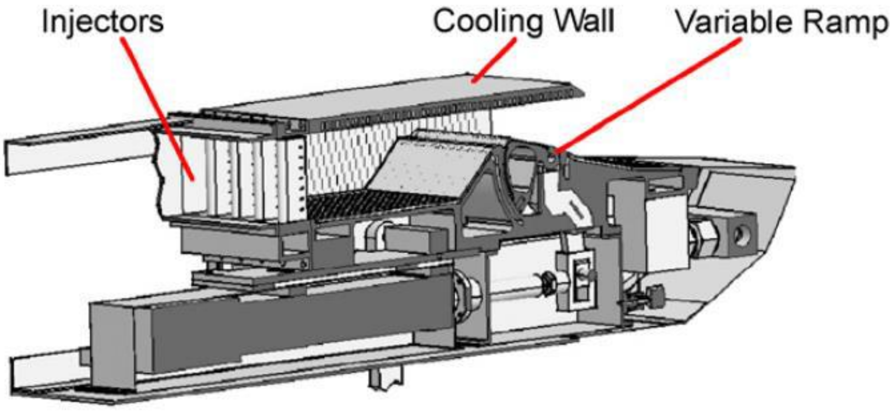

Figure 3 Afterburner of the PCTJ [5]

1.2 Previous research

During the mixing process, the vortices play a significant role. In the former studies of ramjets and scramjets, it has been shown that the mixing process in the streamwise direction is enhanced by increasing vortices to form pressure and density gradients. The study of vortices formation has been widely done in previous research articles [6-8]. In order to form vortices, a typical method is the utilization of different types of injectors in the flow field, such as swirl injectors [9], strut injectors [10], and wall injectors [11]. Swirl injector is a wildly used type of injector. It is preferred by liquid rockets with staged combustion, gas turbines, and diesel engines for its high mixing and atomization efficiency. Strut and wall injectors are mainly used in gas turbine afterburners, ram combustors with subsonic or supersonic airflow. Wall injectors can enhance the mixing process and bring flow blockage to the flow field; meanwhile, it could cause thrust losses. The strut injectors affect the cross-section area in the chamber, however they can provide a flame holding position in the wake of the injector. A stable flame holding area is essential for achieving stable and efficient combustion in a high-speed flow field. If the fuel is injected parallel to the main flow direction with a strut injector, it can also provide additional thrust by adding redundant momentum. A significant different point of the strut injector compared with the swirl injector and the wall injector is that the strut injector has limited mixing enhancement capabilities, especially when the parallel injection is used. However, the vortices on the streamwise generated by the strut injector makes up for this problem [11]. Thus, if the strut injector is applied in the combustor, the mixing process needs to be enhanced by additional measures, and the vortices in the wake of the injector are also supposed to be noted.

In the PCTJ afterburner, the strut injector is equipped to increase vorticity in the streamwise direction. The fuel is injected from the up and down surface of the strut injector as different injector angles to enhance the mixing process. The vortices zone in the wake behind the injector trailing edge further enhances the mixing process and provides a flame holding area. Extensive research has been carried out in the field of the bluff body acted as a flame holder under different flow conditions [13-16]. The vortices in the wake of the bluff body play a significant role in stabilizing the whole combustion field. The same as the bluff body research, Former studies have shown that utilization of wall injection or called transverse injection as a fuel injection type to enhance the mixing process for ramjet or scramjet has been under consideration for a long time [17-19]. The wall injection/transverse injection effectively enhances the mixing process. Then a combination of the bluff body and transverse injection was considered a promising way to achieve a high efficient strut injector for PCTJ. For the PCTJ's strut injector, there are two rows of injector holes along the streamwise direction. Furthermore, a reasonable arrangement of the injector holes was considered since there may be an interaction between two rows of injection holes. Almost all of the research has focused on a fuel-lean condition for propulsion system. In former research [20], it has indicated that the temperature ratio of burned and unburned gas has apparent influences on the bluff body wake structure. The high equivalence ratio in the PCTJ combustor makes the flame temperature ratio different from the normal lean condition. Therefore, to obtain efficient and reliable combustion, a reconsideration of the design of the PCTJ injector under fuel-rich condition is necessary.

1.3 Objective

The objective of this study is to investigate effects of fuel injection angle on combustion efficiency in a model hydrogen ram combustor experimentally and numerically. A combustion measurement technique for a hydrogen ram model combustor using a high-enthalpy wind tunnel and a calculation method for non-premixed turbulent combustion based on LES using the Flamelet Progress Variable (FPV) method have been applied. In order to obtain knowledge of the optimum injection angle of the injector with two rows of orifices, hydrogen-rich combustion experiments were performed. Numerical calculations were performed for a standard burner, the Sandia Flame D, to verify the validity of the calculation method and model. After that, numerical calculations have been performed to reproduce the experimental system. Thereafter, the injection angle and the injection orifices configuration that maximize the combustion efficiency have been investigated numerically. By showing physical quantities that were difficult to measure experimentally through numerical calculations, the mechanism by which resulted in high combustion efficiency was investigated.

1.4 Methodology

In the experiment part, to simulate the flow in the afterburner of PCTJ under cruising conditions, a high-enthalpy wind tunnel in Kashiwa campus, the University of Tokyo, was used to simulate an operating condition of PCTJ. The combustor was installed at the wind tunnel directly. The inlet temperature was heated up to approximately 900K, and 0.3MPa. Air composition was considered as 23.1% O_2 and 76.9% N_2 in mass percentage. The hydrogen mass flow rate was set corresponding to the equivalence ratio of 2.2 with the temperature of 300 K. B-type thermocouples were installed at the combustor entrance and exit to measure inlet air and exhaust gas temperature. The combustion efficiency was calculated based on these temperature records. The airflow rate was measured by an airflow meter. Combustion pressure was measured with a pressure transducer connected to the combustion chamber. A high-speed camera recorded Near-infrared (NIR) emissions from water molecules to identify the high-temperature region in the combustion field during the experiment. Two kinds of arrangement of injection arrangements were evaluated: serial and zigzag. Two kinds of injection holes' arrangement injectors (serial and zigzag) were tested in the experiment. There were eight upstream and downstream injection angles combinations for serial arrangement injectors, one for zigzag arrangement injectors. However, the investigation was not performed only by experiment since the experiment data in the combustion field with high turbulent, high enthalpy, and nanoseconds chemical reactions are hard to measure. Thus, numerical simulation is one of the promising methods that are helpful to understand the function of the different injectors.

The numerical research on hydrogen-rich combustion in high enthalpy and high turbulence conditions is rather limited since most propulsion systems work under lean conditions. Even if there is some research on hydrogen-rich combustion in turbulent conditions, these researches are mainly in the premixed condition [21-23]. Therefore, fundamental research is needed in the present study. First, a proper turbulent model and chemical reaction model is necessary for the investigation. Large-eddy simulation(LES) is the best choice for the turbulent model since the research focus on the vortices' effect. Although directed numerical simulation can provide perfect results for the turbulent, it costs too many computation resources. On the other hand, the RANS model cannot be used because it erases the vortices' detailed information. For a chemical reaction, the chemical model needs to account for finite-rate chemistry effects and reflecting local extinction, re-ignition phenomena for the turbulence/chemistry interaction. After these requirements, the chemical reaction model still needs to be coupled with LES and less cost of computation resource. With all these requirements, the flamelet/progress variable approach is one of the ideal choices.

The flamelet model simulates the combustion process with detailed chemistry by consuming fewer computation resources [24]. Flamelet/progress variable (FPV) model for LES was developed base on the flamelet model. This model uses a steady-state flamelet solution, but it is different from the typical steady or stretched laminar flamelet model (SLFM) [25]. The SLFM concept assumes that turbulent combustion flame can be divided into small laminar diffusion flames at any time, generally referred to as flamelets. The assumption is justified when the chemical reaction zone is thinner than the turbulent length scales, or in other words, the Damkohler number is large enough. Within this limit, the SLFM is a reliable and widely-used approach that accounts for finite-rate chemistry effects at a reasonable computational effort. The main advantage of SLFM is accomplished by separating the flow field and the chemical reaction calculation and link them by a few parameters. In practice, the chemical reaction is calculated in a pre-processing step and stored in a "flamelet library." The problem of SLFM is that it is not suitable for non-premixed combustion since the local extinction and re-ignition phenomena cannot be predicted [26-30]. In SLFM, the steady flamelet solution is parameterized by scalar dissipation rate. For a scalar dissipation rate value less than the extinction critical value, the steady-flamelet model cannot distinguish flame state between steady burning state and unstable burning state. In the FPV approach, a new parameter called reaction progress variable is employed to replace the scalar dissipation rate to parameterize the flamelet solution monotonically. It can provide a complete flamelet solution that includes descriptions of local extinction and re-ignition which are represented by unstable burning state.

Transport equation is required by filtered reaction progress variable from the aerodynamics in LES. The transport equation is solved in the calculation process. At last joint probability density function PDF [30] of mixture fraction and reaction progress variable is used to close the flamelet/progress variable model and beta function shows good performance.

In the present work, simulations with LES couped with flamelet/progress variable model have been carried out by OpenFOAM-2.3.x [31]. A 3-D turbulent diffusion flame Sandia Flame D [32] was considered for the FPV model validation. The accuracy of the non-premixed hydrogen/air flamelet library was evaluated through a priori analyses of the 2-D counterflow flames case. Eighteen non-premixed hydrogen-rich combustion cases with two kinds of injection hole arrangement (serial and zigzag) were analyzed by numerical simulation with FPV model.

1.5 Thesis outline

In this chapter, the background of this research and the specific objectives have been discussed. The outline of the thesis are as follows:

Chapter 2: The experimental results from the two kinds of arrangement injectors in the model hydrogen ram combustor have been described, and the question from the experiment results are issued.

Chapter 3: The governing equations for turbulent combusting flows have been presented. A numerical simulation with FPV model was applied to non-premixed combustion, and it was validated by the Sandia Flame D.

Chapter 4: A hydrogen flamelet library has been generated and validated for the experimental results shown in Chapter 2 using a model ramjet combustor. The inlet condition of velocity distribution is also determined.

Chapter 5: The numerical results around the injection holes and recirculation zone has been discussed to reveal the correlation between the combustion efficiency and different injector arrangement and injection angles.

Chapter 6: Concluding remarks obtained in the present study are shown.

2 Experimental investigation of the combustion efficiency using model afterburner

In order to simulate a condition in the afterburner of PCTJ at cruising, a high-enthalpy wind tunnel in Kashiwa campus, the University of Tokyo, was used, as shown in Figure 4. This wind tunnel owns a hypersonic flow line, a high enthalpy flow line, and a pebble type heater, which can be switched between the two lines. For this study, a high enthalpy flow line was used. The wind tunnel has compressed air storage and a heater. The heater is filled with alumina pebbles, and a city gas burner heats them. As the air goes through the pebbles, the air temperature becomes high through heat exchange with the pebbles. The physical values of airflow at the test section entrance were set as the simulated condition at the entrance of the afterburner on the actual engine under flight condition with Mach5. The inlet temperature was heated up to approximately 900K, and pressure from the high-enthalpy wind tunnel was 0.3MPa. The combustor was installed at the end of the wind tunnel directly. In the experiment, after 40-second preheating, gas hydrogen was injected into hot airflow from the injectors and made auto-ignition. A combustion test was performed for 4-seconds.

The relative experiment research has been initiated by Taguchi et al. [33] and then followed by Nishida et al. [34] [35]. From 2008 through 2012, flame ignition, temperature, and flame shape have been identified in their research. In the present research, combustion efficiency was focused. In order to get data for validations of numerical study, dynamics of high-temperature combustion gas were observed with a high-speed video camera. Near-infrared emissions from water molecules were used as a marker of the high-temperature region.

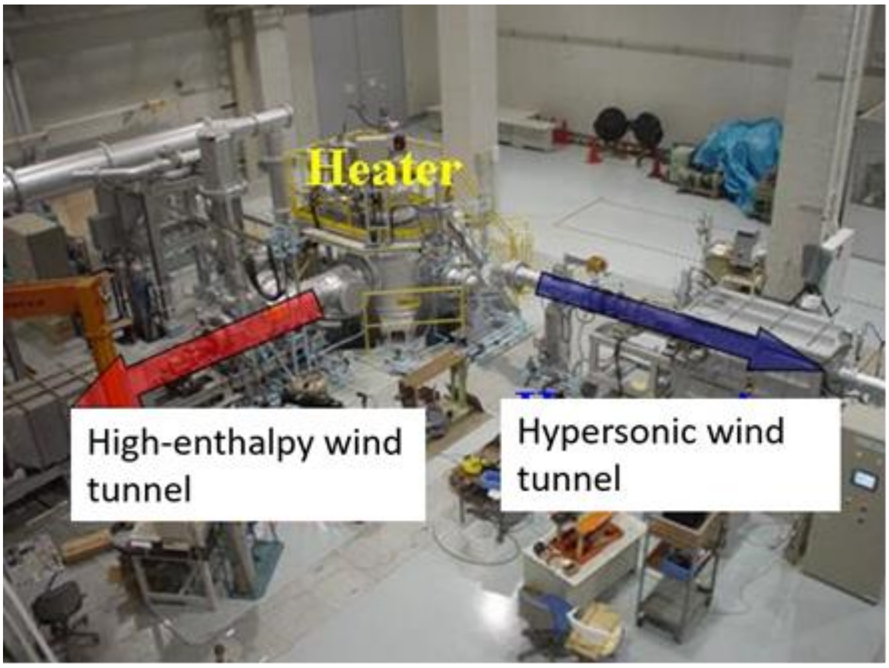

Figure 4 Hypersonic and High Enthalpy Wind Tunnel

2.1 Apparatus

A subscale PCTJ's afterburner has 75mm×200mm rectangular cross-section and has six injectors. In this research, a small testing combustor with 48mm × 32mm rectangular inside cross-section equipped one injector has been made to consider safety and limitation of airflow rate. A schematic diagram of the experiment equipment is shown in Figure 5. The model combustor for the test was installed at the exit of the heater directly. Hot air was provided from the heater, which simulated exhaust gas from the core engine of PCTJ. Gas hydrogen was injected as fuel into the combustor.

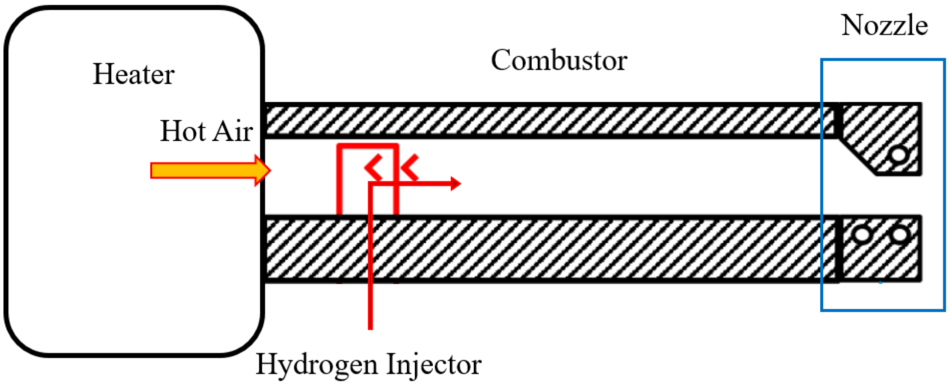

Figure 5 Schematic Drawing of the Test Equipment

In the present study, no igniter was used because high-temperature air enabled auto ignitions. A nozzle with 7mm×48mm rectangular throat was installed downstream of the combustor to set combustion pressure to 0.3MPa as a design point pressure. The combustor was made of stainless steel and equipped with water-cooling. 32mmx316mm windows were installed on the top surface and both sides of the combustor for optical measurement. In this experiment, combustion was observed through the top surface window through silica glass. Both side's surfaces windows were covered by hatches made of carbon/carbon composite. The nozzle was also made of stainless steel, and heat-resistant cement was laid on the inside surface. The detail dimension parameters are as follows. The test chamber's total length is 390mm, the 68mm x 52mm cross-section area with 10 mm thickness walls. The side surface windows are 23mm × 310mm.

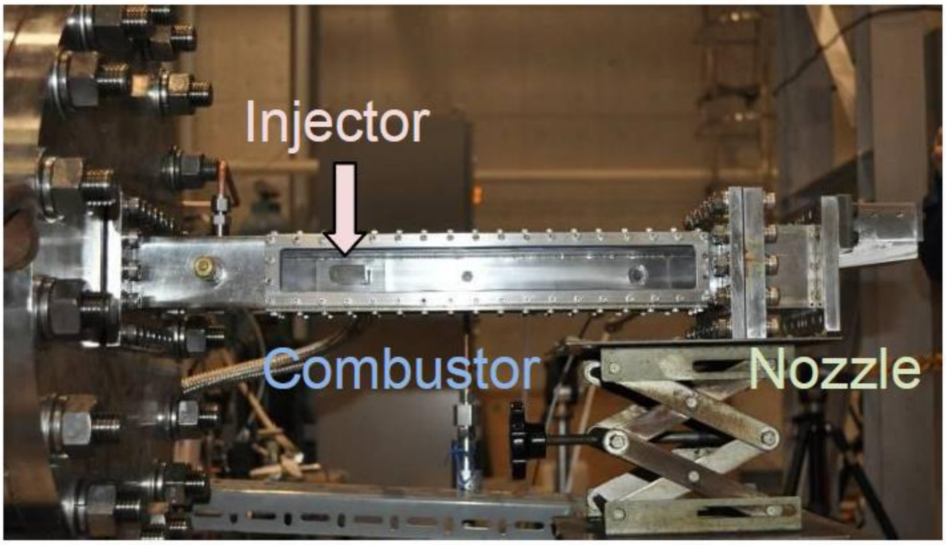

Figure 6 Experimental model afterburner combustor [34]

The injector has a round shape on leading-edge, and a rectangular shape at the trailing edge. This design is based on the result of the past experiment by JAXA. Injection holes were arranged in two rows along the streamwise direction, as shown in Figure 7. The injection holes' diameter was fixed at 1mm to keep the injection speed is sonic speed since the investigation focus on the injection holes' arrangement and angle. Figure 8 shows a definition of the injection angle. The detail dimension parameters are as follows. The injector's total length is 27.25mm. The height is 9.5mm, which is also the diameter of the round shape leading edge. The total depth is 56.5mm. Two kinds of injection holes’ arrangement injectors, serial and zigzag, as shown in Figure 9, have been tested in the experiment. Upstream and downstream orifices deploy at 11mm and 1.2mm from the trailing edge, respectively. Six upstream orifices are arranged equidistantly along chamber width. Downstream orifices are arranged along with the upstream orifices or mid perpendicular of upstream orifices. The injector trailing edge is at the position of 300mm upstream from the outlet of the combustor and in the middle of the combustor height. In the experiment, the serial arrangement injector has been used. The zigzag arrangement injector with a 30° upstream injection hole and a 60° downstream injection hole has also been tested.

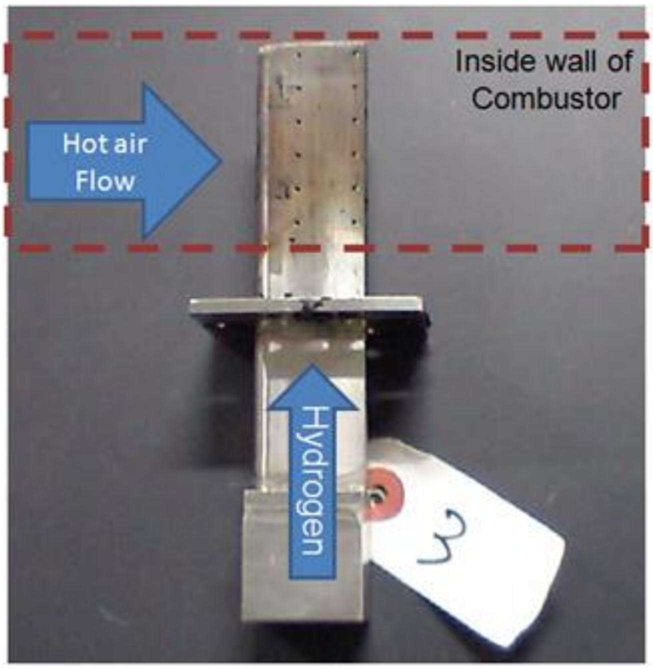

Figure 7 Injector

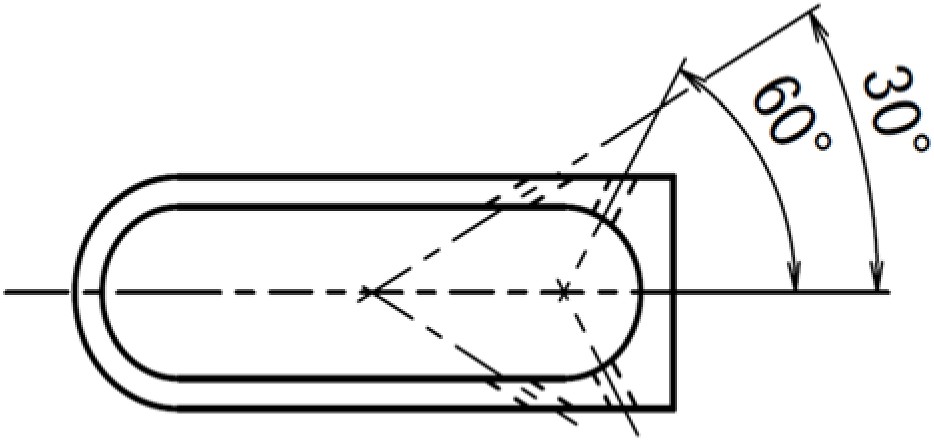

Figure 8 Definition of the injection angle

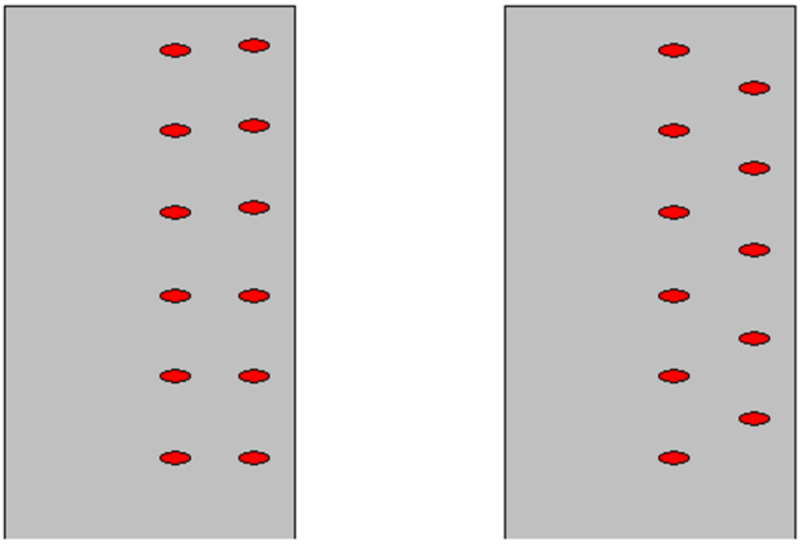

Figure 9 Serial(left) and Zigzag(right) arrangement injector

The incoming airflow conditions simulated conditions of the afterburner under a Mach 5 cruising condition of PCTJ. The pressure from the high-enthalpy wind tunnel was 0.3 MPa. The inlet temperature was heated up to approximately 900K. Air composition was considered as 23.1% O_2 and 76.9% N_2 in mass percentage. The hydrogen mass flow rate was set corresponding to the equivalence ratio of 2.2 with the temperature of 300 K. It was controlled by a needle valve (Swagelok, SS-5PDF8), which was validated by a flow meter (KOFLOC, RK1950AP) that has an accuracy of 2%. Hydrogen mass flow rate was calculated by the flow characteristic of the control valve and pressure of hydrogen upstream and downstream of a control valve. The flow characteristic of the control valve has been examined before the combustion test by using nitrogen gas. The injection pressure was measured by a pressure sensor (TEAC, TP-AR 1 MPa) with an accuracy of 1%. All test sequences and synchronization were made by USB6229, which National Instrument made, and the LabVIEW program coded the program.

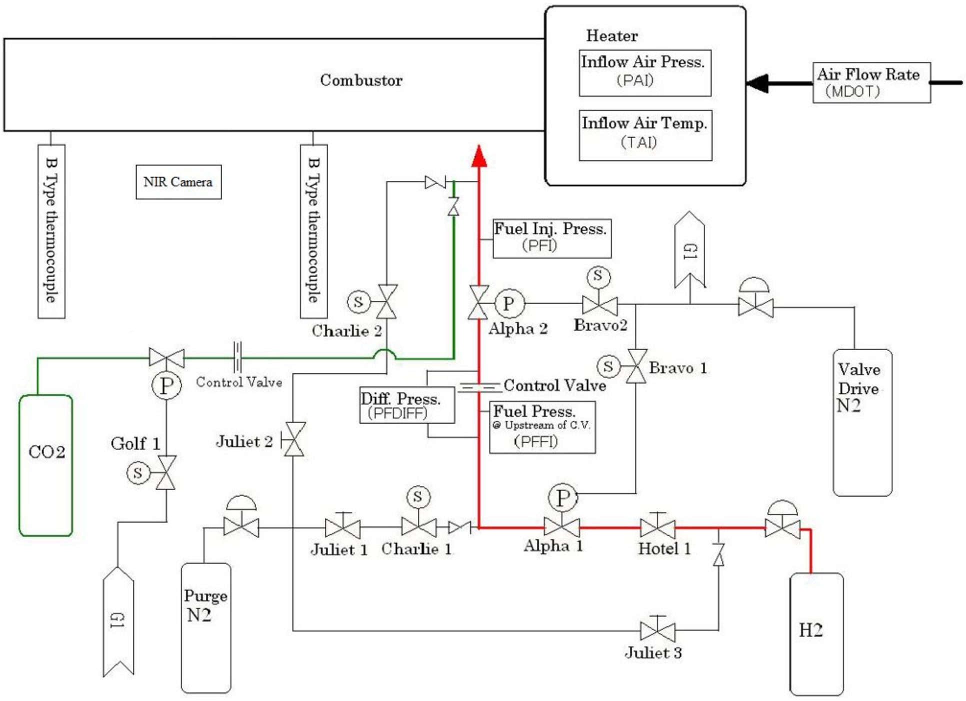

Figure 10 Setup of Experiment

Figure 10 is a schematic drawing of the setup. All controls and measurements were teleoperated from a control room. This is because all experimental rooms have to evacuate from the vicinity of the wind tunnel to the control room for safety. Hydrogen was supplied or cut off by pneumatic valves. After combustion, hydrogen remaining in the pipe was purged by nitrogen gas.

B-type thermocouples were installed at the combustor entrance and exit to measure inlet air and exhaust gas temperature, as shown in Figure 11. The airflow rate was measured by an airflow meter. Combustion pressure was also measured by a pressure transducer connected to the combustion chamber. Signals from these sensors were recorded on a local computer which was set around the wind tunnel via amplifiers and A/D converters. In order to protect the thermocouple, additional CO_2 was injected into the combustor to reduce the flame temperature. The mass flow rate was 2.439g/s.

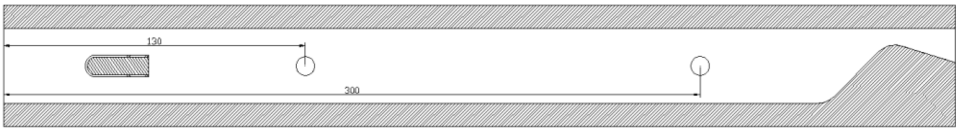

Figure 11 B-type thermo couples installation position [35]

Ethernet was used for connection between the local computer and a remote computer in the control room. Measurement and control were done by a remote computer in the control room. The automatic valve control program was made by LabView either. This program outputs digital operation signals and drives relay contacted to operate valves. The valves were also operated manually on a manual control panel in the control room to make irregular control without the program.

2.2 Near-Infrared emission

Experiments were conducted within the PCTJ operation range, the NIR emissions from water molecules were captured. From the combustor up surface window, NIR emission from water molecules was captured using a high-speed camera (Vision Research Phantom Miro LC 310) equipped with a NIR filter (Fujifilm, IR-78), and the sampling rate was 20,000 fps.

In hydrogen combustion, it is considered that the emission in the NIR range is caused by water molecules [36]. The water emission becomes stronger as the temperature becomes higher, which can indicate that the region with vigorous NIR intensity has a high temperature [36].

2.3 Calibrated flame temperature from thermocouple measurement value

In order to obtain the calibrated flame temperature from the measurement temperature of thermocouple, the estimation of flame viscosity and thermal conductivity is necessary. The detail is as follow.

The viscosity coefficient μ_i of a single component is expressed by the following equation.

$$\mu_i = 8.4401 \times 10^{-5} \frac{\sqrt{M_i T}}{\gamma^2 \Omega^{(2.2)*}} \tag{1}$$

γ is the collision diameter of the molecule. $\Omega^{(2,2)*}$ is the collision integral which is expressed as follow.

$$\Omega^{(2.2)*} = 1.16145 T^{*-0.14874} + 0.52487 \exp(-0.7732 T^*) + 2.16178 \exp(-2.43787 T^*) \tag{2}$$

T^* is a dimensionless temperature, which is the temperature divided by the effective temperature of the molecule ε/k.

$$T^* = \frac{T}{\varepsilon / k} \tag{3}$$

where ε is emissivity, and k is thermal conductivity.

The collision diameter and effective temperature of each molecule was listed in Table 1.

Table 1 Collision diameter and effective temperature

Species	Collision Diameter	Effective Temperature [K]
N2	3.621	97.53
O2	3.458	107.4
H2	2.92	38
H2O	2.605	572.4
Ar	3.33	136.5
CO2	3.763	244

The viscosity of mixture was calculated by Sutherland's empirical formula.

$$\mu = \sum_i \frac{X_i \mu_i}{\sum_j X_j \Phi_{ij}} \tag{4}$$

X is the mole fraction. Φ_{ij} was provided by Wilke et al. empirical formula.

$$\Phi_{ij} = \frac{1}{2\sqrt{2}} \left(1 + \frac{M_i}{M_j}\right)^{-1/2} [1 + \left(\frac{\mu_i}{\mu_j}\right)^{1/2} \left(\frac{M_j}{M_i}\right)^{1/4}]^2 \tag{5}$$

Where *M* is molecular weight.

The thermal conductivity ki of a single component can be calculated from the following equation which was provided by Eucken

$$k_i = 0.25\left(9c_{p,i} - 5c_{v,i}\right)\mu_i \tag{6}$$

cp is calculated from the NASA CEA program, the equation is as follow.

$$\frac{c_p}{R} = \frac{a_1}{T^2} + \frac{a_2}{T} + a_3 + a_4 T + a_5 T^2 + a_6 T^3 + a_7 T^4 \tag{7}$$

cv was calculated by subtracting molar gas constant R from cp. The constants are listed in Table 2.

Table 2 Coefficient of Specific heat capacity polynomial

	N2	O2	H2	H2O
a1	5.88E+05	-1.04E+06	5.61E+05	1.03E+06
a2	-2.24E+03	2.34E+03	-8.37E+02	-2.41E+03
a3	6.07	1.82	2.98	4.65
a4	-6.14E-04	1.27E-03	1.25E-03	2.29E-03
a5	1.49E-07	-2.19E-07	-3.74E-07	-6.84E-07
a6	-1.92E-11	2.05E-11	5.94E-11	9.43E-11
a7	1.06E-15	-8.19E-16	-3.61E-15	-4.82E-15

	Ar	CO2
a1	2.01E+01	1.18E+05
a2	-5.99E-02	-1.79E+03
a3	2.50	8.29
a4	-3.99E-08	-9.22E-05
a5	1.21E-11	4.86E-09
a6	-1.82E-15	-1.89E 12
a7	1.08E-19	6.33E-16

The thermal conductivity of mixture has the same form with viscosity.

$$k = \sum_i \frac{X_i k_i}{\sum_j X_j \Phi_{ij}} \tag{8}$$

$$\Phi_{ij} = \frac{1}{2\sqrt{2}} \left(1 + \frac{M_i}{M_j}\right)^{-1/2} [1 + \left(\frac{k_i}{k_j}\right)^{1/2} \left(\frac{M_j}{M_i}\right)^{1/4}]^2 \tag{9}$$

In the calculation, the O2 was considered as fully consumed since the combustion under hydrogen rich condition.

The measurement temperature T_c of the thermocouple is lower than the actual temperature T. T_c is the result of equilibrium of heat convection with flame and heat conduction and radiation to the outside. Thus, the relation between actual temperature and measurement temperature can be written as:

$$h_m (T - T_c)\pi dl = \varepsilon\sigma(T_c^4 - T_\infty^4)\pi dl + 2k_c \frac{\pi d^2 (T_c - T_\infty)}{4L} \tag{10}$$

h_m is the average heat transfer coefficient from the flame around the thermocouple contact point, ε is the emissivity of the thermocouple contact point, σ is the Stefan-Boltzmann constant, T is actual flame temperature, k_c

is the thermal conductivity of the wire of the thermocouple. In addition, *d* and *l* are the diameter and length when the contact point is regarded as a cylinder, and *L* is the distance to the point of the actual temperature.

The empirical formula of the average heat transfer coefficient is displayed in the form of the Nusselt number.

$$Nu_m = \frac{h_m d}{k} = f(\mathrm{Re}, \mathrm{Pr}) \tag{11}$$

where

$$\mathrm{Re} = \frac{\rho d V}{\mu} \tag{12}$$

and

$$\mathrm{Pr} = \frac{c_p \mu}{k} \tag{13}$$

k is the thermal conductivity of the flame gas; *d* is the characteristic length. The Nusselt number is generally a function of the Reynolds number and the Prandtl number for forced convection.

The Nusselt number was calculated by the approximation formula proposed by Morgan et al. [37].

$$Nu_m = a \times \mathrm{Re}^n \tag{14}$$

The coefficients *a* and *n* are given as shown in Table 3 base on the Reynolds number range.

Table 3 Coefficients in Nusselt approximation

Re			
From	To	a	n
$<4x10^{-3}$	$4x10^{-3}$	0.437	0.0895
$4x10^{-3}$	$9x10^{-2}$	0.565	0.136
$9x10^{-2}$	1	0.800	0.280
1	35	0.795	0.384
35	$5x10^{3}$	0.583	0.471
$5x10^{3}$	$5x10^{4}$	0.148	0.633
$5x10^{4}$	$>5x10^{4}$	0.0208	0.814

Thus, T is a function of T_c and the flow velocity V.

$$T = f(T_c, V) \tag{15}$$

Therefore, T and V can be obtained by T_c from two different thermocouples. R-type and B-type thermocouples were used for the calibration. The diameter of B-type and R-type thermocouple contact point is 72 μm and 773 μm, respectively. The contact point length is 3.79 mm, and 0.92 mm. B-type and R-type thermocouple average emissivity is 0.3 and 0.27, respectively. The length of B-type and R-type wire is about 300 mm and 30 mm.

Part of experimental results of flame temperature was listed in Table 4.

Table 4 Calibrated flame temperature

Equivalence ratio	Case	Temperature [K]
2.19	120&60	1860
2.22	60&60	1765
2.25	120&60	1850
2.25	60&45	1805
2.31	60&45	1810
2.35	30&60	1830
2.42	45&45	1730
2.45	45&60	1650
2.46	45&60	1670
2.51	45&60	1620
2.52	30&60	1760
2.64	30&60	1630

3.28	45&60	1600

2.4 Combustion efficiency

The combustion efficiency was evaluated by the definition provided by Nishida [34]. Inlet air and exhaust gas temperature, the airflow rate, and the hydrogen flow rate were used for calculating combustion efficiency. The chemical reaction was recognized as an equilibrium reaction to calculate the efficiency since the reverse reaction was vanishingly tiny in our condition. During the calculation process, the reverse reaction's effect did not count into the balance of enthalpy. Thus, the reverse reaction was ignored.

The equations used for calculating the combustion efficiency *e* are shown as follows. The expression of degree 3 approximates the enthalpy of each gas.

$$e = \frac{Q_{ac}}{Q_{th}} \tag{16}$$

$$Q_{th} = \dot{m}_{burn} q \tag{17}$$

$$\dot{m}_{burn} = \frac{0.231}{8} \dot{m}_{air} \tag{18}$$

$$Q_{ac} = Q_{in} - Q_{ex} \tag{19}$$

$$Q_{in} = \dot{m}_{air} H_{air}(T_{in}) + \dot{m}_{H_2} H_{H_2}(T_{H_2}) \tag{20}$$

$$Q_{ex} = \dot{m}_{N_2} H_{N_2}(T_{ex}) + \dot{m}_{H_2O} H_{H_2O}(T_{ex}) + \dot{m}_{O_2ex} H_{O_2}(T_{ex}) + \dot{m}_{H_2ex} H_{H_2}(T_{ex}) \tag{21}$$

$$\dot{m}_{N_2} = 0.769 \times \dot{m}_{air} \tag{22}$$

$$\dot{m}_{H_2O} = \frac{18}{32} \times 0.231 \times \dot{m}_{air} \tag{23}$$

$$\dot{m}_{O_2ex} = 0 \tag{24}$$

$$\dot{m}_{H_2ex} = \dot{m}_{H_2} - \frac{0.231}{8}\dot{m}_{air} \tag{25}$$

$$H_{air} = 1.798 \times 10^{-8} T^3 + 4.800 \times 10^{-5} T^2 + 9.832 \times 10^{-1} T - 3.113 \tag{26}$$

$$H_{N_2} = 9.161 \times 10^{-10} T^3 + 7.917 \times 10^{-5} T^2 + 9.958 \times 10^{-1} T - 7.211 \times 10^{-1} \tag{27}$$

$$H_{H_2} = 2.682 \times 10^{-7} T^3 + 9.279 \times 10^{-5} T^2 + 1.440 \times 10 T + 3.645 \tag{28}$$

$$H_{O_2} = -2.000 \times 10^{-8} T^3 + 0.200 \times 10^{-3} T^2 + 8.476 \times 10^{-1} T + 3.531 \tag{29}$$

$$H_{H_2O} = 2.000 \times 10^{-9} T^3 + 0.300 \times 10^{-3} T^2 + 1.688 T + 1.245 \times 10 \tag{30}$$

Here, Q_{ac} is the enthalpy difference between the combustor exit and combustor entrance. Q_{th} is the theoretical heat release. The m dot denotes the mass flow rate. The subscript notation has been used for species name and location. The position of inlet and outlet of the combustor is indicated by *in* and *ex,* respectively. T is the temperature measured by a B-type thermocouple installed at the combustor exit. H is the enthalpy. The energy density of hydrogen, q, is 119594 kJ/kg. The consumed hydrogen mass flow rate was calculated by m_{burn} dot since it was fuel-rich combustion.

2.5 Results and discussion

2.5.1 Effect of injection angle on combustion efficiency

Effect of upstream injection angle on combustion efficiency

Figure 12 represents the correlation between combustion efficiency and upstream injection angle. The equivalence ratio was 2.2, and the pressure of the combustion field was 0.3MPa. The target condition was an actual one of the PCTJ engine at Mach 5 flight condition. As shown in the figure, it was clear that the combustion efficiency increased as the upstream injection angle increased.

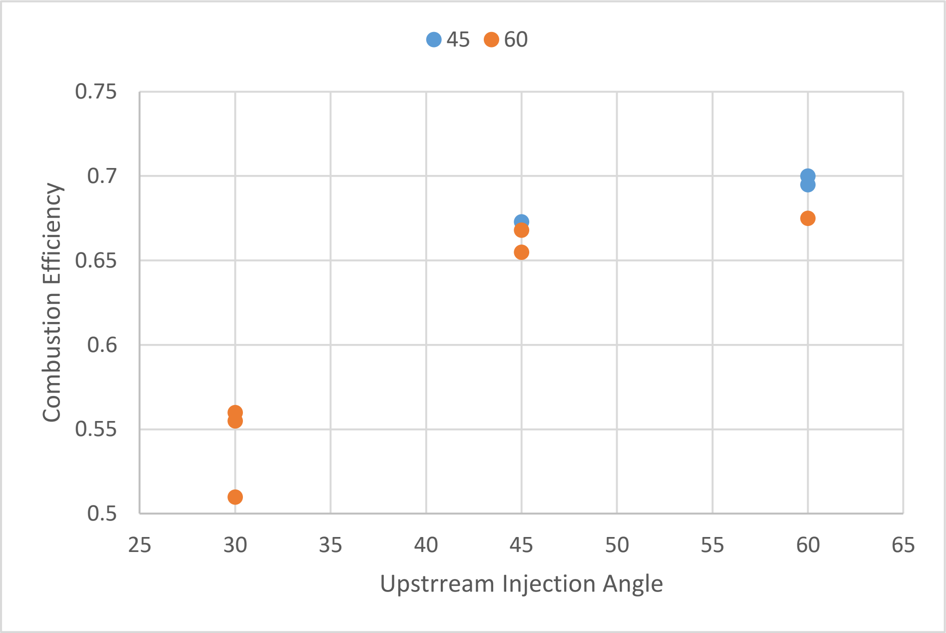

Figure 12 Correlation between combustion efficiency and upstream injection angle (Downstream injection angle marked as legend)

The equivalence ratio of these cases was 2.2. It could be regarded as half of the hydrogen mass flow rate was injected from upstream injection holes since the configuration of injection holes are all the same between upstream and downstream except injection angle. This indicated that the equivalence ratio of the hydrogen mass flow rate injected from upstream to the incoming airflow was close to 1. Besides, the upstream injection flow mixed with the incoming airflow without any blockage. In contrast, downstream injection flow was blocked by the upstream injection flow from incoming airflow. Therefore, the upstream injection flow had comparatively good mixing and reaction circumstances, and the mixing of hydrogen and air from upstream played a significant role in combustion efficiency. Thus, it was essential to keep the upstream hydrogen injection flow in the best mixing and reacting status for achieving high combustion efficiency. With the upstream injection angle increasing, the interaction between upstream injection flow and incoming air flow was stronger. As a result, the mixing process of upstream injection flow was enhanced, so the combustion efficiency was enhanced. Furthermore, since there were two rows of injection holes and the arrangement of the injection holes is serial, the potential interference between the upstream and downstream injection flow was supposed to be noted when the upstream injection angle was relatively small, and the downstream injection angle was large. As can be seen in Figure 12, it was essential to achieve higher combustion efficiency by avoiding upstream and downstream injection flow too close.

Effect of downstream injection angle on combustion efficiency

Figure 13 represents the correlation between combustion efficiency and downstream injection angle. The combustion efficiency was obtained under the same upstream injection angle of 30°. When the downstream injection angle was 90°, combustion efficiency reached a maximum under this condition. It indicates that that the combustion efficiency had the same trend as the correlation between combustion efficiency and upstream injection angle.

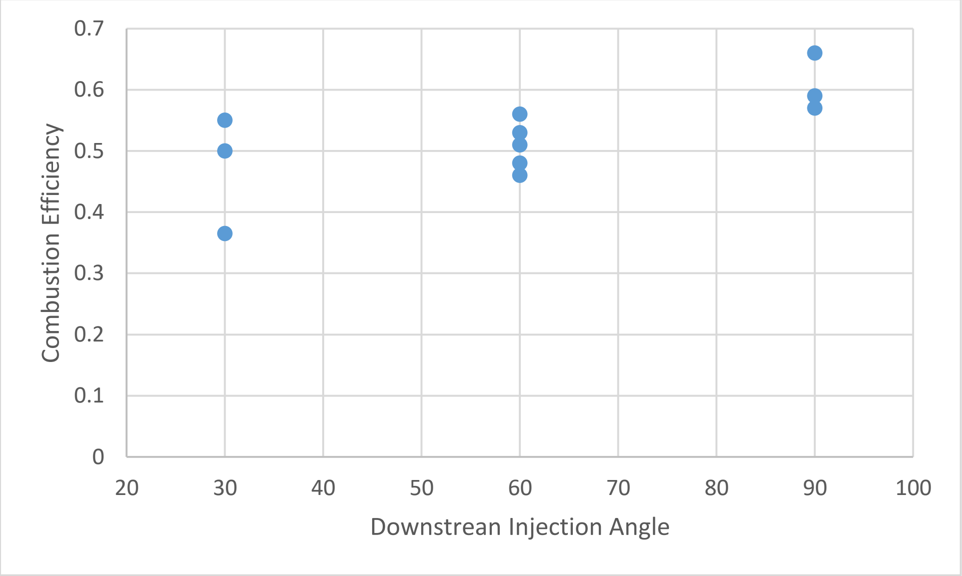

Figure 13 Correlation between combustion efficiency and downstream injection angle

This result seems contradictory to the previous conclusion that it was essential to achieve higher combustion efficiency by avoiding too close upstream and downstream injection flow. It needs to pay attention that the upstream injection angle of these results was 30°. It is a very small injection angle. In this situation, the potential interference between the upstream and downstream injection might happen and affect combustion efficiency. The detail would be discussed in the numerical simulation part.

2.5.2 Effect of arrangement of Injection hole to combustion efficiency

Zigzag arrangement injector has also been tested. Downstream injection holes were placed between two upstream holes alternately. The injector dimension (injection angle, diameter, pressure) is the same as the serial arrangement injector. The experimental result of the zigzag arrangement injector combustion efficiency was about 73%. It indicates that the zigzag arrangement injector combustion efficiency is 10-15% higher than the serial arrangement injector. The zigzag arrangement helps hydrogen injected from upstream avoid collision with hydrogen injected downstream and make the downstream injection flow directly mix with the incoming flow. More tests about Zigzag arrangement injectors with different injection angles were conducted in the numerical research part.

2.6 Summary

According to the experiment, the following results were obtained.

For the serial arrangement injector, the upstream injection angle row had crucial effects on combustion efficiency. The larger the upstream injection angle was, the higher the combustion efficiency was. Mixing hydrogen from upstream with air had main effects on combustion efficiency.

When the downstream injection angle was 90deg, combustion efficiency reached a maximum when the upstream injection angle was 30deg.

Interference between the two injection rows might have a different effect on the combustion efficiency for different cases.

The zigzag arrangement injector combustion efficiency was about 73% which is 10-15% higher than the serial arrangement injector. In theory, hydrogen injected from upstream can avoid interference with hydrogen injected from downstream. The downstream injection flow has better mixing circumstance for avoiding the blocking from upstream flow.

Further investigation of the correlation between the mixing process, the fuel distribution, and combustion efficiency was not conducted since the limitation of the measurement method. In order to understand the results revealed by the experiments, a numerical analysis was conducted.

3 Numerical model

In order to investigate the correlation between the mixing process, the fuel distribution, and combustion efficiency, a large eddy simulation solver, coupled with flamelet/progress variable chemical reaction model, was used based on the OpenFoam 2.3.X. Sandia Flame D was used for validating this solver for the feature of little or no local extinction. After the validation, the non-premixed hydrogen combustion processes in the model ramjet combustor were simulated with this solver.

3.1 Governing Equations

3.1.1 Turbulence model

In the present work, a large-eddy simulation was applied for reacting flow. The large scales motion containing energy are simulated numerically, while the small, unresolved scales (subgrid scales) motion and their interactions with the large scales are modeled. Then, the governing equations can be decomposed into LES form.

continuity:

$$\frac{\partial\bar{\rho}}{\partial t}+\frac{\partial}{\partial x_j}(\bar{\rho}\tilde{u}_j)=0 \tag{31}$$

momentum:

$$\frac{\partial\bar{\rho}\tilde{u}_i}{\partial t}+\frac{\partial}{\partial x_j}(\bar{\rho}\tilde{u}_i\tilde{u}_j)=-\frac{\partial\bar{p}}{\partial x_j}+\frac{\partial}{\partial x_j}\left(\bar{\rho}\nu\frac{\partial\tilde{u}_i}{\partial x_j}\right)+\frac{\partial}{\partial x_j}(\bar{\rho}\tau_{ij}) \tag{32}$$

state relation:

$$\bar{\rho}=\overline{f(\phi_1,\phi_2,\ldots)} \tag{33}$$

Here, ρ is the density, u_j is the velocity vector, p is the pressure, ν is the kinematic viscosity, δ_{ij} is the Kronecker symbol, Φ_i represents scalar quantities. The filtering operation is denoted by an overbar and Favre (density-weighted) filtering by a tilde. All unclosed transport terms in the momentum and scalar equations are grouped into the residual stress, τ_{ij}. The state relation closes the model. Scalar transport equation is based on the FPV model trajectory variables. It is dectcibed in the chemistry model section.

3.1.2 Subgrid-scale models

Since a large-eddy simulation was applied in this work, the subgrid momentum in Eq.(32) is needed to be modeled in order to represent the turbulent flow field. Boussinesq assumption [38], which assumes the transfer of turbulent kinetic energy from the resolved scales to the subgrid scales is similar to a molecular diffusion at a certain viscosity, was used to model the subgrid-scale (SGS) stresses τ_{ij} in Eq.(32). Because the Mach number in this study is less than 0.4, an assumption of SGS imcompressibility [39-40] was applied. Therefore, the SGS stresses τ_{ij} are modeled as:

$$\tau_{ij} \approx dev(\tau)_{ij} = \tau_{ij} - \frac{1}{3}\tau_{kk}\delta_{ij} = -2\left(\nu_{sgs} dev\left(\tilde{S}\right)_{ij} - \frac{1}{3}k_{sgs}\delta_{ij} \right) \tag{34}$$

$$k_{sgs} = -\frac{1}{2}\tau_{kk} \text{ and } \tilde{S}_{ij} = \frac{1}{2}\left(\frac{\partial \tilde{u}_i}{\partial x_j} + \frac{\partial \tilde{u}_j}{\partial x_i} \right)$$

where $dev\left(\tilde{S}\right)_{ij}$ is the deviatoric component of the resolved strain rate tensor $\tilde{S}_{ij}$, k_{sgs} is the subgrid kinetic energy, δ_{ij} is the Kronecker symbol, and ν_{sgs} is the subgrid eddy viscosity. In order to close the model, the ν_{sgs} and k_{sgs} are required to be calculated. Smagorinsky [41-42] gave the model to calculate the subgrid eddy viscosity ν_{sgs}. It is assumed in the model that the SGS eddies are isotropic and only the eddy size needs to be considered rather than the shape. Therefore, according to the units, the kinematic viscosity is considered as the product of the velocity gradients, which are obtained from the strain rate tensor $\tilde{S}_{ij}$, and a length scale of eddy that is calculated with the subgrid-scale filter length Δ and a dimensionless constant which gives the fraction of the filter width Δ to the subgrid-scale length. In the original Smagorinsky model, ν_{sgs} was defined as

$$\nu_{sgs} = \left(C_s \Delta\right)^2 \left|\tilde{S}_{ij}\right| \tag{35}$$

where $\left|\tilde{S}_{ij}\right| = \sqrt{2\tilde{S}_{ij}\tilde{S}_{ij}}$, $\Delta = \sqrt[3]{\delta x \delta y \delta z}$ is the filter width with δx , δy , δz the cell lengths under Cartesian coordinates, and C_s is the Smagorinsky constant defined as $C_s = \frac{1}{\pi}\left(3K_0 / 2\right)^{-0.75}$ with the Kolmogorov constant K_0 [41]. Smagorinsky model has been proven to be able to represent the energy transfer between resolved and SGS scales, but the results are highly depended by the Smagorinsky constant [40].

In order to increase the accuracy, Moeng et al. [43] developed a modified Smagorinsky model, which coupled the turbulent kinetic energy in the definition of subgrid eddy viscosity ν_{sgs} , and solved the turbulent kinetic energy k_{sgs} explicitly. In the model, ν_{sgs} was defined with the Prandtl-Kolmogorov relation [44-45],

$$\nu_{sgs} = C_k \Delta k_{sgs}^{1/2} \tag{36}$$

where C_k is a model constant. The subgrid kinetic energy k_{sgs} was then calculated by assuming the local equilibrium of the energy production $\tilde{S}_{ij}$: τ_{ij}, and dissipation $\frac{C_e}{\Delta} k_{sgs}^{3/2}$ in the subgrid scale according to the Kolmogorov hypothesis [46-47]:

$$\tilde{S}_{ij} : \tau_{ij} + \frac{C_e}{\Delta} k_{sgs}^{3/2} = 0 \, , \tag{37}$$

where C_e is a dissipation constant [43][47]. Eq.(34) was then substituted into Eq.(36):

$$\tilde{S}_{ij} : \left(-2\nu_{sgs} dev\left(\tilde{S}\right)_{ij} + \frac{2}{3} k_{sgs} \delta_{ij} \right) + \frac{C_e}{\Delta} k_{sgs}^{3/2} = 0 . \qquad (38)$$

With Eq.(38), Eq.(37) can be then derived into a quadratic equation about $k_{sgs}^{1/2}$ [43]:

$$k_{sgs}^{1/2} \left(\frac{C_e}{\Delta} k_{sgs} + \frac{2}{3} tr\left(\tilde{S}_{ij}\right) k_{sgs}^{1/2} - 2C_k \Delta \left(dev\left(\tilde{S}\right)_{ij} : \tilde{S}_{ij} \right) \right) = 0 , \qquad (39)$$

$$a k_{sgs} + b k_{sgs}^{1/2} - c = 0 , \qquad (40)$$

where $a = \frac{C_e}{\Delta}$, $b = \frac{2}{3} tr(\tilde{S}_{ij})$ with the trace of strain rate tensor, and $c = 2C_k \Delta \left(dev\left(\tilde{S}_{ij}\right) : \tilde{S}_{ij} \right)$. Due to incompressibility assumption in the SGS, the coefficients *b* and *c were* reduced to $b = 0$ and $c = C_k \Delta \left|\tilde{S}_{ij}\right|^2$ respectively. The subgrid kinetic energy was then calculated as:

$$k_{sgs} = \frac{C_k}{C_e} \Delta^2 \left|\tilde{S}_{ij}\right|^2 , \qquad (41)$$

and the subgrid eddy viscosity ν_{sgs} was:

$$\nu_{sgs} = C_k^{3/2} C_e^{-1/2} \Delta^2 \left|\tilde{S}_{ij}\right| . \qquad (42)$$

The relation between the original Smagorinsky constant C_s, the dissipation constant C_e and the model constant C_k can be estabished as follow,

$$C_s = C_k^{3/4} C_e^{-1/4} . \qquad (43)$$

In this work, the dissipation constant C_e was set as $C_e = 0.93$ [43][47], and the model constant C_k was selected as $C_k = 0.094$ [43]. Therefore, the applied Smagorinsky constant C_S in this work was $C_s = 0.17$, which in the usual range for reacting flows [46][48].

3.1.3 Chemistry models

The steady flamelet solutions are given in mixture fraction *Z,* and the reaction progress variable *C*.

The scalar transport equations for *Z* and *C* carried in a simulation is given by

$$\frac{\partial\bar{\rho}Z}{\partial t}+\nabla\cdot(\bar{\rho}\tilde{u}Z)=\nabla\cdot(\bar{\rho}\tilde{\alpha}_Z\nabla Z) \tag{44}$$

$$\frac{\partial\bar{\rho}C}{\partial t}+\nabla\cdot(\bar{\rho}\tilde{u}\mathrm{C})=\nabla\cdot(\bar{\rho}\tilde{\alpha}_C\nabla C)+\bar{\rho}\omega_C \tag{45}$$

where tilde α_c is the turbulent diffusivity. Filtered combustion variables are obtained by integrating chemical state relationships over *Z* and *C*'s joint subgrid PDF.

$$T=\int T(Z,C)P(Z,C)dZdC \tag{46}$$

$$\omega_C=\int \omega_C(Z,C)P(Z,C)dZdC \tag{47}$$

$$Y_i=\int Y_i(Z,C)P(Z,C)dZdC \tag{48}$$

The chemical state relationships for the temperature *T*, and the chemical source term:

$$Y_i=Y_i(Z,C) \tag{49}$$

$$T=T(Z,C) \tag{50}$$

$$\omega_C=\omega_C(Z,C) \tag{51}$$

are obtained from the steady-state flamelet library.

The joint subgrid PDF is modeled by

$$P(Z,C) = P(C|Z)P(Z) \tag{52}$$

where beta function gives tilde P(Z).

Delta function is described tilde *P(C|Z)*

$$P(C|Z) = \delta(C - C|Z) \tag{53}$$

C|Z is given by the steady-flamelet solution

$$C|Z = C(Z,\xi) \tag{54}$$

Here, ξ is any variable that can be used to parameterize the family of flamelet solutions.

The reference value of the chosen parameter, ξ, should follow the constraint

$$C = \int C(Z,\xi)P(Z)dZ \tag{55}$$

Flamelet solution can be computed from the transport equation with this constraint. Any selection of ξ can be used as long as it satisfies this constraint.

At last, filtered chemical variables as functions of the quantities from LES is provided by lookup tables:

$$Y_i = Y_i(Z, Z''^2, C) \tag{56}$$

$$T_i = T_i(Z, Z''^2, C) \tag{57}$$

The computational cost of the flamelet/progress-variable approach is only greater than the steady-flamelet model since the functions in (53) (54) are precomputed and stored in the library before running a simulation. The major additional cost comes from solving the transport equation for the progress variable.

In the present work, the flamelet/progress variable simulations were carried out using a solver called fpvFoam, which is based on OpenFOAM-2.3.x, and the equations were solved using a PIMPLE algorithm in the finite volume method. The 1-D laminar counterflow diffusion flamelet solutions are obtained from the code "FlameMaster" developed by Pitsch [49].

3.2 Validation

3.2.1 Sandia Flame D

In order to validate the flamelet/progress variable code, Sandia Flame D was selected as a validation case.

The Sandia Flame D, as shown in Figure 14, is a partial premixing flame. The partial premixing fuel produces a robust flame. Thus, the flames could be operated under high Reynolds number inlet flow with little or no local extinction. The high Reynolds number makes the mixing rates are high enough to keep flames burn as diffusion flames. The flame has a single reaction zone near the stoichiometric mixture fraction and no significant premixed combustion in the main fuel-rich injection flow. Therefore, Sandia Flame D can be considered as pure non-premixed diffusion flame. It corresponds to the flamelet assumption. It separates turbulence and chemistry interaction. Thus, it is very suitable for validating the chemical model used in the present research.

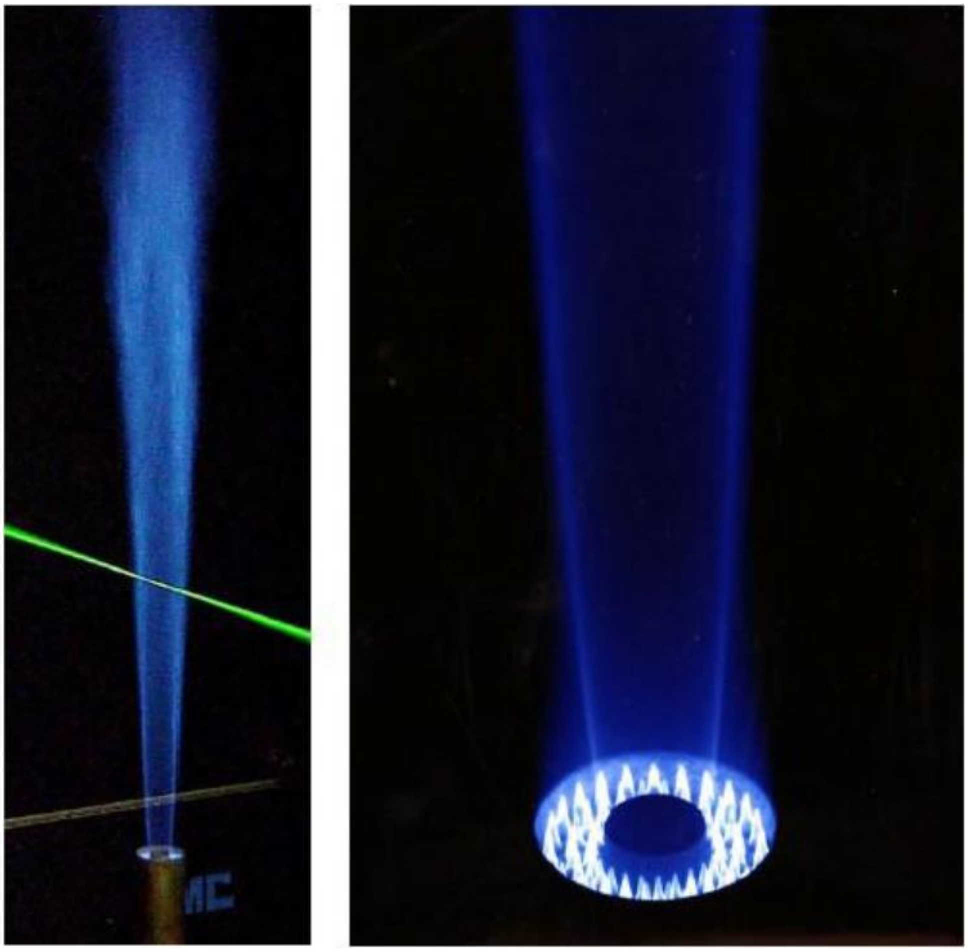

Figure 14 Sandia Flame D - view of the flame (left); zoom of the vicinity of the

nozzle (right) [32]

A schematic view of the Sandia Flame D central and pilot burners located 15 cm above the vertical wind tunnel exit is shown in Figure 15. Configuration is listed in Table 5. The flame is unconfined. [32]

Table 5 Configuration of Sandia Flame D burner

Main jet inner diameter(D)	7.2 mm
Pilot flame annulus inner diameter	7.7 mm (wall thickness = 0.25 mm)
Pilot flame annulus outer diameter	18.2 mm
Burner outer wall diameter	18.9 mm (wall thickness = 0.35 mm)
Wind tunnel exit	30x30 cm

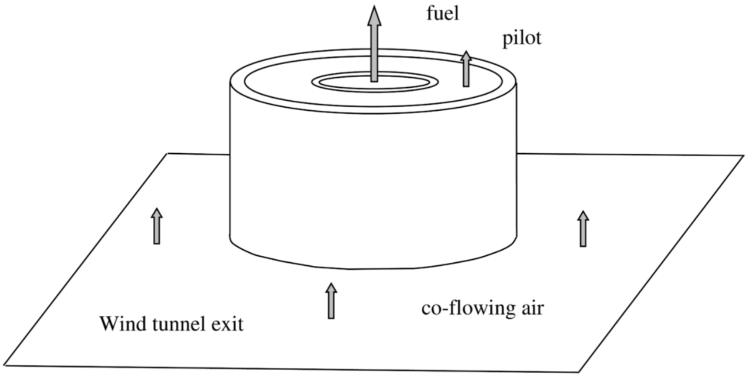

Figure 15 Scheme of the flow domain geometry [50]

Table 6 Inlet velocity of Sandia Flame D

Fuel velocity	49m/s
Pilot flame	11.4m/s
Coflow velocity	0.9m/s

The Sandia D Flame fuel is a mixture of 25% methane (CH4) and 75% air in volume. The mixture of C_2H_2, H_2, air, CO_2, and N_2, is used as pilot flame fuel. The pilot flame is operated under lean condition, the equivalence ratio is 0.77, and the flow rate is scaled as ~6% of the power of the main flame. The burner exit is positioned approximately 15 cm above the exit of the vertical wind tunnel [32].

3.2.2 Pre-processing

Base on the information above, a computational domain was made. The computational domain is a cylinder with 65D in height and 0.3m in radial direction. A 40D length tube was added to the inlet to generate the turbulent flow. The nodes number is 6341716, as shown in Figure 16.

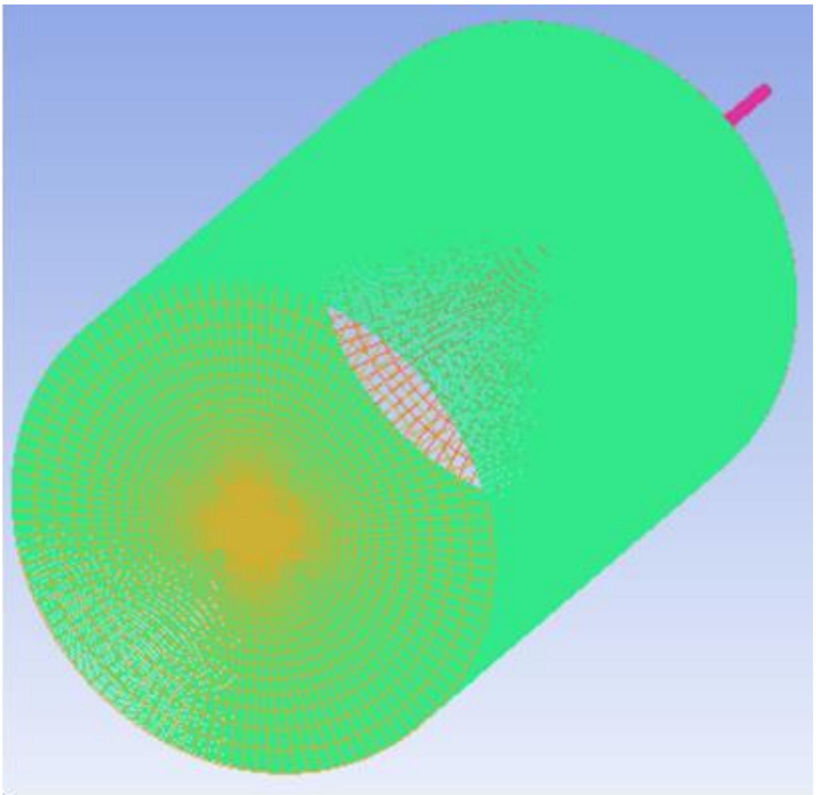

Figure 16 Mesh of computational domain

In the present research, there are two eddy generating sources which are needed to be noted. The first is the tube wall. The second is the shear layer generated by the fuel injection flow and pilot flame flow. The finer mesh was distributed at these positions. The directly simulated eddy focuses on the eddy formed by the fuel injection flow. O grid and Hexahedral meshes were used in the domain. The first layer of the tube was set as y+ around 30. Maximum mesh size in the tube part is around 0.2mm. The estimation of fully developed turbulence length scale in the tube is about 0.3mm~0.5mm. The same mesh setting was also used around the injection flow area.

The fuel tube inlet was set as a velocity inlet with 10% random fluctuation. Pilot flame inlet and the co-flow inlet was set as laminar velocity inlet for the low Reynolds number. All inlet boundary was set without boundary layer. The outlet boundary condition was set as pressure boundary. The walls in the domain was set as non-slip boundary. A similar composition of pilot flow was obtained from a laminar diffusion flame calculation with the present fuel-air boundary conditions, equal species diffusivities, and a relatively low strain rate (a ~ 20/s) 0.27 mixture fraction [32]. The detailed boundary conditions are shown in Table 7. The chemical reaction mechanism used here contains 28 species and 72 reactions, originally proposed by N. Peters et al. [51]. The internal field was initialized with velocity and scalar field equal to zero.

Table 7 Boundary conditions

	Fuel Inlet	Pilot inlet	Co-flow inlet	Outlet
Velocity (m/s)	49.6±10%	11.4	0.9	0 Gradient
Pressure (MPa)	0 Gradient	0 Gradient	0 Gradient	0.1
Z	1	0.27	0	0
C	0	0.113	0	0

The FPV approach begins with building the flamelet library. The flamelet parameter monotonically parameterizes all the steady flamelet solutions, including the weak reaction branch.

Previous research [52] defined the flamelet parameter of methane combustion as the linear combination of product mass fraction: the CO_2 CO, H_2O, and H_2 at $Z=Z_{st}$. It is found that the progress variable $C(Z_{st})$ varies (decrease) monotonically from equilibrium to complete extinction and hence satisfied the flamelet parameter criterion.

In the present study, flamelets solutions were obtained from the code "FlameMaster." Variation of $C(Z_{st})$ along all the flame states is shown in Figure 17. It was found that although the overall variation is monotonic, the region in the proximity to the equilibrium state showed the existence of saddle points. For Sandia Flame D, fuel also includes an oxidizer. When the scalar dissipation rate was low, the flamelet solution was affected significantly by H2O and H2 from premixed combustion. These saddle points prevented a monotonous parameterization. Thus these saddle points needed to be removed from the flamelet solutions if $C(Z_{st})$ was used as a flamelet parameter. Thus, to keep the progress variable definition monotonically, a maximum value of CO_2 and CO mass fractions linear combination has been chosen for the present study. The progress variable is given by:

$$C = Y_{CO} + Y_{CO_2} \tag{58}$$

With this definition of progress variable, the C_{max} is truly monotonic along with the whole flamelet solution. Hence, in the present study, the flamelet parameter was defined by C_{max}.

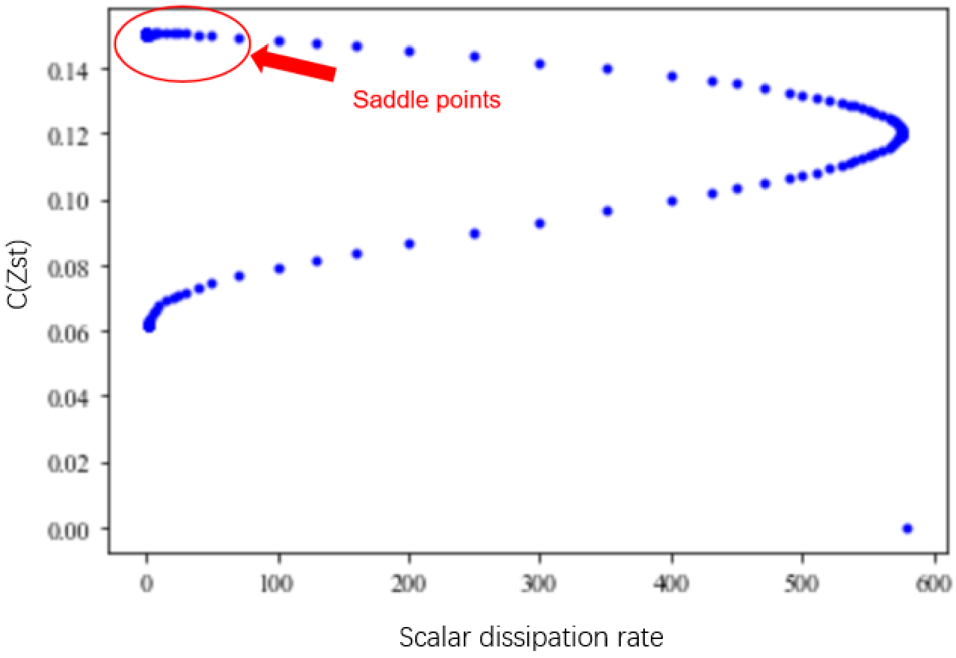

Figure 17 Variation in the parameterization of flamelets along with the entire solution space

3.2.3 Results

Figure 18 toFigure 23 provide the radial profiles for mean and root mean squared(RMS) of mass fraction of CO, CO_2, H_2O, OH, velocity and temperature. The velocity profile was close to the experiment result distribution. It indicated that, the numerical setting and mesh setting was qualified for present research. At the height of 15D, the species mass fraction, velocity and temperature profiles agreed well with the experimental data. The CO mass fraction around 10mm to 15mm and the CO2 mass fraction around 5mm to 10mm on radial direction tended to be over-predicted. The pilot flame parameter could cause it since the pilot flame parameter was mapped on the pilot flame inlet boundary. In general, the performance of the fpvFoam was evaluated in Sandia D flame. The results from the fpvFoam were approximately identical with the experiment result, implying that the fpvFoam model was valid.

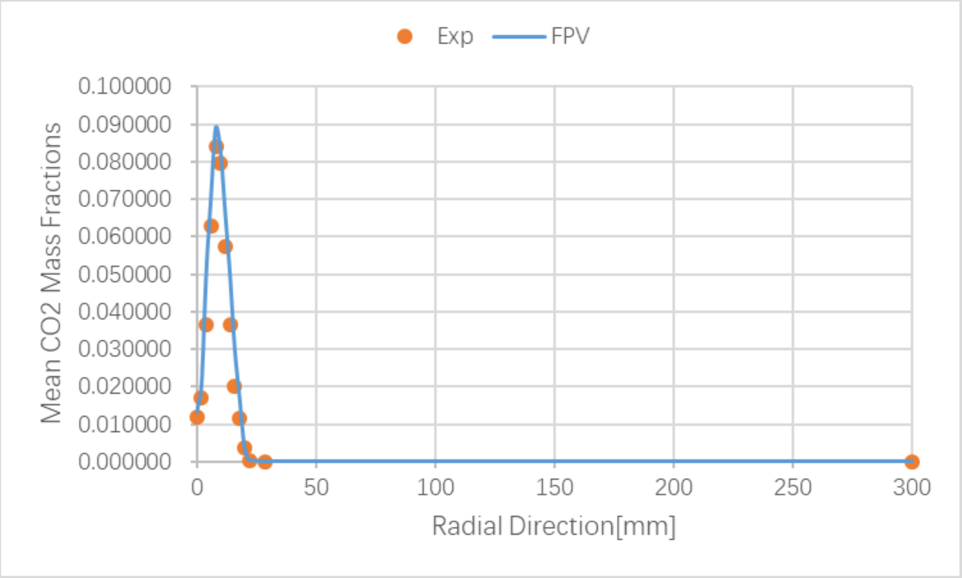
Exp
FPV
Mean CO2 Mass Fractions
0.100000
0.090000
0.080000
0.070000
0.060000
0.050000
0.040000
0.030000
0.020000
0.010000
0.000000
0
50
100
150
200
250
300
Radial Direction[mm]

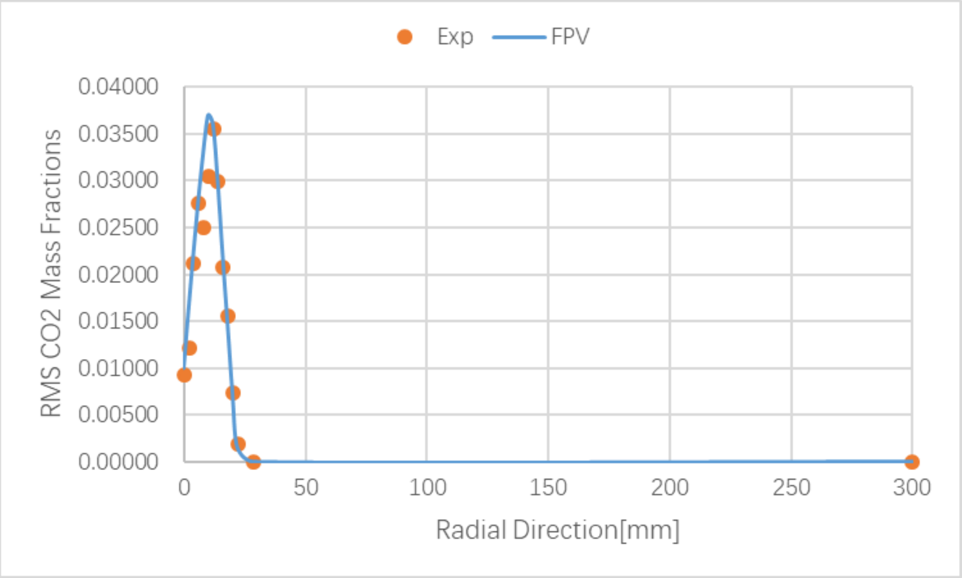

Figure 18 Radial profiles of CO_2 mass fraction

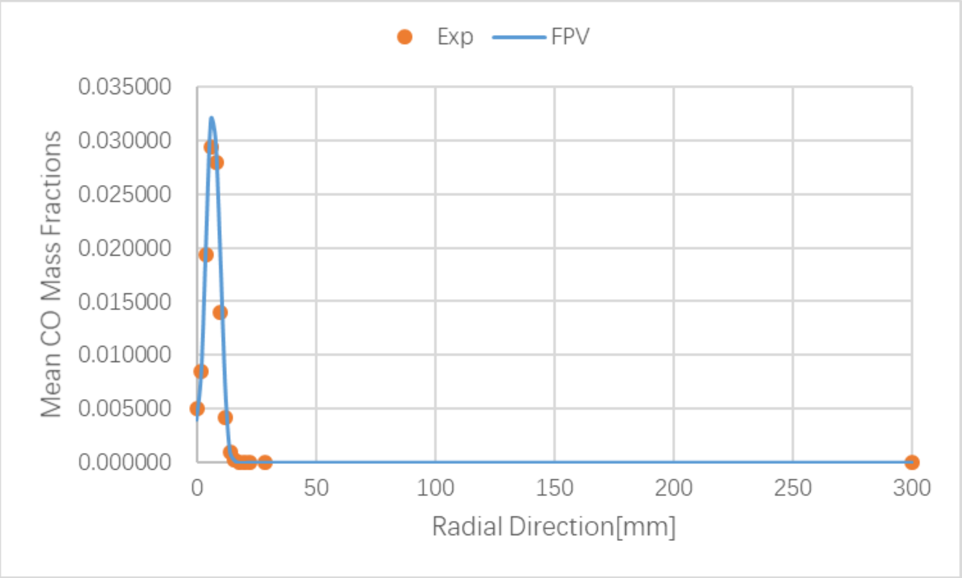

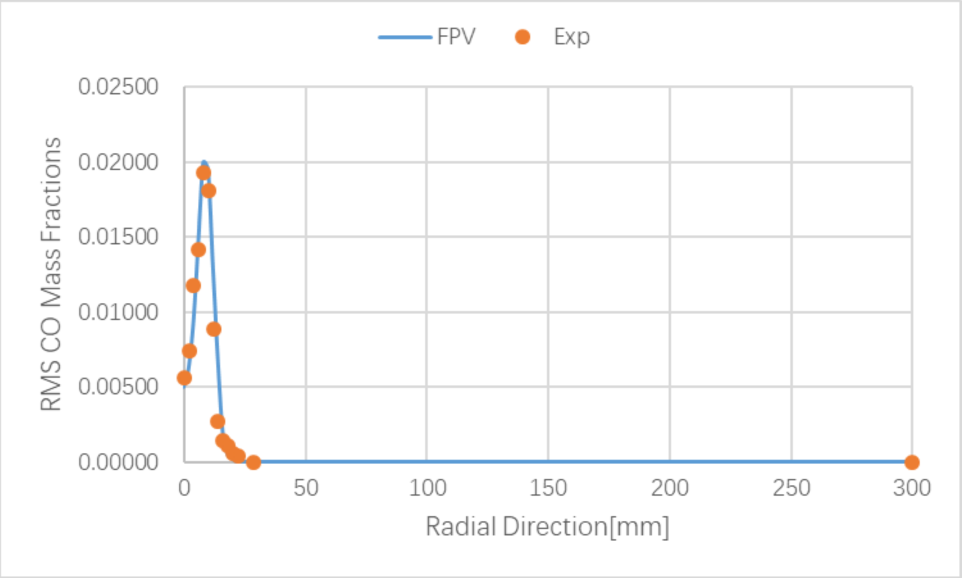

Figure 19 Radial profiles of CO mass fraction

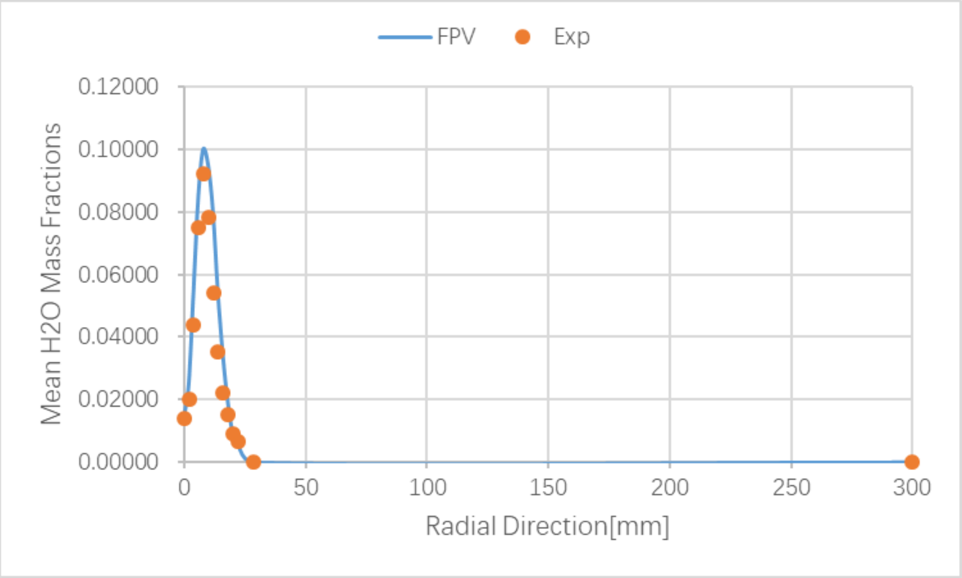

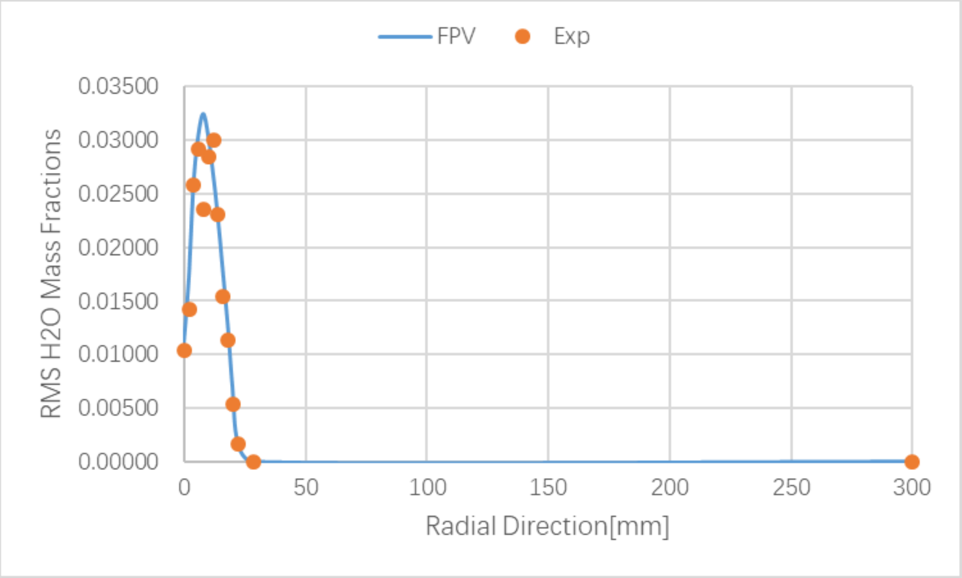

Figure 20 Radial profiles of H_2O mass fraction

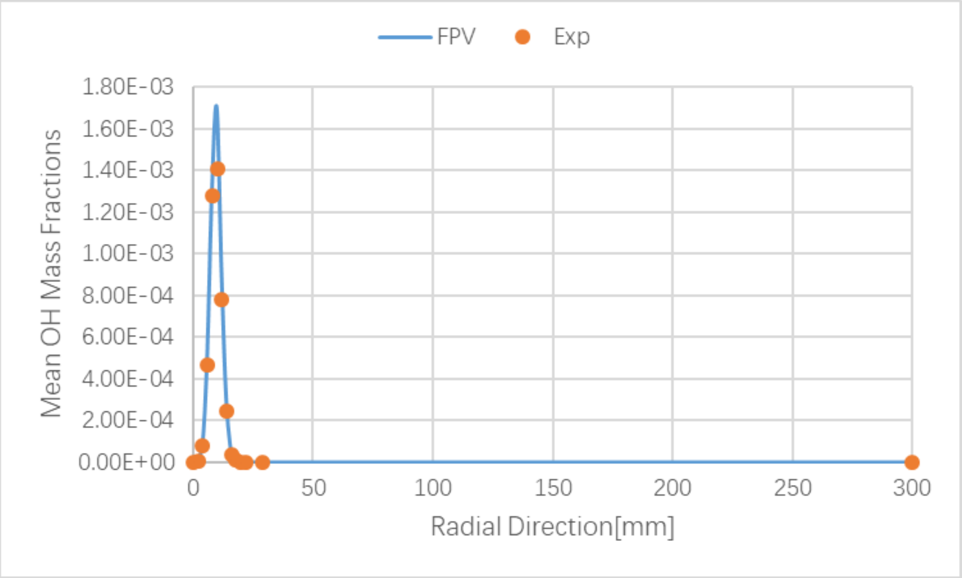

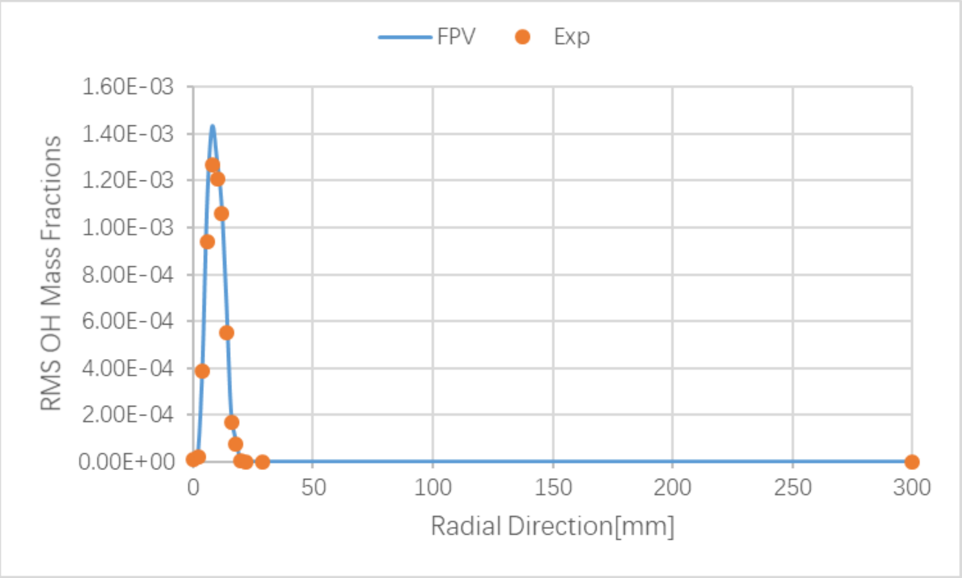

Figure 21 Radial profiles of OH mass fraction

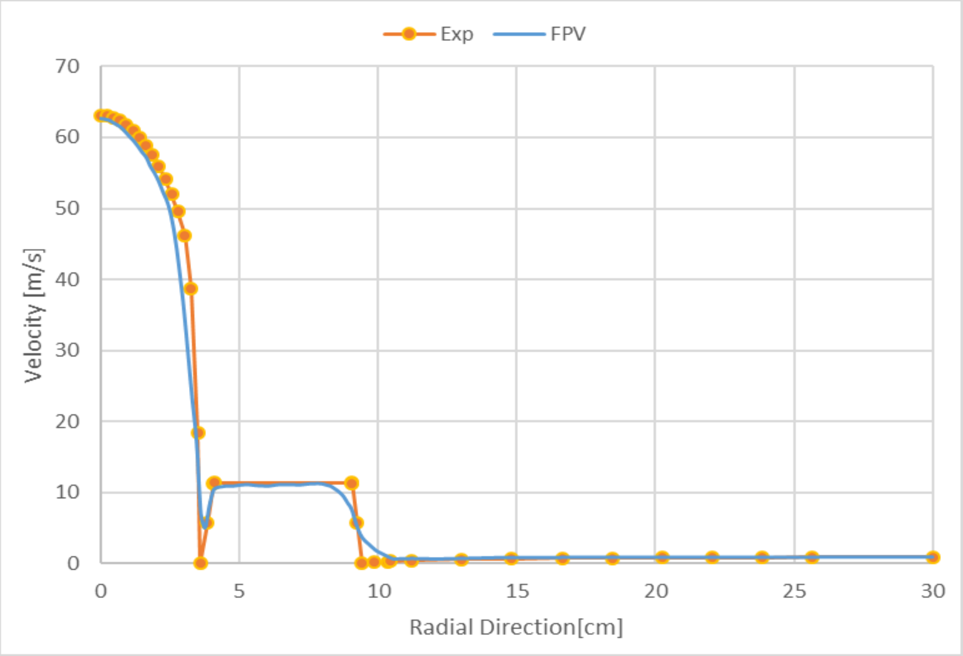

Figure 22 Velocity distribution on radial profiles

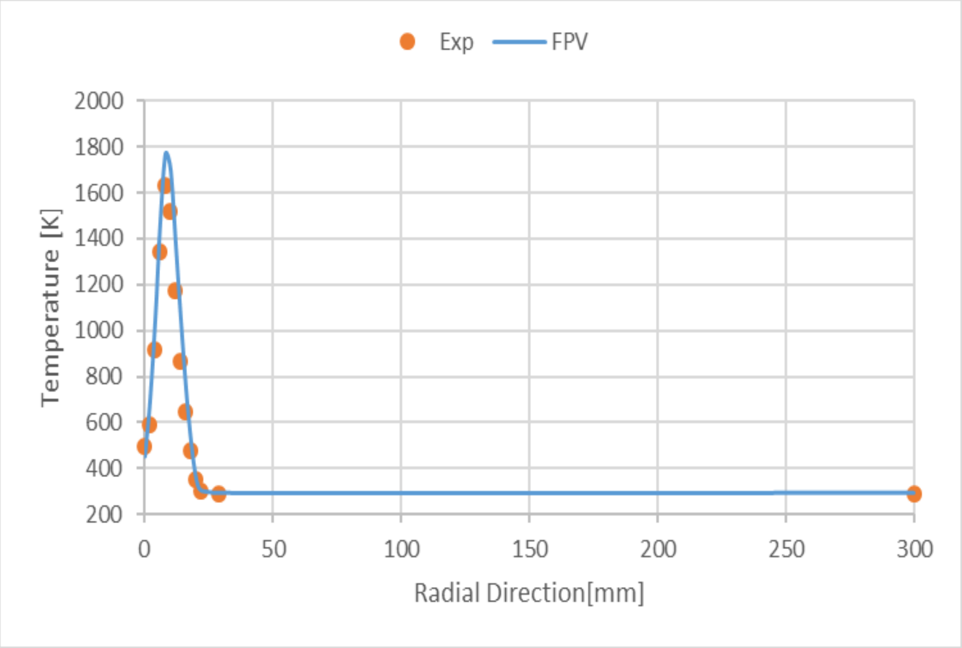

Figure 23 Temperature distribution on radial direction

3.3 Summary

This chapter presented detailed information about the numerical model to investigate the correlation between the mixing process, fuel distribution, and combustion efficiency. Sandia Flame D was selected as the validation case for the unique features of little or no local extinction. The results from the simulation had good agreement with the experiment results. Thus, the numerical model was considered validated. In the following, some preparation for the simulation of the model ramjet combustor had to be done first.

4 Generation of hydrogen flamelet library and initial flow conditions

In this section, preparation was made for the simulation of the model ramjet combustor. A hydrogen flamelet library was generated for the flamelet/progress variable approach and tested using a detailed chemistry 1-D counterflow flame result. The inlet velocity distribution has also been tested to determine the inlet condition. (laminar or turbulent).

4.1 Generation and a priori tests of hydrogen flamelet solution

In this work, the flamelets library was generated with a 1-D counterflow diffusion flame flamelets solution. The configuration was shown in Figure 24 [24]. Through opposed nozzles, air and hydrogen flow form a diffusion flame in the middle part along its centerline. The temperature, the species composition at the nozzles, and the operating pressure were chosen to match the condition used in the model ramjet combustor, which follows the condition in the PCTJ afterburner under cruising status. The detailed chemical mechanism of hydrogen used for calculating the flamelet solutions was with nine species and nineteen reactions which is shown in Table 8. The detail setting is in Table 9, and the flamelets solutions were obtained from the code "FlameMaster."

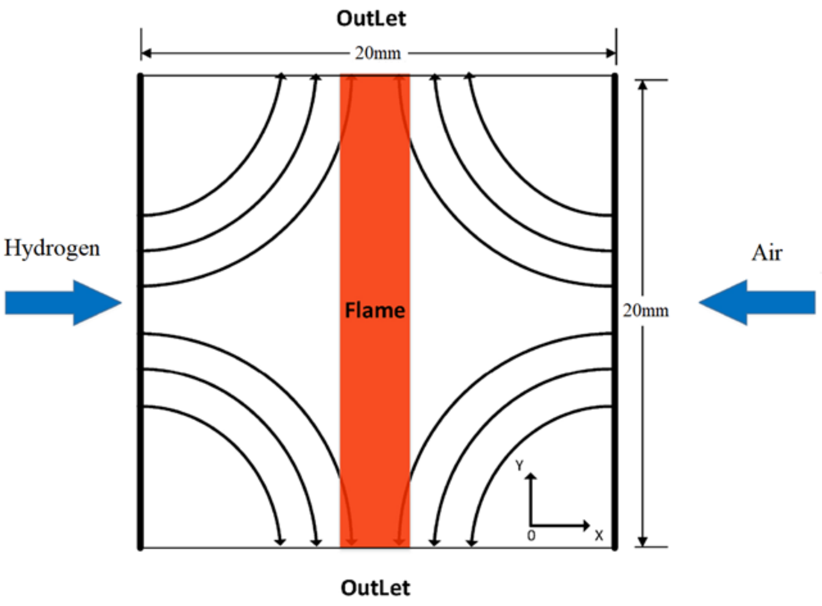

Figure 24 The computational domain used for the two-dimensional counterflow flame

Table 8 Detailed chemical mechanism of hydrogen [51]

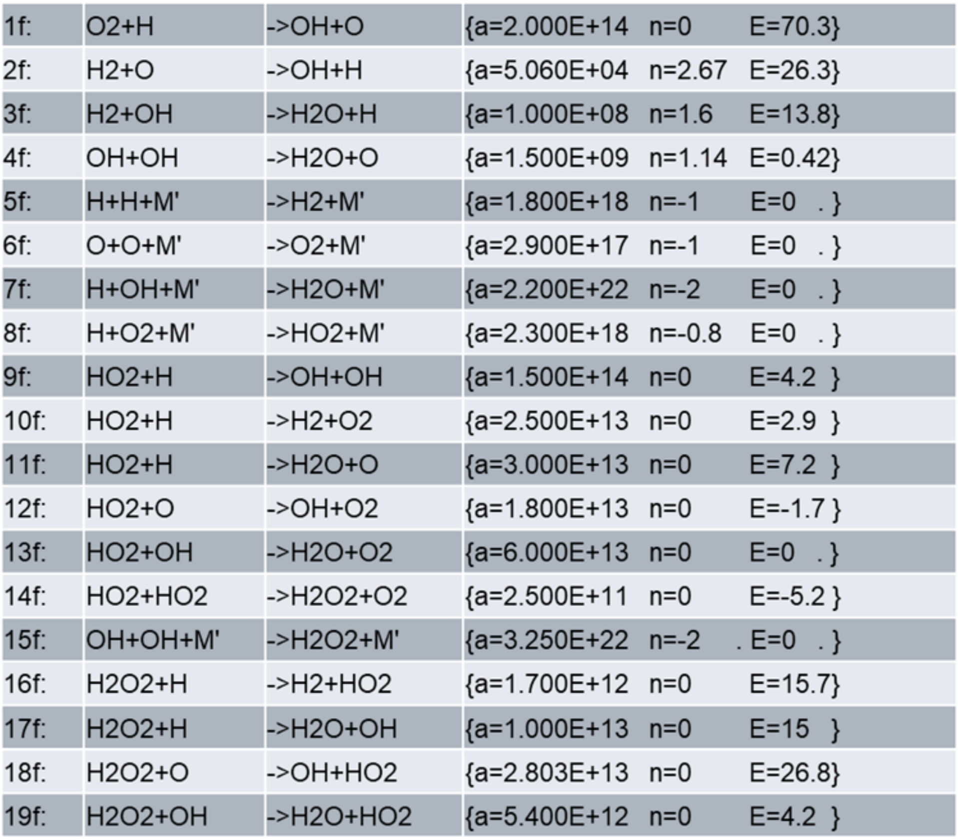

1f:	O2+H	->OH+O	{a=2.000E+14 n=0 E=70.3}
2f:	H2+O	->OH+H	{a=5.060E+04 n=2.67 E=26.3}
3f:	H2+OH	->H2O+H	{a=1.000E+08 n=1.6 E=13.8}
4f:	OH+OH	->H2O+O	{a=1.500E+09 n=1.14 E=0.42}
5f:	H+H+M'	->H2+M'	{a=1.800E+18 n=-1 E=0 . }
6f:	O+O+M'	->O2+M'	{a=2.900E+17 n=-1 E=0 . }
7f:	H+OH+M'	->H2O+M'	{a=2.200E+22 n=-2 E=0 . }
8f:	H+O2+M'	->HO2+M'	{a=2.300E+18 n=-0.8 E=0 . }
9f:	HO2+H	->OH+OH	{a=1.500E+14 n=0 E=4.2 }
10f:	HO2+H	->H2+O2	{a=2.500E+13 n=0 E=2.9 }
11f:	HO2+H	->H2O+O	{a=3.000E+13 n=0 E=7.2 }
12f:	HO2+O	->OH+O2	{a=1.800E+13 n=0 E=-1.7 }
13f:	HO2+OH	->H2O+O2	{a=6.000E+13 n=0 E=0 . }
14f:	HO2+HO2	->H2O2+O2	{a=2.500E+11 n=0 E=-5.2 }
15f:	OH+OH+M'	->H2O2+M'	{a=3.250E+22 n=-2 . E=0 . }
16f:	H2O2+H	->H2+HO2	{a=1.700E+12 n=0 E=15.7}
17f:	H2O2+H	->H2O+OH	{a=1.000E+13 n=0 E=15 }
18f:	H2O2+O	->OH+HO2	{a=2.803E+13 n=0 E=26.8}
19f:	H2O2+OH	->H2O+HO2	{a=5.400E+12 n=0 E=4.2 }

Table 9 Boundary setting of hydrogen flamelet solution

Temperature of hydrogen	300K
Temperature of air	900K
Operating pressure	0.3MPa

The result of flamelet solutions has been generated as different scalar dissipation rates, as shown in Figure 25.

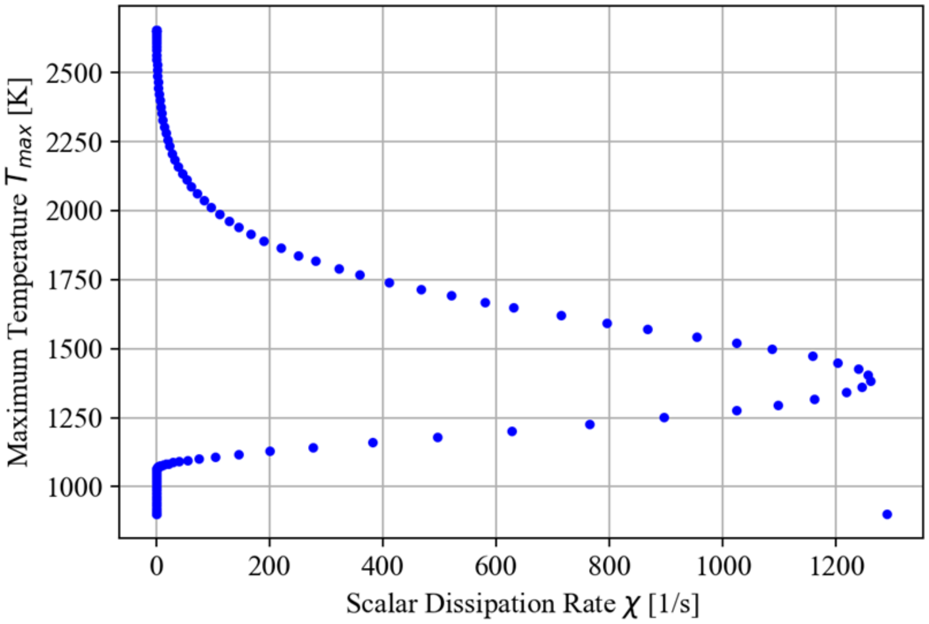

Figure 25 The hydrogen flamelet solution (maximum temperature vs. scalar dissipation rate)

Commonly, the combination of chemical species or temperature is defined as progress variable *C*. The combination should follow some principles, although the definition is not unique.

(a) The definition of *C* should be solved by transport equation conveniently.

(b) The reactive scalars in *C* should be time depended.

(c) All reactive scalars in *C* should be independent of one another.

(d) The definition of *C* should parameterize all the flamelet monotonically.

In the present study, the hydrogen flamelet solution clearly has two branches. The upper and lower branch represents the intensive reaction and weak reaction respectively. In the weak reaction branch, the radical species reaction ratio is comparatively slow. With the heat accumulation, the temperature reaches the ignition point, and the intensive reaction starts. The reaction goes into the upper branch. Therefore, the progress variable representing hydrogen autoignition should include both weak and intensive reaction brach species. Meanwhile, the combination must ensure that the progress variable *C* increases or decreases monotonously from initial conditions up to equilibrium [53].

H_2O and HO_2 were chosen to represent the intensive reaction branch and weak reacting branch in this work. H_2O is the final production of intensive reaction. HO_2 is the initial intermedia species of weak reaction. They are the best representative of each branch. The composition of the progress variable was defined as the sum of the mass fractions of H_2O and HO_2 [53]:

$$C = Y_{HO_2} + Y_{H_2O} \tag{59}$$

This definition is a prevalently used and effective combination for progress variable *C* of the hydrogen autoignition combustion process.

Before the simulation of the model ramjet combustor, the accuracy of the hydrogen flamelet library was evaluated through the a priori analysis. First, 1-D counterflow flames were simulated with the detailed chemistry(DC) solver of reactingFoam [31] under operating conditions, and the mixture fraction *Z* was extracted from the DC results. The FPV approach extracted species mass fractions and thermodynamic quantities from the flamelet library as functions of mixture fraction *Z*. Then, the quantities of interest in the flamelet library were compared to those from detailed chemistry simulations to validate the accuracy of the flamelet library. The test case strain rate was 200. The strain rate a is defined by the following equation:

$$(u_{H_2} + u_{air}) / H \tag{60}$$

where u_{h2} and u_{air} are the exit velocities of the fuel and oxidizer streams, respectively, and *H* is the distance between the two nozzles.

Figure 26 toFigure 32 shows the profiles of temperature and species mass fraction as a function of the mixture fraction. The comparison between the detailed chemistry and flamelet results has been shown in these figures. Figure 26 shows that the temperature distribution of the flamelet result showed good agreement with the DC result. Figure 27,Figure 28,Figure 30 toFigure 32 show that the major mass fraction profiles of species including H2O, OH, O, H2O2, and HO2 obtained from the flamelet models generally agreed with the detailed chemistry simulation results. However, in Figure 29, considerable discrepancies were observed between the flamelet model and DC results for intermediate species H.

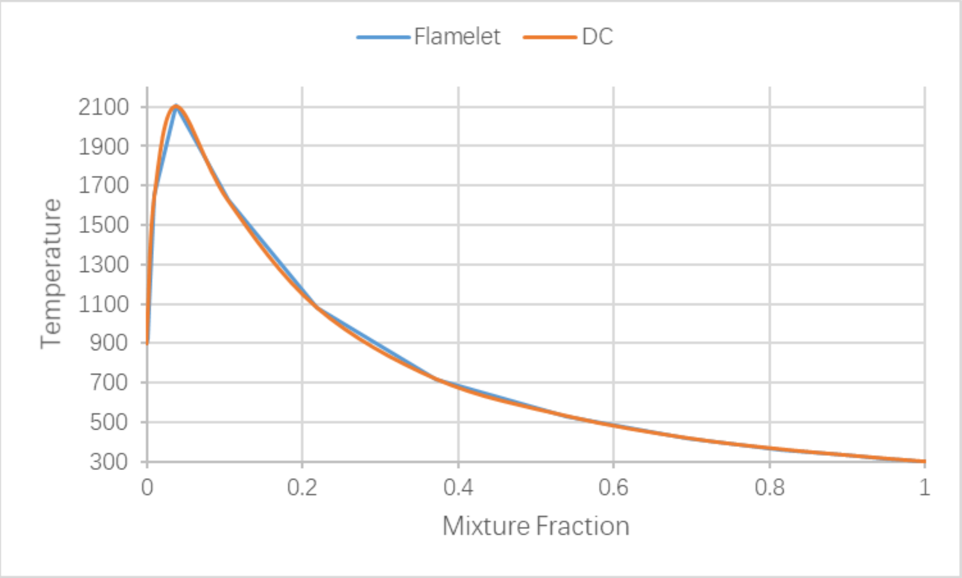

Figure 26 Profiles of temperature as a function of mixture fraction for flamelt and DC models

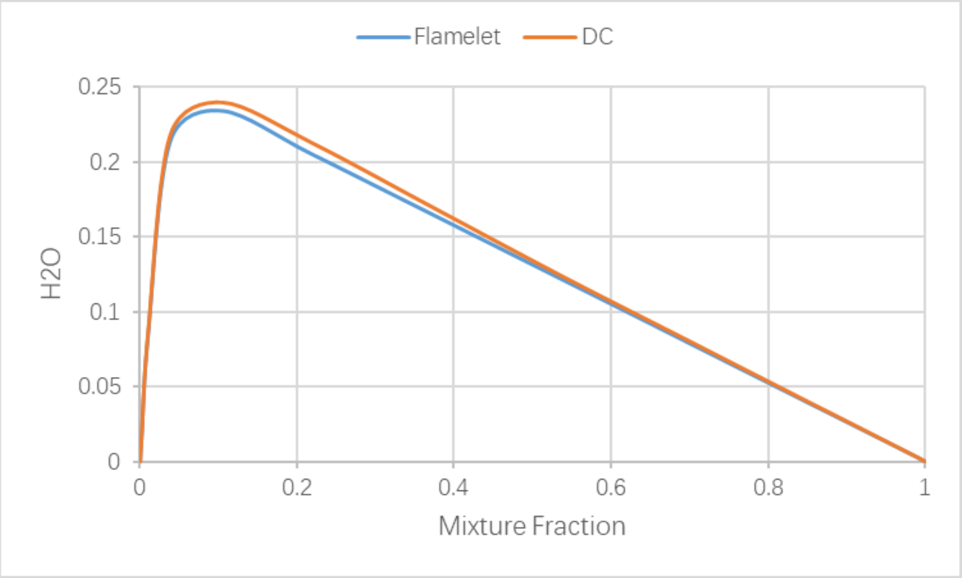

Figure 27 Profiles of H_2O as a function of mixture fraction for flamelt and DC models

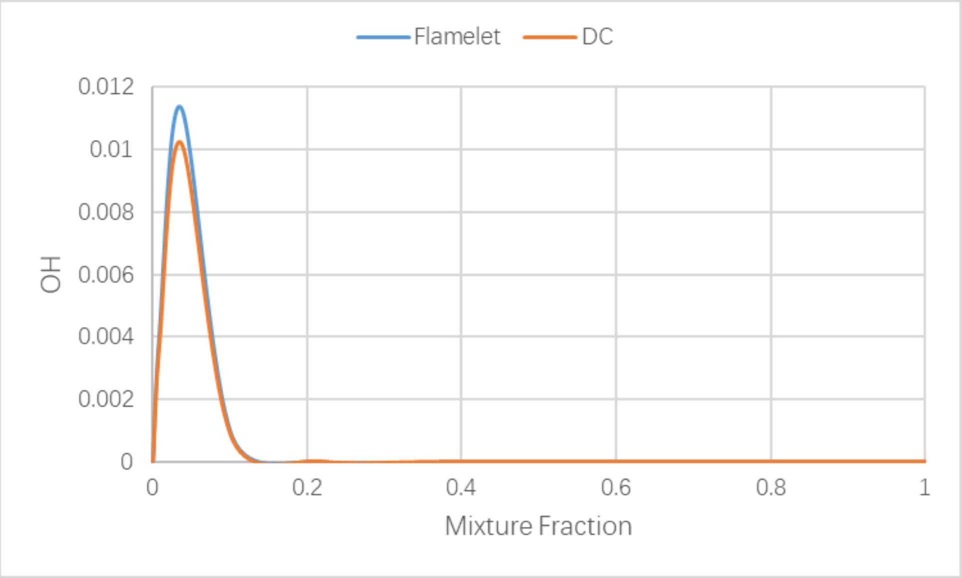

Figure 28 Profiles of OH as a function of mixture fraction for flamelt and DC models

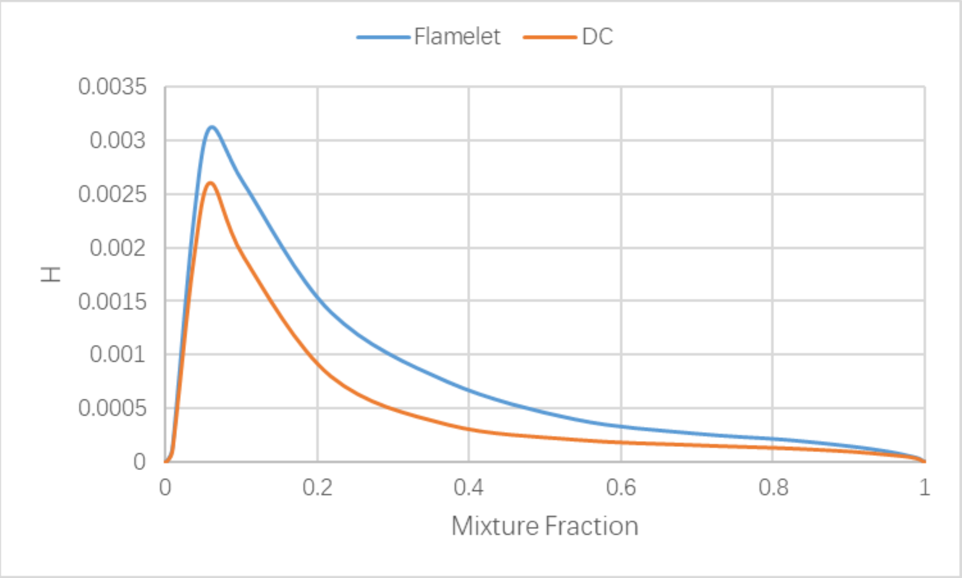

Figure 29 Profiles of H as a function of mixture fraction for flamelt and DC models

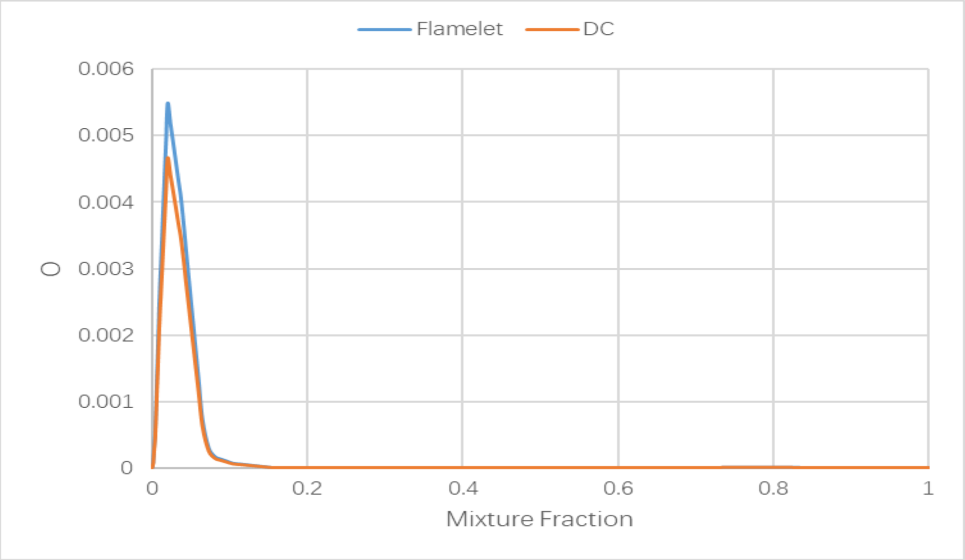

Figure 30 Profiles of O as a function of mixture fraction for flamelt and DC models

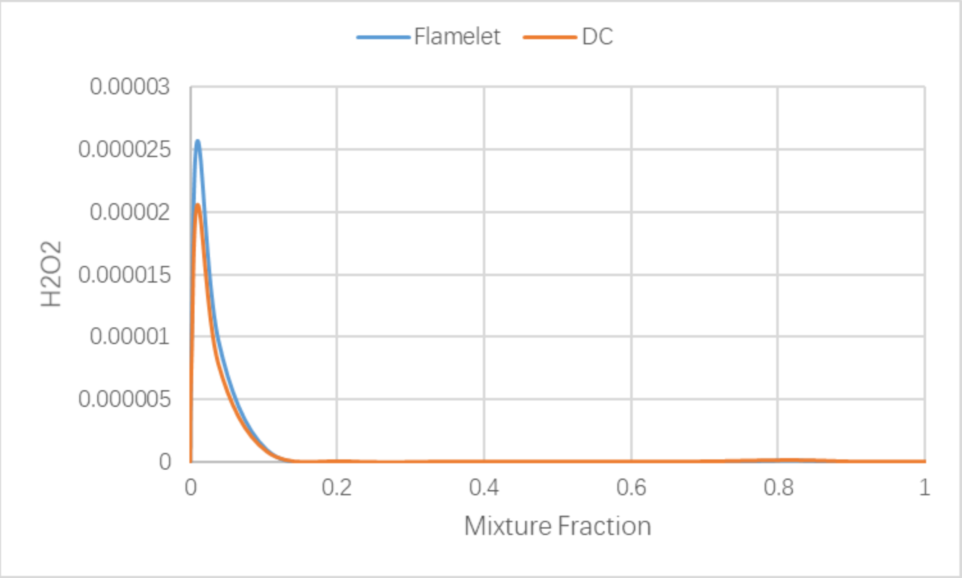

Figure 31 Profiles of H_2O_2 as a function of mixture fraction for flamelt and DC models

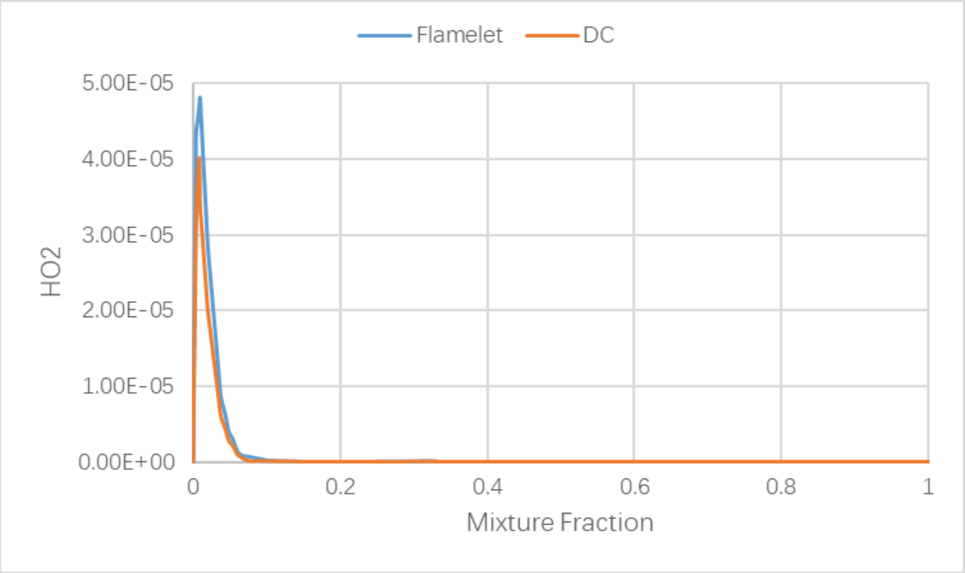

Figure 32 Profiles of HO_2 as a function of mixture fraction for flamelt and DC models

Two facts caused the gap between the flamelet results and DC results. Firstly, the transport model used in the simulation was not able to provide a precise rustle of all species simultaneously. Especially for the intermedia species, like H, which is susceptible during the reaction, and the quantity is meager. Secondly, the minor species such as intermedia species H in the weak reaction process were hard to predict as it was not incorporated in the progress variable. Thus, it was difficult to achieve a very accurate estimation.

In summary, good agreement was achieved between the detailed chemistry and flamelet results, despite the H mass fractions showed a minor discrepancy. It confirmed that the flamelet library was adequate for hydrogen flames.

4.2 Inlet condition of model ramjet combustor

In order to compare the numerical simulation and experimental results, a suitable simulation model was established. For the present study, the most crucial parameter was the inlet flow condition. A number of researches about the effect of incoming flow on combustion stability have been conducted. The bluff-body flame holder was one of the most concerning types. The model ramjet combustor used in the present study was connected directly to the wind tunnel outlet with a flange. The inner diameter of the wind tunnel outlet is 200mm, and the model ramjet combustor inner cross-section is a 48mm × 32mm rectangular. The installation position of the model ramjet combustor on the flange was located along the central line of the wind tunnel outlet and the combustor. Thus a suddenly narrowed tube was constructed by the wind tunnel outlet and the combustor inlet. According to the continuity equation, it can be estimated that the airflow velocity jumped from about 3m/s in the outlet of the wind tunnel to about 50m/s in the inlet of the model combustor under 900K of temperature, 0.3MPa of pressure, and the experiment mass flow rate of air. With the estimation of step velocity increasing, the flow shrinking at the model combustor inlet was formed. In order to validate this analysis, a test numerical simulation case with rhoPimpleFoam [31] has been set.

The test case domain is a 200mm diameter cylinder connect with a 48mm × 32mm cross-section rectangular, nodes number 3266975. The length is 200mm and 100mm, respectively, shown in Figure 33. The inlet flow at the cylinder side was set mass flow rate of 0.102kg/s. The detail parameter of inlet flow cannot be measured since the they are in the wind tunnel. However, the flow speed is not high and the temperature is high. Thus, Reynolds number is not high. The flow can be considered as laminar flow. The boundary layer in the wind tunnel did not affect the combustor inlet condition. Therefore, the inlet velocity boundary was set as laminar flow without boundary. The outlet was on the rectangular side with a pressure of 0.3MPa. The large eddy simulation has been applied in this simulation.

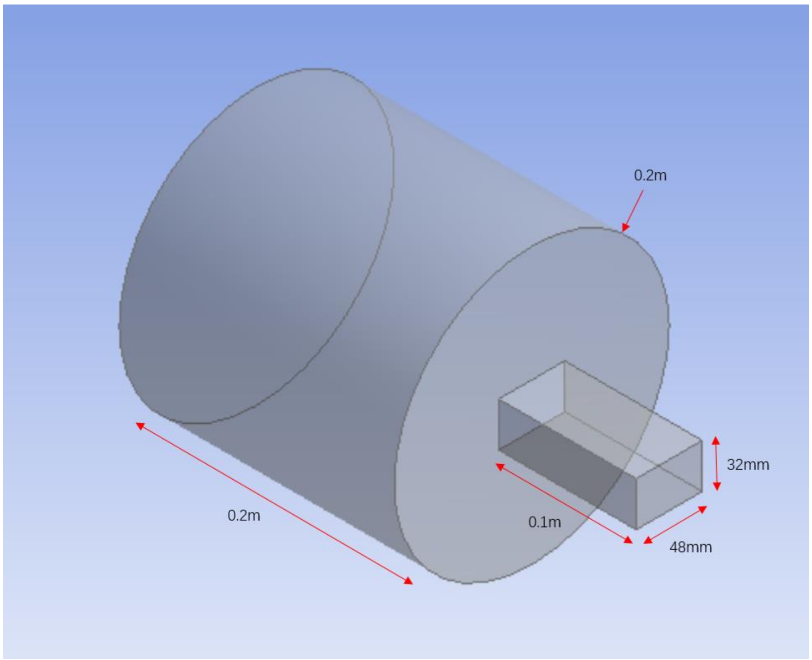

Figure 33 Geometry for inlet condition test

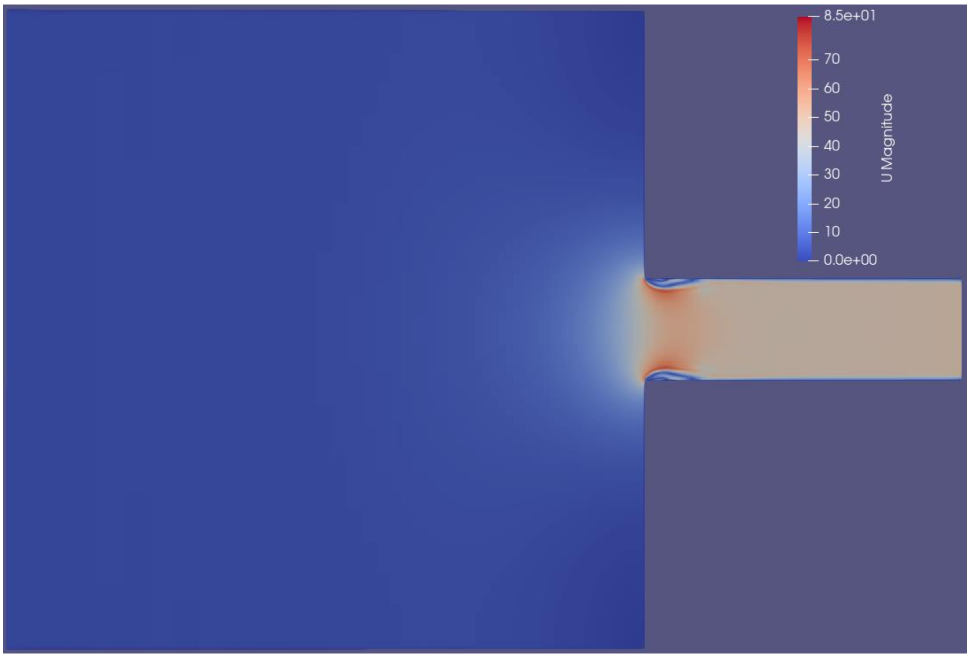

Figure 34 Velocity distribution at the inlet part.

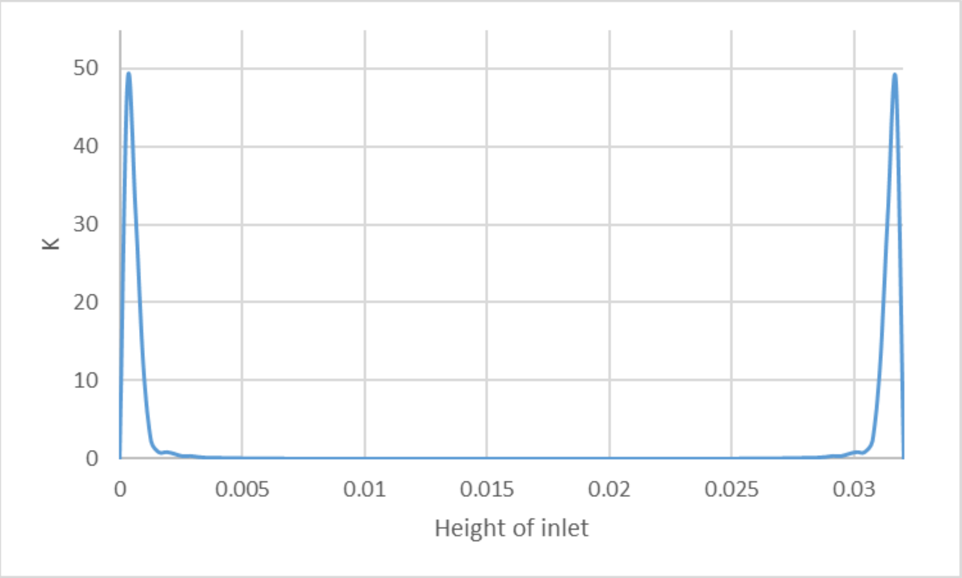

Figure 35 Turbulent kinetic energy along with the height of 30mm from the inlet

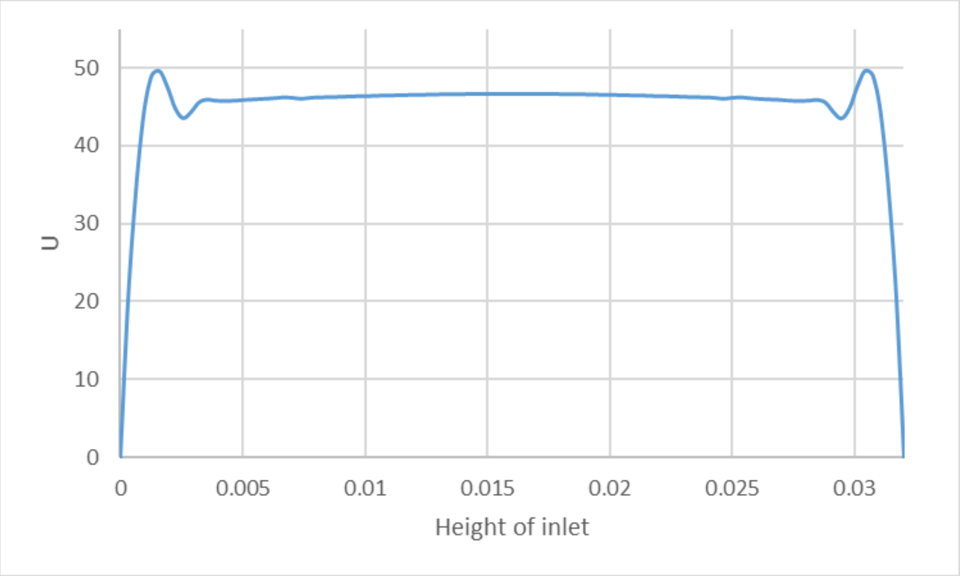

Figure 36 Velocity along with the height of 30mm from the inlet

Figure 34 represents the velocity distribution at the wind tunnel and combustor connection part. The velocity had a sudden acceleration due to the sudden narrowing cross-section area. The airflow shrinking effect was apparent. It made the velocity near the wall accelerate faster than the main flow around the central line.

Figure 34,Figure 35, andFigure 36 indicated that the main flow velocity distribution at the inlet part of the model ramjet combustor is almost uniform. The velocity distribution around wall cannot affect the simulation result of combustion efficiency. Therefore, the setting of uniform laminar velocity boundary condition was suitable for the present research of combustion efficiency.

4.3 Summary

This section has generated the hydrogen flamelet library based on flamelet solutions used for simulating the model ramjet combustor. The sum of the mass fractions of H2O and HO2 was used as progress variable. A priori test has been conducted to validate the accuracy of the hydrogen flamelet library via 1-D counterflow flame. The results indicated that the flamelet library generally agreed with the detailed chemical simulation, although the mass fraction of H was overestimated. The numerical simulation of the wind tunnel and combustor connection part showed that the velocity distribution was much closer to laminar flow at the combustor inlet. Thus, a uniform laminar velocity inlet boundary condition would barely affect the present research of combustion efficiency.

5 Investigation of injection holes’ angle and arrangement

The combustion efficiency is one of the most important parameters for the combustor. However, the research of hydrogen-rich combustion under high enthalpy and turbulence fields is still limited. The investigation conducted under the high turbulent, enthalpy flow field coupled with fast rate chemical reaction by experiment is also quite difficult. Thus, in this section, a numerical simulation domain base on the model ramjet combustor was built up to conduct the research with flamelet/progress variable and large-eddy simulation to investigate the effect of different injection holes' arrangement and injection angle on the combustion efficiency in the model ramjet combustor.

In Chapter2, the research mainly focused on the serial arrangement injector and accumulated a set amount of experiment data. Therefore, the numerical research began with the serial arrangement injector. On the first, the experiment result of serial arrangement injectors was used as the standard to evaluate the accuracy of numerical results. On the other hand, the numerical results revealed the detailed situation of the serial arrangement injector. It is noted that the combustion efficiency of simulation results must be higher than the experiment result since the numerical solver is adiabatic. For the zigzag arrangement injector, the radiation calculated from the temperature distribution of numerical result compared with the NIR image of water emission from the zigzag injector's only experiment result to ensure the simulation result's reliability. Numerical results estimated the effect of injection angle on combustion efficiency. The working situation of the zigzag injector was also investigated.

5.1 Numerical simulation setup

In order to investigate the effect of injection holes' arrangement and angle on combustion efficiency numerically, a computational domain has been made base on the model ramjet combustor of the experiment, as shown in Figure 37.

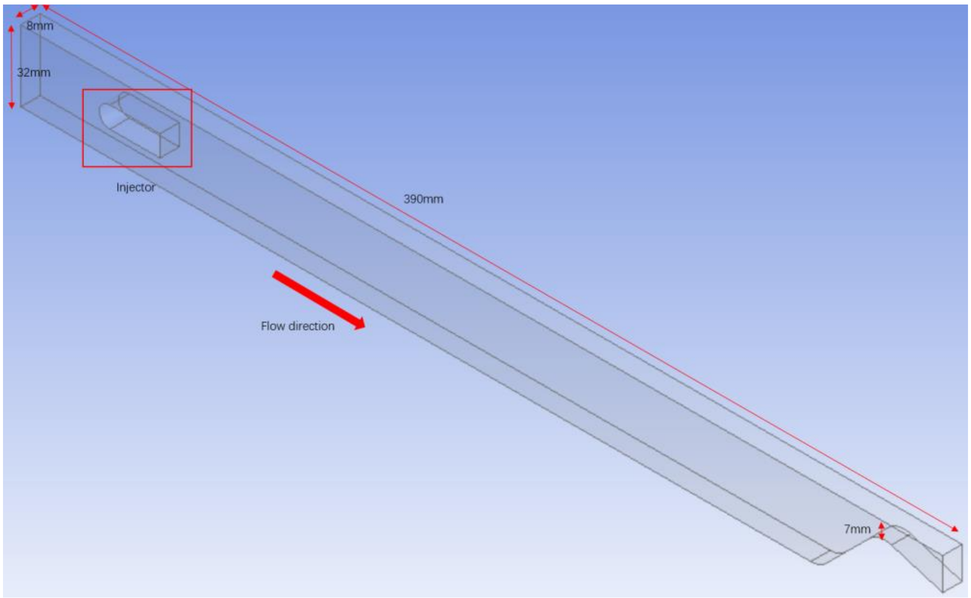

Figure 37 Computational domain

In the experiments, a combustor with a full-sized injector with 24 injection holes was used. In order to reduce the consumption of computational resources and time, the injector simulated was only a "slice" of the actual injector, as shown in Figure 38, with a total of 4 injection holes. The upstream and downstream injection holes are deployed along the central line for the serial arrangement injector. The upstream and downstream injection holes kept them at the same distance with both sides of the computational domain for the zigzag arrangement injector. The width of the fuel inlet was also reduced to 1/6 of the model ramjet combustor of the experiment to adapt the mass flow reducing from the reducing of injection holes' number (4/24) and keep the same equivalence ratio of the combustion in the experiment. With this simplification, the parameter (pressure, velocity) of incoming airflow and hydrogen injection flow were kept the same with the experiment setting. The mixing process of the injection flow was reflected correctly by the numerical simulation. Thus the computational domain had a total length of 390 mm and 8mm x 32mm cross-section area. The nozzle was an 8mm x 7mm cross-section area. The hydrogen injection holes were created as ellipses or circles base on the projection of the different injection angle holes placed on the top and bottom surface of the injector. The injector part had the same side projection as the injector in the experiment. The length was 27.25mm with a round leading edge. The height was 9.5mm, which was also the diameter of the round shape leading edge. The width was the same as the combustor domain.

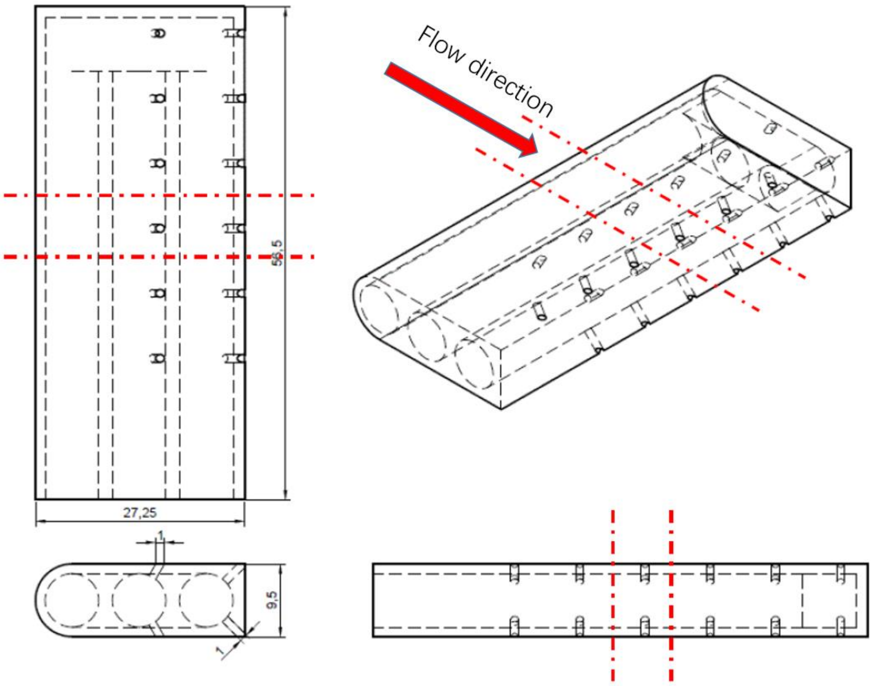

Figure 38 "Slice" of injector [54]

In the domain, there are three eddy generating sources. They are the boundary layer of the wall, the injection flow, and the shear layer generated by the injector's trailing edge, respectively. In the present study, the directly simulated eddy only focused on the eddy in the recirculation zone area since the limitation of computational resource. Hexahedral meshes were used in the domain. O grid mesh was applied around the injector part. Mesh size around the injector was set around 0.2mm. The maximum mesh size of O gride was around 0.3mm. The first layer of the whole combustor was set as y+ around 30. The finer mesh was distributed around the injector and nozzle along the streamwise direction. Mesh size at span direction was set as 0.25mm. The main flow mesh-size at the vertical direction was set as 0.25mm. Figure 39 shows the distribution of mesh of the whole combustor.

Figure 39 Mesh distribution

The air inlet was set as a mass flow rate inlet and assumed as laminar flow. The fuel injection inlet was the same. All inlet boundary was set without boundary layer. The outlet boundary condition was set as pressure far field boundary. The walls in the domain was set as non-slip boundary. Periodic boundary condition was used on the left and right side of the computational domain to simulate the effect of other injection holes during the combustion process. The detailed boundary conditions are shown as following tables.

The other setting of the simulation was as the same as the setting of Sandia Flame D validation.

The parameter of the incoming airflow and hydrogen is in Table 10

Table 10 Parameter of the incoming airflow and hydrogen

	Air	Hydrogen
Temperature	900K	300K
Pressure	0.3Mpa	0.32833MPa
Mass flow rate	0.017kg/s	0.00027kg/s

The boundary condition is shown in Table 11.

Table 11 Boundary type

Air inlet	Mass flow rate inlet
Outlet	Pressure far field
Wall	Adiabatic and none-slip
Left and right side panel	Periodic boundary
Hydrogen inlet	Mass flow rate inlet

The detailed setting of the simulation based on the flamelet progress variable model is shown in Table 12.

Table 12 Parameters on the boundary

	Z	C
Air inlet	0	0
Outlet	Zero gradient	Zero gradient
Wall	Zero gradient	Zero gradient
L and R side panel	Zero gradient	Zero gradient
Hydrogen inlet	1	0

In order to investigate the effect of the injection holes’ arrangement and angle on the combustion efficiency, two kinds of injection holes' arrangement were considered: serial and zigzag, the same as the experiment. For each arrangement, nine combinations of injection holes' angles have been evaluated. The different combinations were listed in Table 13. For convenience, the different combinations have been recorded as upstream injection angle & downstream injection angle; for instance, the combination of upstream injection angle of 30° and downstream injection angle of 60° was written as 30&60. The Upstream part computational domain of cases 30&60 for two kinds of injection hole arrangement is shown in Figure 40 and Figure 41.

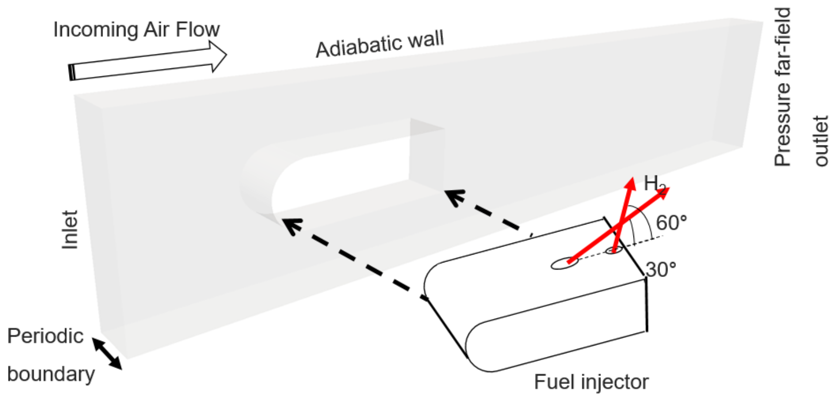

Figure 40 The upstream part of the combustor with serial arrangement injector

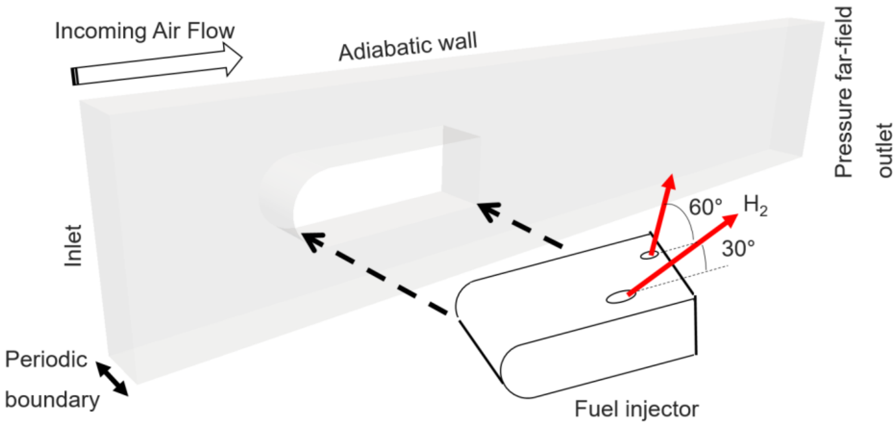

Figure 41 The upstream part of the combustor with zigzag arrangement injector

Table 13 Cases for test

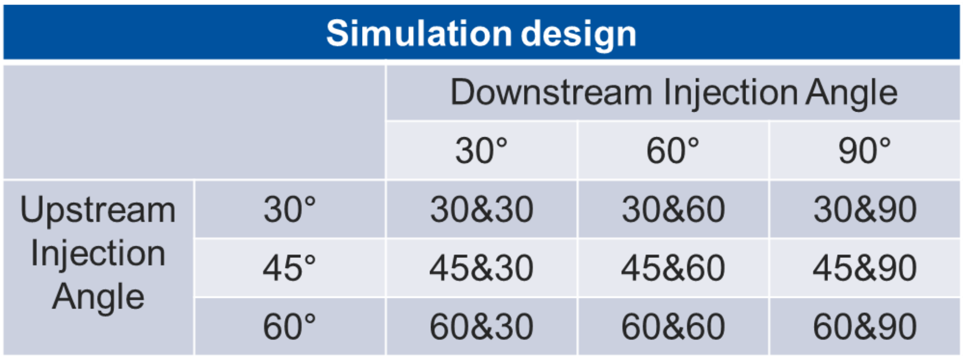

Simulation design				
		Downstream Injection Angle		
		30°	60°	90°
Upstream Injection Angle	30°	30&30	30&60	30&90
	45°	45&30	45&60	45&90
	60°	60&30	60&60	60&90

5.2 Results and discussion

In this section, the effect of injection holes' arrangement and angle has been discussed. The discussion started with a comparison between radiation calculated from the numerical result and NIR emission from water molecules of the zigzag arrangement injector, then focused on combustion efficiency. During the discussion of combustion efficiency, the effect of injection angle on the flame holding area in the recirculation zone behind the injector has been discussed since this area significantly affects the mixing, ignition, and combustion process. The discussion was separated into two main parts by the injector arrangement. The experiment data of the serial arrangement injector can also be used for validating the simulation results. All the figures used in this section were captured after the flame full of the whole chamber.

5.2.1 A test running of zigzag arrangement injector

Figure 42 represents the NIR emission from water molecules of the zigzag arrangement injector. The configuration shows case upstream injection angle 30° and downstream angle 60° of zigzag arrangement under the same condition with the serial arrangement injector experiment. In the image, the flame was anchored in this area for flame holding. It was evident in the image, the emission intensity along the central line was stronger than the emission around the wall. On the one hand, most of hydrogen was injected around the wall. The equivalence ratio was extremely high in this area. It required a long distance for the mixing and ignition process. On the other hand, the heat loss from heat convection with the wall also reduced the reaction rate.

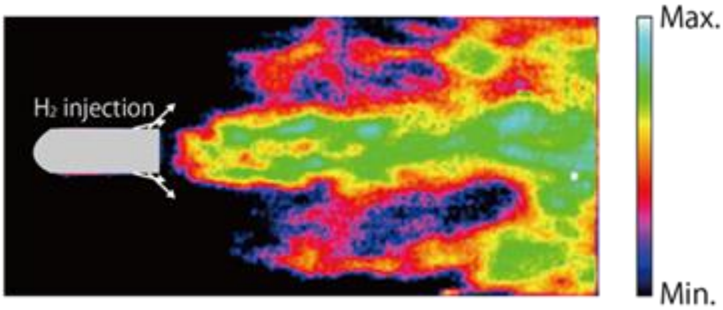

Figure 42 NIR emission from water molecules for case 30&60 of zigzag arrangement

Figure 43 shows the instantaneous temperature distribution on the central plane of simulation. The numerical simulation equivalence ratio kept the same conditions as in the experiments is 2.2, air inlet temperature 900K.

Figure 43 Span averaged temperature distribution of simulation

In order to make a reasonable comparison with NIR image, a modification of simulation temperature result based on the Stefan-Boltzmann law has been considered. The Stefan–Boltzmann law describes the power radiated from a black body in terms of its temperature as

$$j = \sigma T^4 \tag{61}$$

where σ is Stefan–Boltzmann constant and equal to 5.670374e-8Wm^{-2}K^{-4}.

Considering different pressure and temperature also affects the emissivity, The following modification has been applied to the Stefan–Boltzmann law.

$$\varepsilon_g = Z - a_g e^{-kpL} \tag{62}$$

where

$$Z_i = b_1 + b_2 \tau$$

$$a_g = b_3 + b_4 \tau$$

where

ε_g, gas emissivity.

K absorption coefficient of gray gas i,

p partial pressure of the emitting or absorbing gas.

L thickness of the gas slab

$a_{g,}$ the weighting factor of the gray-gas i, i = 0 represents the dear gas for which the absorption coefficient is zero.

b_i constant

T T(K)/1000

The term Z is defined as the sum of the weighting factors of the gray·gases excluding the clear component.

The constant is listed in Table 14.

Table 14 Constant for emissivity calculation

b_1	0.43265
b_2	-0.10890
b_3	0.32730
b_4	-0.043821
k	0.036295

The modified equation is

$$j = \varepsilon_g \sigma T^4 \tag{63}$$

Figure 44 is the image of radiation intensity based on Figure 43. It indicates that the recirculation zone formed by shear layer. However, in the simulation result, the flame holding area in the recirculation zone was attached to the injector's trailing edge since the numerical simulation was conducted under adiabatic conditions. Besides, this figure still showed stronger radiation power than the NIR image, as shown in Figure 42 around the flame front. The reason is Stefan-Boltzmann law includes the radiation intensity from all wavelengths. However, the NIR image only focused on the emissions wavelength over 780nm. Thus the image is different. Overall, the simulation result had a good agreement with the experiment image.

Figure 44 Radiation intensity distribution base on the temperature of the simulation result

5.2.2 Temperature gap

There were several factors that can cause the deviation, including the heat loss. In the experiment, combustion efficiency was calculated using the measured mean value of temperature. Since the maximum temperature for a usually used B-type thermocouple is only 2000K, it is not able to measure the combustion temperature at equivalence ratio phi=2.2, which is over 2500K at adiabatic conditions. Therefore, CO2 was added into the fuel to decrease the combustion temperature. After the fuel was mixed with CO2, combustion temperature became much lower than the pure fuel-air mixture. The amount of the additional CO2 was fixed, thus, the temperature drop caused by CO2 is considered as identical for all different test cases. Moreover, the measured temperature by the thermocouple is lower than the actual temperature due to the heat transfer on the surface of thermocouple. Therefore, calibration of the measured flame temperature from was conducted to compensate the deviation, and the measured temperature in the context was revised with the calibrated temperature. Detailed information about the calibration was performed in thesis section 2.3.

Heat loss in the experiment also influenced the combustion temperature. In order to calculate the order of the influence, the estimation of heat loss from heat convection was conducted. We used an approximation to calculate the

Nusselt number and the heat transfer coefficient. Base on the Eq.(4) and (8) in section 2.3, kinetic viscosity and heat conductivity were calculated. Here, the viscosities and thermal conductivities for each species were calculated using Sutherland’s viscosity law and polynomial approximations on temperature, respectively. Mean velocity is about 50m/s. Characteristic length was 0.0384m. Thus, the Reynolds number Re is about 10768. It is used to estimate the Nusselt number. Base on the equation (14), The Nusselt number is about 52.8. According to equation (11), the heat transfer coefficient is 178.64 W/(m^2K). All cases have the similar result, since the temperatures are very close. Considering the area of walls, the heat loss from the heat convection is about 348J to 351J for different cases with zigzag injector, and 336J to 340J for different cases with serial injector. It is only about 1.6% of the heat release during the combustion process.

In general, the heat loss was very slight and difficult to change the trend of the combustion efficiency. Therefore, the conclusion will not change even if the heat loss was taken into consideration.

5.2.3 Overview of the combustion field

Before investigating the correlation between combustion efficiency and injection angle of two arrangements, a general understanding of the combustion field was necessary. The combustion field can generally be categorized into two statuses by whether the intensive reaction was formed in the recirculation zone for both kinds of injection holes' arrangement since the reaction status in the recirculation zone was always related to the combustion efficiency. All the figures and data used in following sections are based on the time averaged value obtained in one cycle time, defined as the time of airflow going through the combustor.

(1) Serial arrangement injector

Figure 45 shows the time and span direction averaged temperature distribution for the case of 30&60 and 60&90. A weak reaction area was formed in the recirculation zone behind the injector in the case of 30&60. At the same position, an intensive reaction area was formed in the case of 60&90. All the other injectors with serial arrangement had similar temperature distribution with the case of 30&60. Figure 46 indicates the time and span direction averaged temperature standard deviation in the whole combustor. It is clear that the fluctuation almost vanished around the downstream of the combustor. It means that the flow tended to be laminar flow and the mixing process was very weak.

30&60

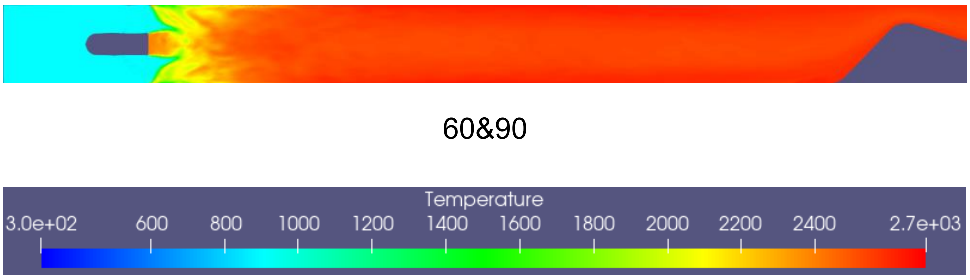

60&90

Figure 45 Time and span direction averaged temperature distribution. The reaction in the recirculation zone behind the injector is clearly different for different injection angle.

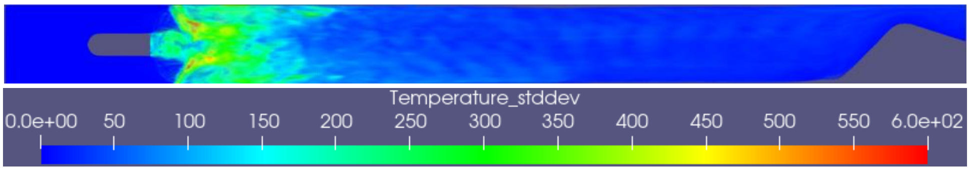

Figure 46 Time and span direction averaged temperature standard deviation for the case of 30&60 with serial injector. The fluctuation is strong around the recirculation zone behind the injector, and almost vanished around the downstream of the combustor.

Figure 47 shows the time and span direction averaged H_2 and O_2 mass fraction for the case of 30&60. Most of the H_2 was injected into the position around the wall. Then, H_2 mixed with and consumed the O_2. O_2 around the central part went through the recirculation zone into the downstream and mixed, reacted with H_2. All serial arrangement injectors had similar distribution.

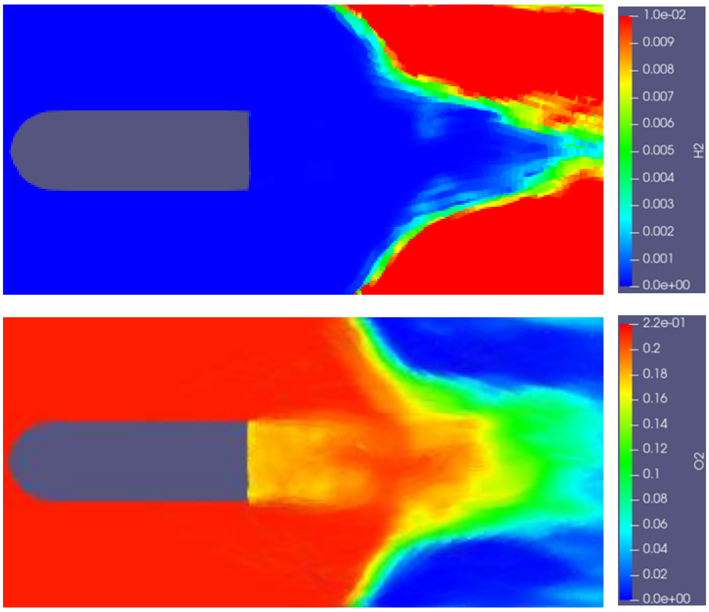

Figure 47 Time and span direction averaged H_2 and O_2 mass fraction for the case of 30&60. Most of H_2 was injected to the wall area and then diffused to the central area of combustor.

(2) Zigzag arrangement injector

The time and span direction averaged temperature distribution for the cases of 30&60, 45&60, and 45&30 are shown in Figure 48. The temperature of the recirculation zone changed from 1400K to 2500K with different injection angles. It indicated that the reaction status was more diverse than the injector with the serial arrangement. Similar flame configuration was also reported by previous researches [55-63]. Figure 49 also shows time and span direction averaged temperature standard deviation in the combustor, and the similar situation with the serial injector, but the high fluctuation area is smaller but stronger than serial injector. It means the mixing efficiency of zigzag injector is much higher than serial injector.

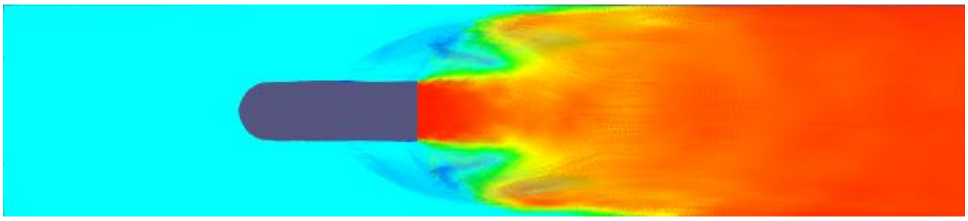

30&60

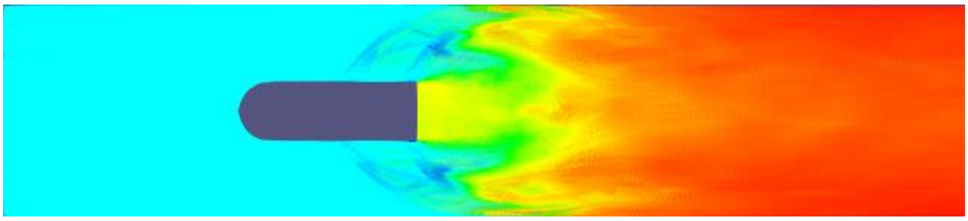

45&60

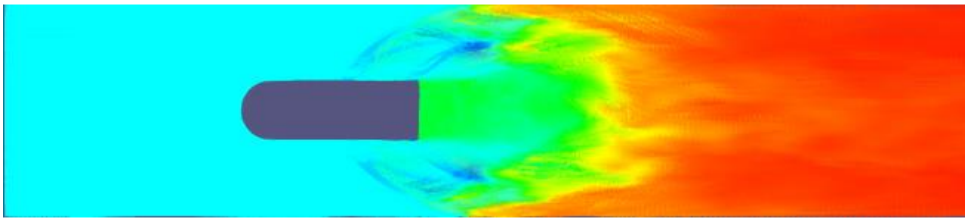

45&30

Figure 48 Time and span direction averaged temperature distribution. The reaction in the recirculation zone behind the injector is different for different injection angle and the reaction status is more diverse than the serial injector.

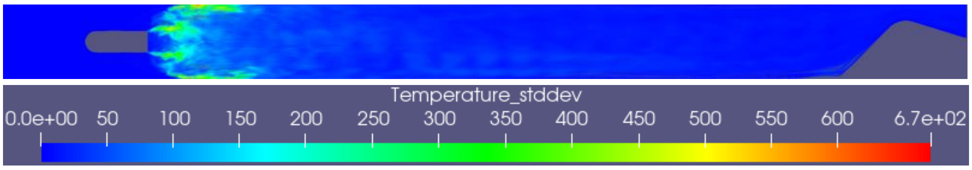

Figure 49 Time and span direction averaged temperature standard deviation for the case of 30&60 with zigzag injector. The fluctuation distribution is similar with the serial injector, but the high fluctuation area is smaller but stronger than serial injector

Figure 50 shows the time and span direction averaged H_2 and O_2 mass fraction for the case of 45&90. H_2 was injected into the combustor separately by upstream and downstream injection holes. The distribution of H_2 was more reasonable than the serial injector. The mixing was also more thorough than the serial injector. The O_2 was almost entirely consumed before they went through the recirculation zone. All zigzag arrangement injectors had similar distribution.

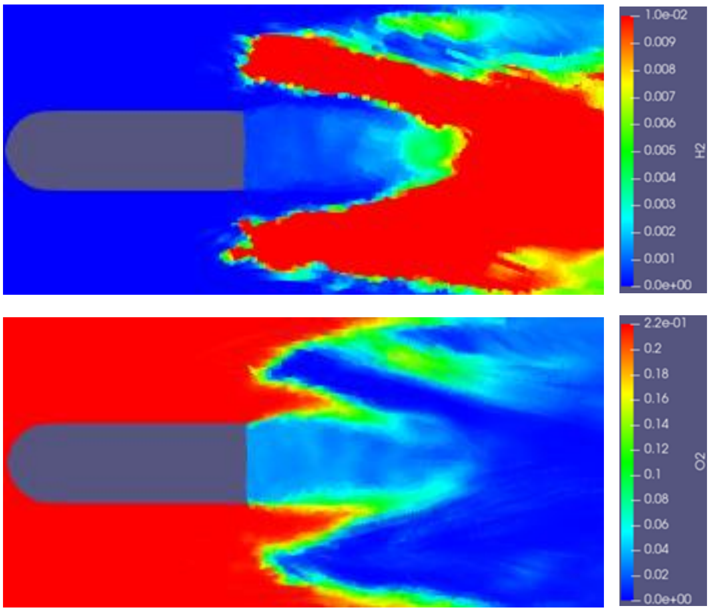

Figure 50 Time and span direction averaged H_2 and O_2 mass fraction for the case of 45&90.

5.2.4 Combustion efficiency

In this section, the combustion efficiency of numerical simulation is calculated from the mean temperature at the cross-section of the same position of the downstream B-type thermocouple.

(1) Serial arrangement injector

Combustion efficiency at the outlet of combustor

Effect of upstream injection angle on combustion efficiency

Figure 51 represents the correlation between combustion efficiency and upstream injection angle for all nine numerical simulation cases. From the plot, it is clear that the injection angle of the upstream had a significant effect on combustion efficiency. The combustion efficiency increased with the upstream injection angle increasing. The trend had a good agreement with the experiment result. Case 60&90 had the best combustion efficiency.

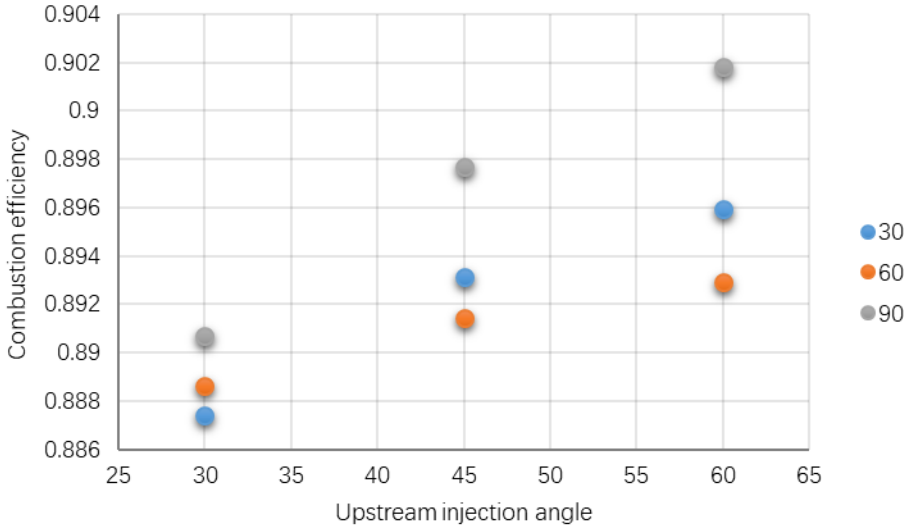

Figure 51 Correlation between combustion efficiency and upstream injection angle (Downstream injection angle marked as legend)

In Chapter 2, the advantage of upstream injection has been discussed. The upstream injection flow had better mixing status since there was no blockage. The combustion efficiency increased with the upstream injection angle increasing since the mixing process around the wall was significantly enhanced. The evidence is that the intensive reaction area around the wall propagated forward with upstream injection angle increasing, as shown in Figure 52.

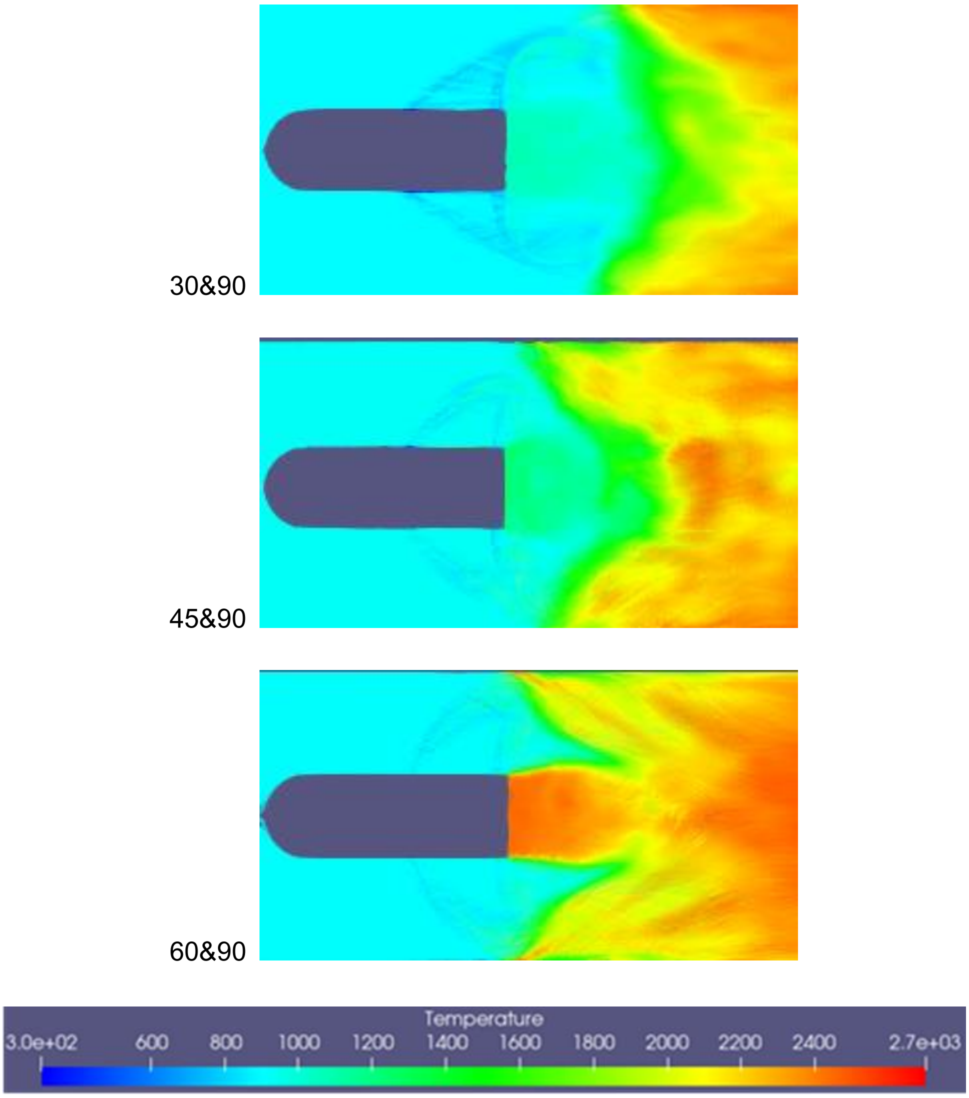

Figure 52 Time and span direction averaged temperature distribution of different upstream injection angles for 90° downstream injection angle. The intensive reaction area around the wall propagated forward with upstream injection angle increasing.

Effect of downstream injection angle on combustion efficiency

Figure 53 indicates the correlation between combustion efficiency and downstream injection angle for all nine numerical simulation cases. It is clear that the injection angle of the downstream row also affected combustion efficiency, but it is not so effective as the upstream injection angle. In addition, the combustion efficiency did not increase monotonously as the upstream injection angle increases when the upstream injection angle is 45° and 60°.

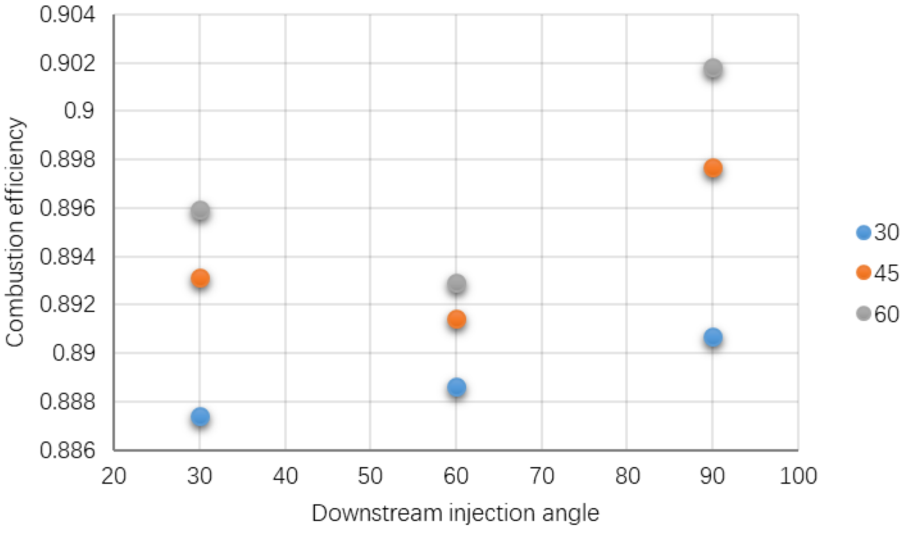

Figure 53 Correlation between combustion efficiency and downstream injection angle (Upstream injection angle marked as legend)

In the cases with a 30° upstream injection angle, the combustion efficiency increased with the increasing downstream injection angle. This result agreed well with the experiment result. Since the 30° upstream injection angle was slight, it had relatively strong interference with the downstream injection flow, as shown in Figure 54. The interference between the upstream and downstream injection flow furtherly enhanced the mixing process.

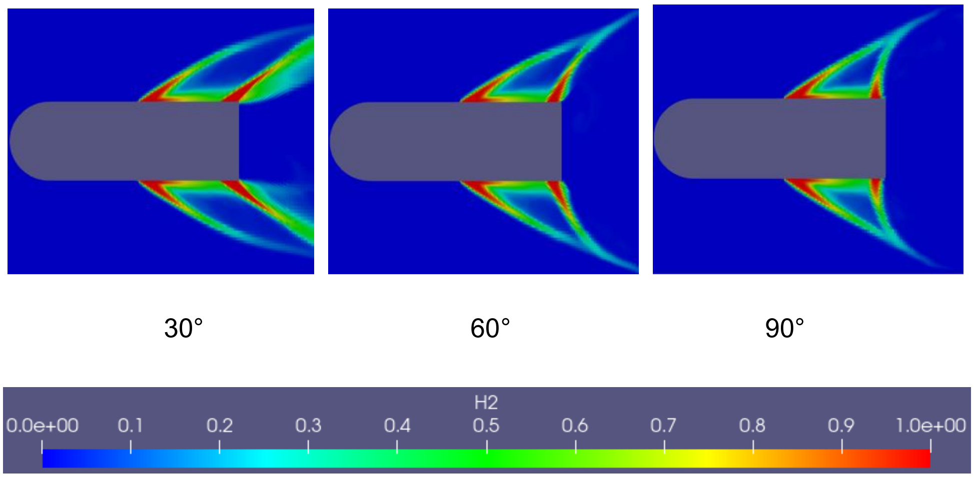

30° 60° 90°

Figure 54 Time averaged H_2 mass fraction distribution with constant 30° upstream injection angle at injection hole cross section (Downstream injection angle marked under the figure)

In Chapter 2, experimental results showed that it was essential to achieve higher combustion efficiency by avoiding upstream and downstream injection flow too close. The two simulation cases with low combustion efficiency were 45&60 and 60&60, as shown in Figure 53. These two cases showed the same conclusion as the experimental result. In Figure 55, the upstream and downstream injection flow was parallel or almost parallel. They injected the hydrogen into the close position.

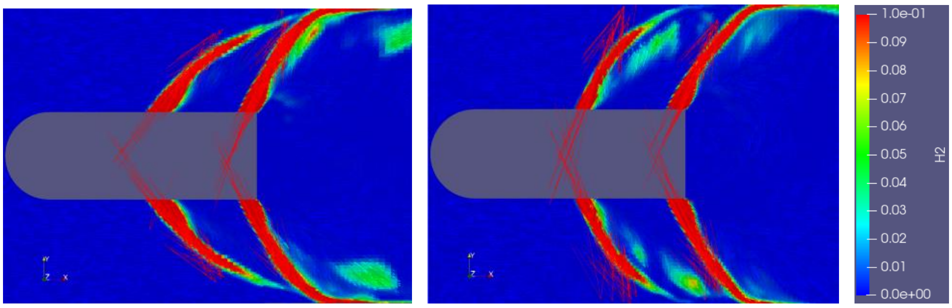

45&60 60&60

Figure 55 Time averaged H_2 mass fraction distribution of case 45&60 and case 60&60 at injection holes cross section

Differences between the effect of upstream and downstream injection angle

The "contradictory" conclusions of interference between the upstream injection flow and downstream injection flow mentioned in the experiment part, a unified conclusion was made in this way; since the upstream injection angle played the most crucial role in combustion efficiency, it had priority to have the best angle for combustion efficiency. If the downstream injection flow was incapable of breaking up the upstream injection flow to enhance the mixing process, the injection angle downstream needed to keep smaller to avoid situations like case 45&60. If the downstream injection flow were strong enough to break up the upstream injection flow to enhance the mixing process, the interference would be helpful to increase the combustion efficiency, as shown in the case of 30&90. In the context of avoiding the interference between upstream injection flow and downstream injection flow, the relatively larger injection angle would be preferred to enhance the mixing process and increase the combustion efficiency, such as case 60&90. Although this kind of interference was very hard to see or analyze quantitatively, it could be considered when very low combustion efficiency happened. The principle of the injection angle setting was to enhance the mixing process and avoid the high local concentration of fuel.

Effect of injection angle to recirculation zone

Effect of upstream injection angle to recirculation zone

As the discussion in combustion efficiency part, the combustion efficiency increased with the upstream injection angle increasing. The O_2 distribution also indicates that the consumption ratio of O_2 was higher with larger upstream injection angle.

The recirculation zone was also extruded at streamwise direction with the upstream injection angle increasing (case of 30&90 and 45&90), as shown in Figure 56. There is a special situation which needs to be noted. The recirculation zone and the injection flow interacted at the downstream area of the recirculation zone, as shown in the case of 60&90. The vortex in the recirculation zone transports part of the hydrogen from injection flow to the recirculation zone to supply the reaction in the recirculation zone, as shown in Figure 57. This interaction improves combustion efficiency significantly. It formed an intensive reaction in the recirculation zone. Thus, the case of 60&90 achieved the best combustion efficiency with serial arrangement injector.

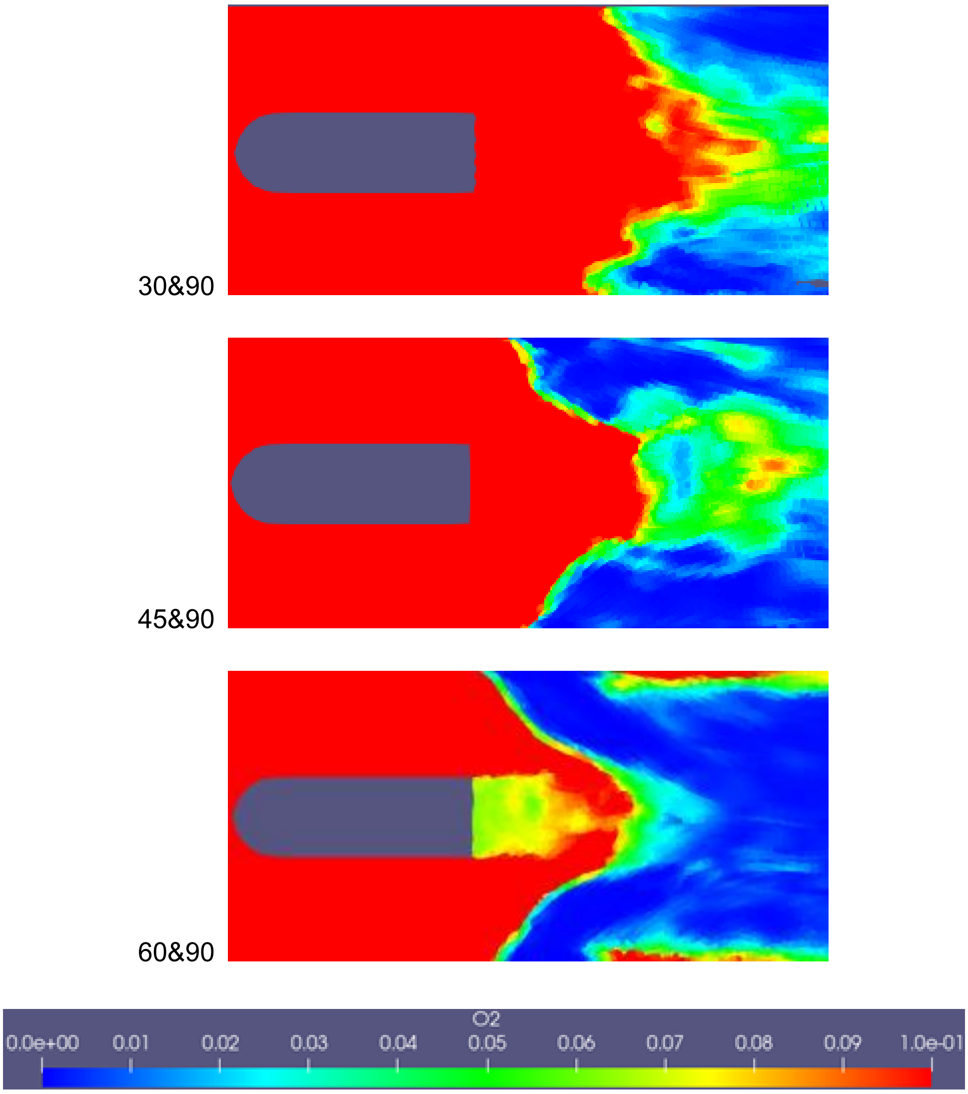

Figure 56 Time and span direction averaged O_2 distribution of different upstream injection angles for 90° downstream injection angle. The O_2 in the recirculation

zone was consumed with upstream injection angle increasing.

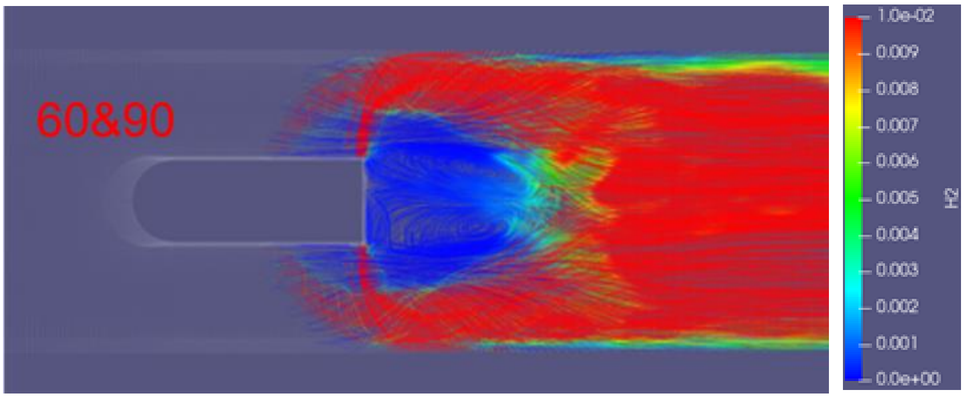

Figure 57 Time averaged streamline colored by H_2 distribution for the case of 60&90. The H_2 was transported into the recirculation zone by vortex.

Effect of downstream injection angle to recirculation zone

The downstream injection angle affected the combustion efficiency by affecting the reaction in the recirculation zone. It is clear that the consumption ratio of O_2 around the central line was increased with a larger downstream injection angle, as shown in Figure 58.

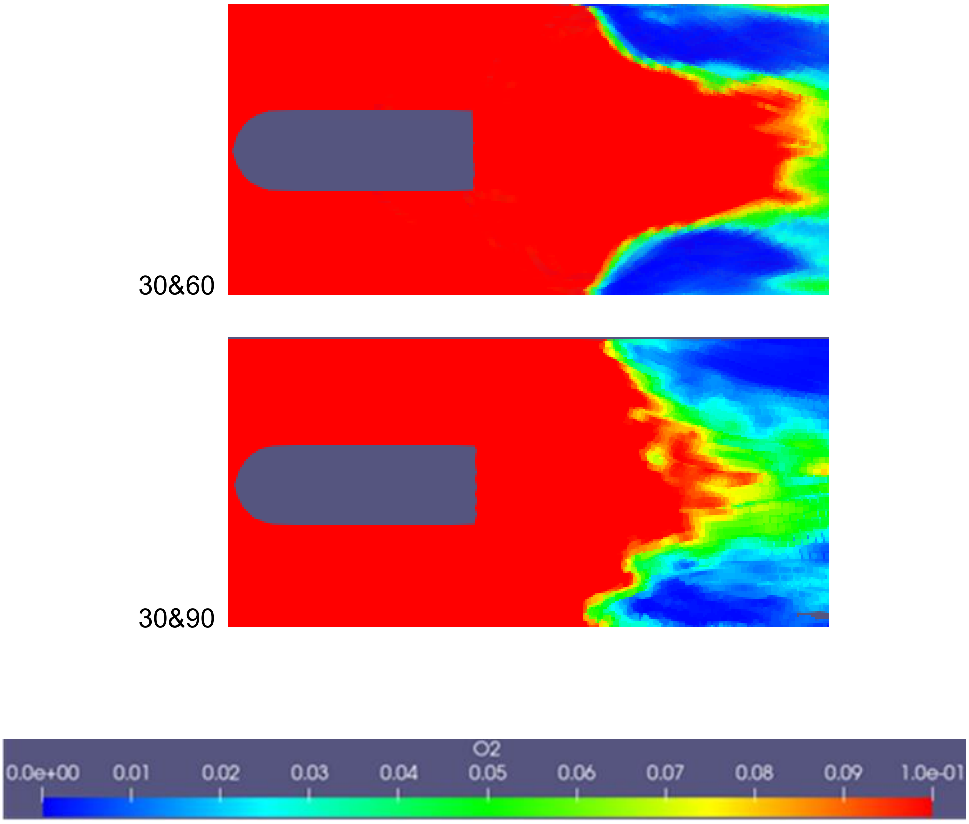

Figure 58 Time and span direction averaged O_2 distribution of different downstream injection angles for 30° upstream injection angle. The O_2 consumption rate was increased with downstream injection angle increasing.

At last, a necessary consideration needed to be mentioned, the larger injection angle could enhance the mixing process and increase the combustion efficiency, but it also injected most of the fuel around the wall. This made the flame close to the wall and brought a large amount of heat loss from heat convection with the wall. The combustion efficiency would be decreased significantly in the simulation with non-adiabatic boundary conditions and experiments.

(2) Zigzag arrangement injector

Combustion efficiency at the outlet of combustor

Figure 59 shows the correlation between combustion efficiency and upstream injection angle of zigzag arrangement injector. This figure indicates that case 30&60 had the best combustion efficiency in all injection angle combinations. In general, the combustion efficiency increased with downstream injection angle increasing and upstream injection angle decreasing, except case of 30&90.

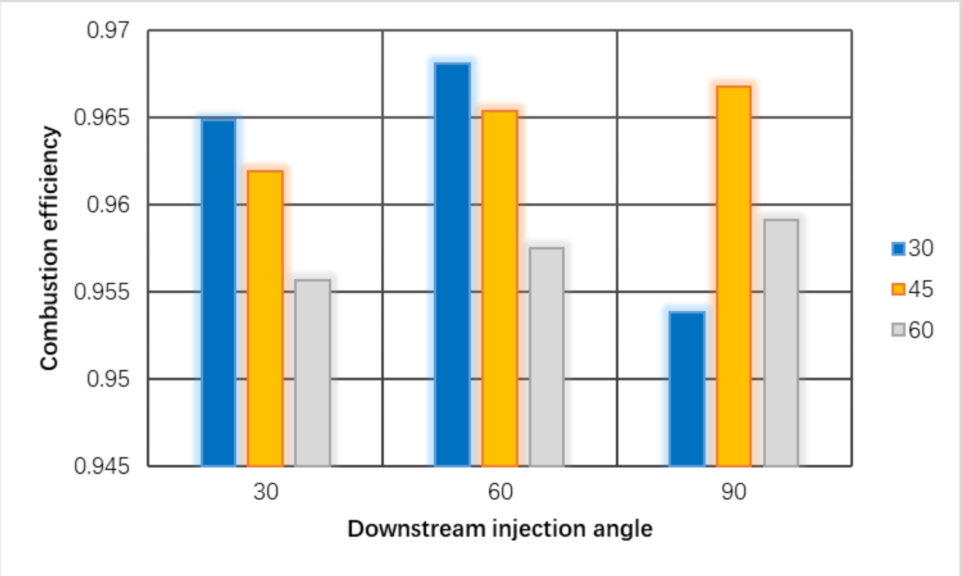

Figure 59 correlation between combustion efficiency and upstream injection angle (Upstream injection angle marked as legend)

Effect of injection angle to recirculation zone

In order to investigate the upstream and downstream injection angle effect on the recirculation zone separately, the combustor was separated into two pieces along the central cross-section of the span direction.

Effect of upstream injection angle to recirculation zone

Figure 60 shows the time averaged streamline colored by hydrogen mass fraction of 90° downstream injection angle in the upstream injection hole piece combustor. With the upstream injection angle increasing, hydrogen flow did not attach to the injector's surface anymore. Thus the supply of hydrogen to the recirculation zone was decreased. The temperature of the recirculation zone was also decreased naturally. The other two downstream injection angles had the same results.

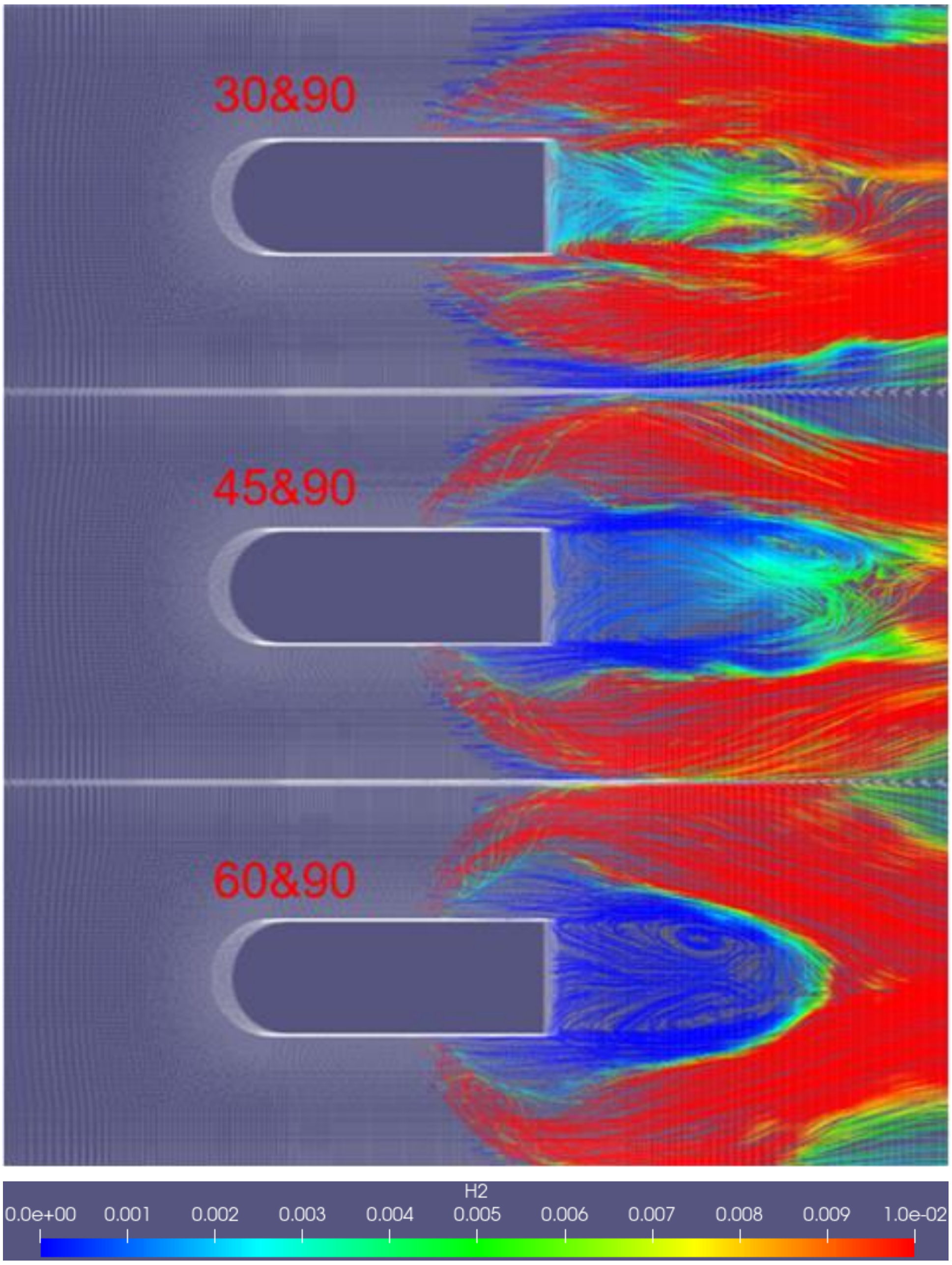

Figure 60 Time averaged streamline colored by H_2 distribution of different upstream injection angles for 90° downstream injection angle (Upstream injection hole piece combustor). The H_2 transported to the recirculation zone by the vortex was decreased with upstream injection angle increasing.

Effect of downstream injection angle to recirculation zone

Figure 61 shows the time averaged streamline colored by hydrogen mass fraction of 45° upstream injection angle in the downstream injection hole piece combustor. The correlation between downstream injection angle and combustion efficiency had a reverse trend to upstream injection angle. The interaction happened between injection flow and vortex at the downstream position of the recirculation zone with downstream injection angle increases. The hydrogen can be transported into the recirculation zone to enhance the reaction.

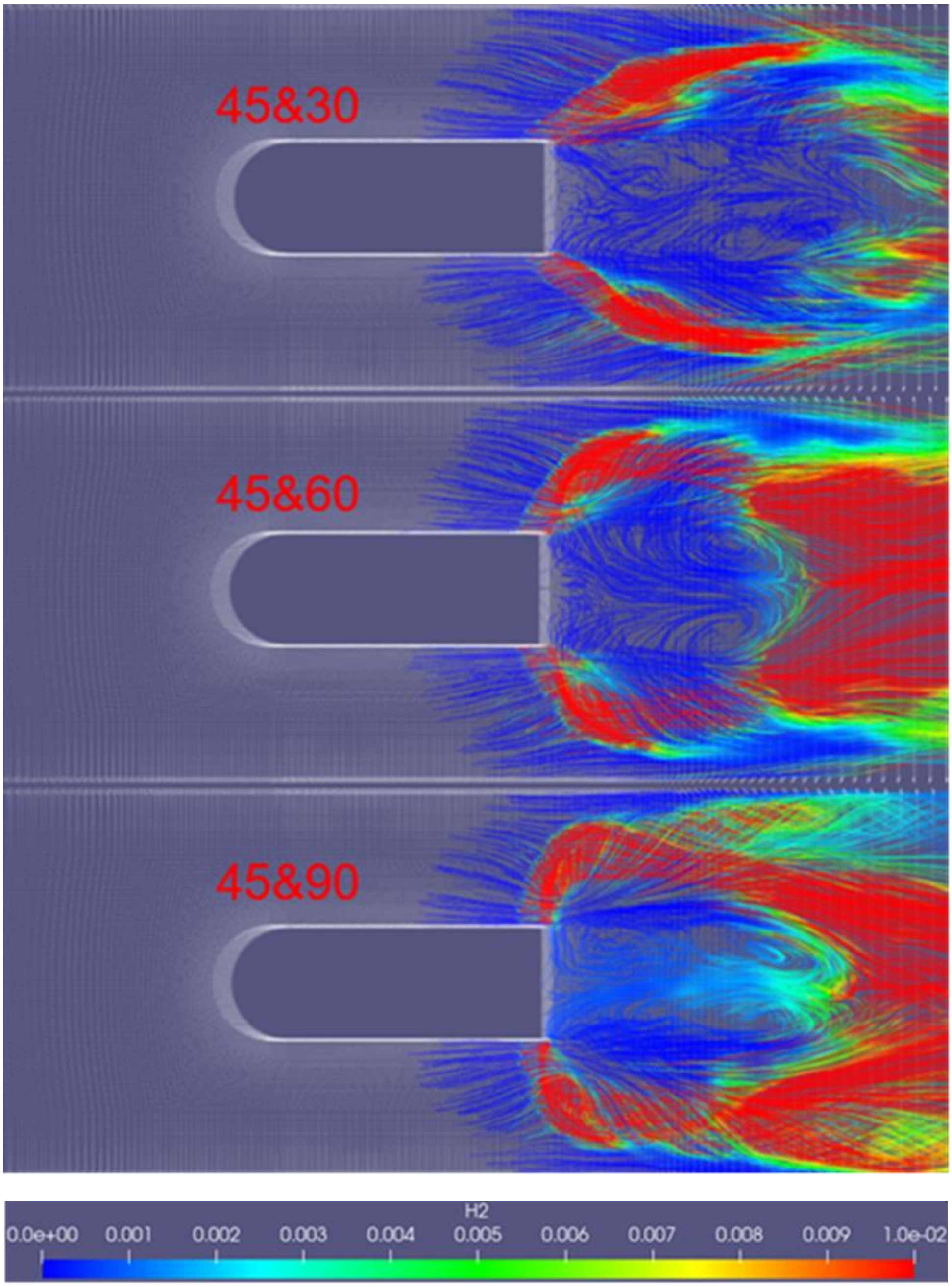

Figure 61 Time averaged streamline colored by H_2 distribution of different downstream injection angles for 45° upstream injection angle (Downstream injection hole piece combustor). The H2 transported to the recirculation zone by the vortex was increased with upstream injection angle increasing.

Thus, the hydrogen supply in the recirculation zone of the zigzag arrangement injector was affected by both upstream and downstream injection angles, and the 30° upstream injection angle can provide a sufficient supply. Thus, a 30° upstream injection angle provided the highest combustion efficiency with a zigzag arrangement injector in the recirculation zone. In theory, case of 30&90 should have the best combustion efficiency, but, in fact, case 30&60 had the best combustion efficiency. The reason was found in Figure 62, a mass of air isolated the flame in the recirculation zone. It stopped the flame in the recirculation zone spread into the injection flow area. Thus the intensive reaction area did not extend but was narrowed compared to case 30&60 as shown in Figure 63.

30&60

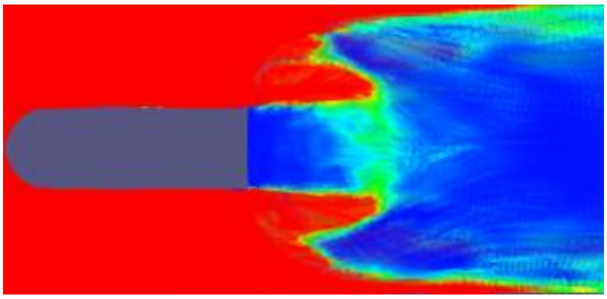

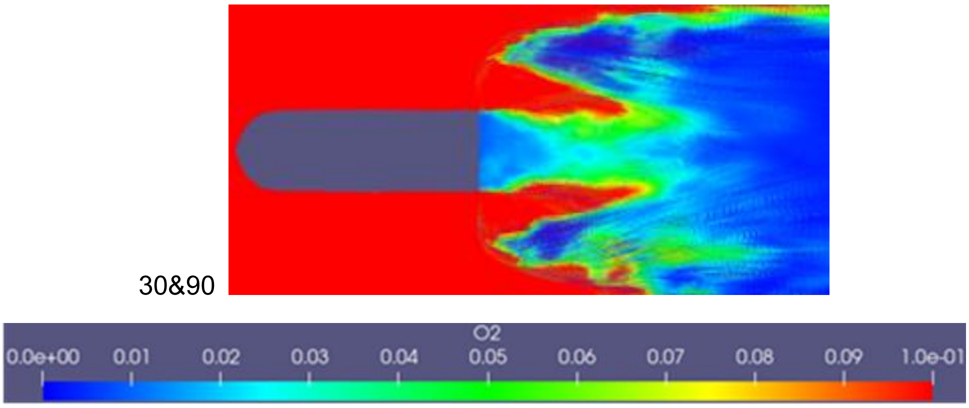

Figure 62 Time and span direction averaged O_2 distribution for cases of 30&60 and 30&90 (Downstream injection hole piece combustor). The O_2 flow isolate the recirculation zone and H_2 injection flow.

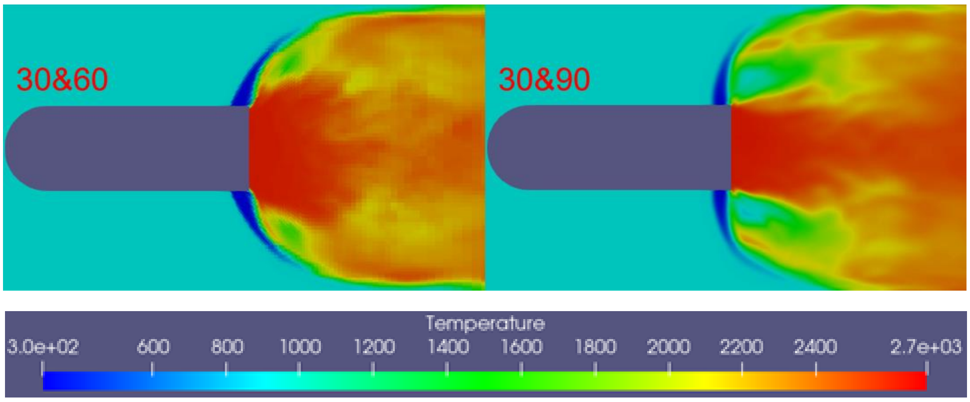

Figure 63 Time averaged Intensive reaction area for cases of 30&60 and 30&90 at downstream injection holes cross section

5.3 Summary

In this section, the effect of injection holes' angle and arrangement have been investigated. The simulation results trend showed a good agreement with the experiment, and case of 30&60 with zigzag arrangement achieved the best combustion efficiency. The zigzag arrangement injector provided a better mixing circumstance for all injection flow since the zigzag arrangement avoided blockage to the downstream injection flow from the upstream injection flow. Naturally, the zigzag arrangement injector had better performance in the mixing process. The O_2 mass fraction distribution clearly indicates that. The combustion efficiency mainly depended on the upstream injection flow for both kinds of injectors. In order to achieve high combustion efficiency, a stable intensive reaction flame holding area is also necessary. The zigzag arrangement injector had the advantage of forming an intensive reaction flame holding area since it can provide sufficient hydrogen to the recirculation zone when the upstream injection angle is 30°.

6 Conclusion

This research investigates the effect of injection angle and injection hole arrangement in a model ramjet combustor by experiment and numerical simulation. A large-eddy simulation coupled with flamelet/progress variable chemical model, validated by Sandia Flame D, was conducted in the present study with OpenFOAM 2.3.x.

The experiment indicated that the combustion efficiency was related to the injection angle and injection holes' arrangement. The larger the upstream injection angle was, the higher the combustion efficiency was for the serial arrangement injector. Interference between the two injection rows had a different effect on the combustion efficiency for different cases. Zigzag arrangement injector increased combustion efficiency dramatically. It had a 10%~15% advantage over the serial arrangement injector.

In order to investigate the turbulent combustion under hydrogen-rich conditions and high enthalpy conditions, a large eddy simulation with flamelet/progress variable chemical reaction model has been performed. It was validated by the Sandia Flame D experiment data and showed good agreement with the experimental results. With the numerical model, the complex situation of the combustion field was investigated by different combinations of injection angle and arrangement. The simulation results showed a good agreement with the experimental result, and the case of 30&60 with zigzag arrangement achieve the best combustion efficiency.

The results indicated that an intensive reaction flame holding area in the recirculation zone is critical for achieving high combustion efficiency. The zigzag arrangement injector has an advantage in supplying sufficient hydrogen to the recirculation zone, although the configuration of the two kinds of injectors is all the same except for the injection holes' arrangement. Thus, the zigzag arrangement injector consistently achieved a better combustion efficiency than the serial arrangement injector. For both injectors, the upstream injection angle played a critical role in combustion efficiency. Besides, in the present research, the fpvFoam is an adiabatic solver. Therefore, the heat loss was not able to be reflected by the solver. As a result, the flame temperature was overestimated, especially for the flame close to the tail of the injector and wall. The effect of the recirculation zone would be much more apparent if the heat loss were counted. The fundamental rules of achieving high combustion efficiency in a robust turbulent flow field are a reasonable fuel distribution and a stable intensive reaction flame holding area.

During the research process, the flamelet/progress variable model showed a good performance. The flamelet/progress variable method provided high calculation efficiency and good accuracy in estimating the chemical reaction. The large-eddy simulation also gave a detailed description of the highly turbulent flow field. Overall, this research was successful and provided a deep understanding of the combustion process in the model hydrogen ram combustor. Having said all of the above, considering the flame anchoring and high combustion efficiency, the zigzag arrangement with 30&60 injection angle is the best design for the injector used in the model hydrogen ram combustor.

Acknowledgments

First, I want to thank my supervisor, Associate Professor Nakaya Shinji. He has taught me experience in all aspects of research. I appreciate all his advice, contribution, effort, and ideas and his valued support throughout my Ph.D. study. Professor Tsue Mitsuhiro has contributed immensely to my professional development during my study at the University of Tokyo. His invaluable advice has brought this work to fruition. I would also like to thank professor Shimada, professor Teramoto, and Associate professor Mogi for providing much-needed comments that led to the completion of this study.

The laboratory members from all of the world have helped me in daily life, adapting to different cultures, whether it was personal affairs or professional advice, they have been a foundation of this thesis. Without their enthusiasm, cheerfulness, and camaraderie, my life and research would have been pale.

As for the experiment of my research, I wish to thank Masafumi Utsumi and Takeo Okunuki for their assistance at the Kashiwa Hypersonic Wind Tunnel experiments.

At last, I would like to thank all the people who helped and encouraged me in the last five years. Your help has made me who I am today.

Che Zhao

The University of Tokyo

July 2021

Reference

[1] Taguchi, H., Harada, K., Kobayashi, H., Kojima, T., Hongoh, M., Masaki, D., ... & Sato, T. (2009). Firing Test of a Hypersonic Turbojet Engine Installed on a Flight Test Vehicle. In 16th AIAA/DLR/DGLR International Space Planes and Hypersonic Systems and Technologies Conference (p. 7311)

[2] Papamoschou, D., & Roshko, A. (1988). Observations of supersonic free shear layers. *Sadhana*, *12*(1), 1-14

[3] Taguchi, H., Kobayashi, H., Kojima, T., Ueno, A., Imamura, S., Hongoh, M., & Harada, K. (2012). Research on hypersonic aircraft using pre-cooled turbojet engines. *Acta Astronautica*, *73*, 164-172.

[4] Taguchi, H., Futamura, H., Yanagi, R., & Maita, M. (2005). Performance analysis of pre-cooled turbojet engines for space planes. *Japan Aerospace Exploration Agency, 2005*.

[5] Sato, T., Taguchi, H., Kobayashi, H., Kojima, T., Okai, K., Fujita, K., ... & Ohta, T. (2007). Development study of precooled-cycle hypersonic turbojet engine for flight demonstration. *Acta Astronautica*, *61*(1-6), 367-375.

[6] Jiang, Y., Gerdroodbary, M. B., Sheikholeslami, M., Babazadeh, H., Shafee, A., Moradi, R., & Li, Z. (2020). Effect of free stream angle on mixing performance of hydrogen multi-jets in supersonic combustion chamber. *International Journal of Hydrogen Energy*, *45*(46), 25426-25437

[7] Li, Z., Manh, T. D., Gerdroodbary, M. B., Nam, N. D., Moradi, R., & Babazadeh, H. (2020). The effect of sinusoidal wall on hydrogen jet mixing rate considering supersonic flow. *Energy*, *193*, 116801

[8] Fox, J. S., Gaston, M. J., Houwing, A. F. P., & Danehy, P. M. (1998, December). Comparison of Hypermixing Injectors Using a Mixture-Fraction-Sensitive Imaging Technique. In *13th Australasian Fluid Mechanics Conference Monash University*.

[9] Bell, P. C. (1971). *Electromechanical Prime Movers: Electric Motors*. Macmillan International Higher Education.

[10] Gerlinger, P., Stoll, P., Kindler, M., Schneider, F., & Aigner, M. (2008). Numerical investigation of mixing and combustion enhancement in supersonic combustors by strut induced streamwise vorticity. *Aerospace Science and Technology*, *12*(2), 159-168.

[11] Schetz, J. A., Maddalena, L., Throckmorton, R., & Neel, R. (2008). Complex wall injector array for high-speed combustors. *Journal of Propulsion and Power*, *24*(4), 673-680.

[12] Michaels, D., & Ghoniem, A. F. (2018). Leading edge dynamics of lean premixed flames stabilized on a bluff body. *Combustion and Flame*, *191*, 39-52

[13] Shanbhogue, S., Shin, D. H., Hemchandra, S., Plaks, D., & Lieuwen, T. (2009). Flame-sheet dynamics of bluff-body stabilized flames during longitudinal acoustic forcing. *Proceedings of the Combustion Institute*, *32*(2), 1787-1794

[14] Zettervall, N., Nordin-Bates, K., Nilsson, E. J. K., & Fureby, C. (2017). Large eddy simulation of a premixed bluff body stabilized flame using global and skeletal reaction mechanisms. *Combustion and Flame*, *179*, 1-22

[15] Giacomazzi, E., Battaglia, V., & Bruno, C. (2004). The coupling of turbulence and chemistry in a premixed bluff-body flame as studied by LES. *Combustion and flame*, *138*(4), 320-335.

[16] Heiser, W. H., & Pratt, D. T. (1994). *Hypersonic airbreathing propulsion*. Aiaa.

[17] Berland, J., Bogey, C., & Bailly, C. (2007). Numerical study of screech generation in a planar supersonic jet. *Physics of fluids*, *19*(7), 075105.

[18] Barber, M. J., Schetz, J. A., & Roe, L. A. (1997). Normal, sonic helium injection through a wedge-shaped orifice into supersonic flow. *Journal of Propulsion and Power*, *13*(2), 257-263.

[19] Tomioka, S., Jacobsen, L. S., & Schetz, J. A. (2003). Sonic injection from diamond-shaped orifices into a supersonic crossflow. *Journal of Propulsion and Power*, *19*(1), 104-114.

[20] Emerson, B., Lundrigan, J., O'Connor, J., Noble, D., & Lieuwen, T. (2011). Dependence of the bluff body wake structure on flame temperature ratio. In

49th AIAA Aerospace Sciences Meeting including the New Horizons Forum and Aerospace Exposition (p. 597).

[21] Safer, K., Tabet, F., Ouadha, A., Safer, M., & Gökalp, I. (2013). Combustion characteristics of hydrogen-rich alternative fuels in counter-flow diffusion flame configuration. *Energy conversion and management*, *74*, 269-278

[22] Moëll, D., Lörstad, D., & Bai, X. S. (2018, June). LES of hydrogen enriched methane/air combustion in the SGT-800 burner at real engine conditions. In *Turbo Expo: Power for Land, Sea, and Air* (Vol. 51067, p. V04BT04A023). American Society of Mechanical Engineers

[23] Sui, C., Zhang, J., Zhang, L., Hu, X., & Zhang, B. (2021). Large eddy simulation of premixed hydrogen-rich gas turbine combustion based on reduced reaction mechanisms. *Engineering Applications of Computational Fluid Mechanics*, *15*(1), 798-814.

[24] Müller, H., Ferraro, F., & Pfitzner, M. (2013, June). Implementation of a Steady Laminar Flamelet Model for non-premixed combustion in LES and RANS simulations. In *8th International OpenFOAM Workshop* (pp. 1-12).

[25] Murthy, R. V. (2008). *Advanced flamelet modelling of turbulent nonpremixed and partialy premixed combustion* (Doctoral dissertation, Loughborough University).

[26] Pierce, C. D. (2001). *Progress-variable approach for large-eddy simulation of turbulent combustion*. stanford university.

[27] Ihme, M., Cha, C. M., & Pitsch, H. (2005). Prediction of local extinction and re-ignition effects in non-premixed turbulent combustion using a flamelet/progress variable approach. *Proceedings of the Combustion Institute*, *30*(1), 793-800.

[28] Pitsch, H., & Ihme, M. (2005). An unsteady/flamelet progress variable method for LES of nonpremixed turbulent combustion. In *43rd AIAA Aerospace Sciences Meeting and Exhibit* (p. 557).

[29] Moin, P., Squires, K., Cabot, W., & Lee, S. (1991). A dynamic subgrid-scale model for compressible turbulence and scalar transport. *Physics of Fluids A: Fluid Dynamics*, *3*(11), 2746-2757.

[30] Pierce, C. D., & Moin, P. (2004). Progress-variable approach for large-eddy simulation of non-premixed turbulent combustion. *Journal of fluid Mechanics*, *504*, 73-97.

[31] Weller, H. G., Tabor, G., Jasak, H., & Fureby, C. (1998). A tensorial approach to computational continuum mechanics using object-oriented techniques. *Computers in physics*, *12*(6), 620-631.

[32] Barlow, R., & Frank, J. (2007). Piloted ch4/air flames c, d, e, and f–release 2.1 15-jun-2007

[33] Taguchi, H., Kobayashi, H., Kojima, T., Ueno, A., Imamura, S., Hongoh, M., & Harada, K. (2012). Research on hypersonic aircraft using pre-cooled turbojet engines. *Acta Astronautica*, *73*, 164-172.

[34] Nishida, S., Ianus, G., Taneda, H., Kita, S., Taguchi, H., Utsumi, M., ... & Tsue, M. (2011). Measurements of Combustion and NOx Emission Characteristics in Afterburner of Pre-Cooled Turbo Jet. In *28th International Symposium on Space Technology and Science*. Okinawa, Japan: The Japan Society for Aeronautical and Space Sciences.

[35] 西田俊介. (2012). *予冷ターボジェットエンジンのアフターバーナにおける水素燃焼に関する研究* (Doctoral dissertation, 東京大学).

[36] Nakaya, S., Funahashi, T., Asakami, Y., Fujio, I., Takahashi, S., & Tsue, M. (2018). Thermometry of combustion gas measuring two-band near-infrared emissions less than 1.1 μm from water molecules. *Experimental Thermal and Fluid Science*, *94*, 1-8.

[37] Morgan, V. T. (1975). The overall convective heat transfer from smooth circular cylinders. In Advances in heat transfer (Vol. 11, pp. 199-264). Elsevier.

[38] Boussinesq, J. V. (1877). Essai sur la théorie des eaux courantes (Essay on the theory of water flow). *Mémoires présentés par divers savants à l'Académie des Sciences, Paris, France*, *23*, 1-680.

[39] Holzmann, T. (2016). Mathematics, numerics, derivations and OpenFOAM®. *Loeben, Germany: Holzmann CFD*

[40] Garnier, E., Adams, N., & Sagaut, P. (2009). *Large eddy simulation for compressible flows*. Springer Science & Business Media.

[41] Smagorinsky, J. (1963). General circulation experiments with the primitive equations: I. The basic experiment. *Monthly weather review*, *91*(3), 99-164.

[42] Deardorff, J. W. (1970). A numerical study of three-dimensional turbulent channel flow at large Reynolds numbers. *Journal of Fluid Mechanics*, *41*(2), 453-480.

[43] Moeng, C. H., & Wyngaard, J. C. (1988). Spectral analysis of large-eddy simulations of the convective boundary layer. *Journal of the Atmospheric Sciences*, *45*(23), 3573-3587.

[44] KOLMOGOROV, A. (1942). Equations of Turbulente Motion of an Incompressible Fluid., Akad, Nak USSR, Ser.

[45]PRANDTL L., Nachr. Akad. Wiss. Göttingen, Math.-Phys., Kl. (1945) 6

[46] C. Fureby, G. Tabor, H. G. Weller, and A. D. Gosman , "A comparative study of subgrid scale models in homogeneous isotropic turbulence", Physics of Fluids 9, 1416-1429 (1997).

[47] Lilly, D. K. (1967). The representation of small-scale turbulence in numerical simulation experiments. *IBM Form*, 195-210.

[48] Garnier, E., Adams, N., & Sagaut, P. (2009). *Large eddy simulation for compressible flows*. Springer Science & Business Media.

[49] Pitsch, H. (1998). FlameMaster: A C++ computer program for 0D combustion and 1D laminar flame calculations. *Cited in*, *81*.

[50] Abstr: Sandia Flame D - KBwiki. https://www.kbwiki.ercoftac.org/w/index.php?title=Description_AC2-09

[51] Bisetti, F., & Chen, J. Y. (2005). LES of Sandia flame D with Eulerian PDF and finite-rate chemistry

[52] Ihme, M., Cha, C. M., & Pitsch, H. (2005). Prediction of local extinction and re-ignition effects in non-premixed turbulent combustion using a flamelet/progress variable approach. *Proceedings of the Combustion Institute*, *30*(1), 793-800.

[53] Kulkarni, R., & Polifke, W. (2012). Large eddy simulation of autoignition in a turbulent hydrogen jet flame using a progress variable approach. *Journal of Combustion*, *2012*

[54] Ianus, G. (2013). *Numerical Simulations on Combustion Characteristics in a Pre-Cooled Turbo Jet Afterburner* (Doctoral dissertation, University of Tokyo (東京大学)).

[55] Erickson, R., Soteriou, M., & Mehta, P. (2006, January). The influence of temperature ratio on the dynamics of bluff body stabilized flames. In *44th AIAA aerospace sciences meeting and exhibit* (p. 753).

[56] Emerson, B., Lundrigan, J., O'Connor, J., Noble, D., & Lieuwen, T. (2011). Dependence of the bluff body wake structure on flame temperature ratio. In *49th AIAA Aerospace Sciences Meeting including the New Horizons Forum and Aerospace Exposition* (p. 597).

[57] Fureby, C. (2000). A computational study of combustion instabilities due to vortex shedding. *Proceedings of the Combustion Institute*, *28*(1), 783-791.

[58] Shanbhogue, S., Shin, D. H., Hemchandra, S., Plaks, D., & Lieuwen, T. (2009). Flame-sheet dynamics of bluff-body stabilized flames during longitudinal acoustic forcing. *Proceedings of the Combustion Institute*, *32*(2), 1787-1794.

[59] Zettervall, N., Nordin-Bates, K., Nilsson, E. J. K., & Fureby, C. (2017). Large eddy simulation of a premixed bluff body stabilized flame using global and skeletal reaction mechanisms. *Combustion and Flame*, *179*, 1-22.

[60] Ghani, A., Poinsot, T., Gicquel, L., & Staffelbach, G. (2015). LES of longitudinal and transverse self-excited combustion instabilities in a bluff-body stabilized turbulent premixed flame. *Combustion and Flame*, *162*(11), 4075-4083.

[61] Ahmed, K. A., & Forliti, D. J. (2010). On the flame and vorticity characteristics of a fluidically stabilized premixed turbulent flame. In *48th AIAA Aerospace Sciences Meeting*.

[62] Giacomazzi, E., Battaglia, V., & Bruno, C. (2004). The coupling of turbulence and chemistry in a premixed bluff-body flame as studied by LES. *Combustion and flame*, *138*(4), 320-335.

[63] Pinchak, M. D., Shaw, V. G., & Gutmark, E. J. (2019). The effects of cross-flow fuel injection on the reacting jet in vitiated cross-flow. *Combustion and Flame*, *199*, 352-364.